DOTTORATO DI RICERCA IN SCIENZE DELLA TERRA

Università degli Studi di Firenze

Giorgio Lacanna

"Modelling the propagation of acoustic waves at the ground – atmosphere interface"

settore scientifico disciplinare: GEO-10

Tutore: Prof. Maurizio Ripepe

Co-Tutore:

Coordinatore: Prof. Federico Sani

XXIII Ciclo

Firenze, 31 Dicembre 2010

Index

List of Figures

List of Tables

Introduction

The main goal of volcano infrasound is to provide information on internal dynamics and to get the state of the volcano activity from the acoustic pressure. Infrasonic sensors and infrasonic arrays installed around the craters have rapidly become a tool widely used in volcano monitoring *(Ripepe and Marchetti, 2002, Garcès et al, 2003, Johnson et al., 2003)*. Infrasound is presently providing new informations directly related to the explosive dynamics and the degassing of the magma process within the conduit. Thus, this signal together with other geophysical parameters (such as: seismic, deformations and thermic) is becoming available and more accurate at several volcanoes around the world. The recordings of infrasonic activity on volcanoes suggests that conduits are opened and that gas can freely expand into the atmosphere. Infrasound produced by the explosive activity are believed to be generated within the conduit at the magma air interface, either (1) by the oscillation of a gas slug at magma free surface before bursting *(Vergnolle and Brandeis ,1996)* or (2) by the bursting of the slug at the magma – free surface *(Ripepe et al.,1996)* or (3) by the pistoning of the magma free level triggered by a deep gas expansion *(Buckingam and Garces, 1996)*. In all such cases the source is well coupled with the atmosphere, and it propagates interacting with the volcanic topography.

Acoustic wave attenuates mainly for geometrical spreading, diffraction at barriers *(Pierce 1974)*, absorption and atmospheric effect (wind direction and velocity, and temperature variations) *(Garces et al. 1998, Ripepe 2007)*.

At short distances from the source (1-2 km) and perfect weather conditions, dry and sunny weather with no wind, the propagation of pressure waves in the atmosphere can be treated as the spherical propagation in a homogeneous elastic medium, intercepting morphological barriers (Fig 1.3) along the path of the sound front. This is a problem common to most volcanoes, specially when the explosive activity occurs in an central crater inside a caldera rim, but it has also more general implications. In particular, the effects of barriers on acoustic propagation has been extensively studied by *Pierce (1974, 1981)* and *Papadopoulos & Don (1991)* to

reduce noises radiating from highway, railway lines, industrial complexes and airports *(Kang 2000, Iu & Li 2002)*.

When the transmission of acoustic wave through the barrier is negligible, the acoustic field in the shadow region behind the barrier is mainly dominated by wave diffracted around the barrier. This effect is proportional to the ratio between wavelength of the signal and dimensions of the barrier *(Hadden & Pierce, 1981)*.

In this thesis we explore the contamination of acoustic wave by volcano topography near the source. We analyze how the pressure field can change interacting with the topography of the volcano, by using experimental measurements carried out at Stromboli in 2009.

We measured infrasound in 5 sites, with source-to-receiver distances ranging from 0.25 to 1.1 km. A reference station was deployed on the summit at a distance of 0.25 km in perfect line of sight with the source.

To investigate the infrasonic wave field produced by two different vents, infrasonic data were collected during 2 different surveys. During a first campaign from July 29, 2009 to August 8, 2009 the SW vent (Fig 3.3 b) was mainly active and during the second one, from September 29, 2009 to October 10, 2009, the NE vent was more explosive (Fig 3.3 d).

Besides, we modelled the effects of topography on the infrasonic wavefield by a Finite–Difference Time Domain (FDTD) method.

In recent years, the finite difference time domain (FTDT) method has gained popularity in simulating wave propagation both for seismic and infrasound *(Madariaga 1976, Liu and Tao1997, Viriuex 1984, Albert et al., 2005; Liu & Albert 2006, Hedlin 2008)*. Here, the bi - dimensional FDTD method is applied to model the experimental measurements. The finite difference method has the advantage of considering a variety of acoustic pulse with complex topography and spatial variations of sound speeds. It can easily provide insights in the complex wave propagation phenomena produced by the interaction of waves with obstacles.

In this work we discuss the experimental measurements and we present a bi - dimensional finite difference time domain (FDTD) method we developed. Finally, experimental measurements and wave propagation modelling are compared.

Volcano Infrasound

The analysis of acoustic pressure produced by volcanic activity after some sparse initial studies *(Machado et al.,1962; Richards, 1963; Woulf f and McGetchin 1976),* underwent a broad expansion in the last 15 *years (Braun and Ripepe, 1993; Vergnolle and Brandeis, 1994; Bucking and Garces, 1996; Ripepe et al., 1996)*.
Volcanoes are an efficient source of infrasound, where degassing from the magmatic system interior may reach its acme in the gigantic explosions witnessed in historic time or inferred from geologic bodies made of tephra deposits. Examples of both occurrences cover a wide range of scientific reports; interesting enough is the Krakatau eruption in 1883, because it was the first documented case when the sound wave was recorded at distances higher than 10 thousand km; in Italy, microbarographs both pathways around the world.
If major explosive events produce impressive phenomena with their pressure waves propagating in the atmosphere. The small size activity offers the best conditions to observe the variety of acoustic signals related to active volcanoes, e.g. from short (few seconds long) single pulses produced by strombolian/vulcanian explosions to sustained acoustic tremor related to persistent degassing *(Ripepe et al.,1996; Hagerty et al. 2000; Johnson, 2003; Johnson et al., 2003)*.
Pressure perturbations are typically recorded at distances of up to a few km from the vent but can be recorded at distances of up to thousands of km, as above mentioned, in case of major Plinian eruptive events *(Morrisey and Chouet, 1997)*, when the injection of large quantity of material generates very long period (>300 sec) acoustic gravity waves.
Acoustic gravity waves were recorded during the 1980 Mt St. Helens and 1991 Pinatubo eruptions *(Mikumo and Bolt, 1985; Thahira et al., 1996),* as well as the 2008 Montserrat Soufrière Hills Volcano *(Ripepe et al., 2009; Ripepe et al., 2010)*, but are not expected to the recorded during small explosive strombolian activity, when mass injection into the atmosphere is relatively small.
The excess pressure produced by volcanoes during strombolian activity *(Vergniolle et al., 1996; Hagerty et al., 2000; Ripepe and Marchetti , 2002; Johnson et al., 2003;*

Ripepe et al.; 2010) is usually small (<10^4 Pa) compared to atmospheric pressure (10^5 Pa), thus allowing us to treat volcanic infrasound as linear elastic waves rather than non – linear shock waves.
Volcanic infrasound appears to be mostly dominated by low frequency (0.5 – 10 Hz) *(Vergniolle and Brandeis, 1994; Garcés ans McNutt, 1997)* resulting in large infrasonic wavelengths, typically in the range 15 – 400 m.
Two main contrasting models for the explosive source process are based on infrasound recorded during degassing and explosive events, while the first explains the observed infrasonic waveform in terms of resonance of a volcanic conduit triggered by a deep pressure perturbation *(Buckingham and Garcés, 1996; Garcés, 1997 Garcés and McNutt, 1997; Garcés, 2000)*, the second identifies the release of over – pressurised gas as the source of infrasound *(Vergniolle and Brandeis, 1994; Ripepe et al., 1994)*.
These two models require completely different source processes to trigger explosive events. The resonance model requires the existence of a pressure drop, deeply embedded in the conduit.
Here, while the propagation of the pressure wave in the conduit radiates energy both into the ground as seismic wave *(Chouet, 1985; Neuberg, 2000)* the reflections at the magma free surface produce infrasound in the atmosphere *(Garcés, 2000)*.
Spectral properties and duration of the recorded signals are explained in terms of resonance of the volcanic conduit *(Buckingam and Garcés, 1996)* and change in the spectral content of the signals are explained in terms of time varying properties (e.g. void fraction) of the magmatic system *(Hagerty et al., 2000)*, which change the propagation efficiency of the resonant pressure wave.
In contrast to the resonance model described above, infrasound may be produced by the sudden release of over – pressurised gas at the magma free – surface *(Vergniolle and Brandeis, 1994; Ripepe 1995; Yamasato 1997; Johnson, 2003)*, where disequilibrium between internal pressure of the gas bubble and magmastatic pressure, in open vent basaltic systems, may be achieved by the collapsing of a foam (CF) *(Vergniolle and Jaupart, 1986)* or by the rise speed dependent (RSD) model *(Wilson, 1980)*.
According to the CF model, Vergniolle and Brandeis (1994) explained the infrasonic transients recorded during explosions from the NE crater of Stromboli in terms of oscillation of a gas slug at the magma free surface before the explosions. On the other hand, discrimination between infrasound produced by explosions from different vents lead Ripepe and Marchetti (2002) to infer an initial gas – bubble burst followed by a time – varying gas release to explain the longer lasting explosions from the SW crater *(Ripepe and Marchetti 2002)*.

In the same way Johnson et al. *(2003)* explained the complex coda of infrasonic waves recorded for explosions at Sakurajima, Arenal, Karymsky and Sangay in terms of sustained degassing triggered by initial pressure onset.
Moreover, in contrast to the resonance model, sustained infrasonic tremors at Stromboli is explained in terms of small gas bursts, repeating regularly in time *(Ripepe et al., 1996; Ripepe and Gordeev, 1999)*, where spectral shift of acoustic tremor is a result of time varying intermittency, rather than of time – varying properties of the magma – gas mixture.

1.1 Explosions and degassing activity at Stromboli

Explosions at Stromboli volcano are an efficient source of infrasound, pressure waves propagating in the atmosphere at a velocity of ~ 340 m/s are commonly produced during the typical explosive activity *(Braun and Ripepe, 1993)*.
Gas reaching the shallow portion of the conduit in non – equilibrium conditions generates pressure perturbations, where amplitude, duration and waveforms of the signals reflect the time history of gas bursting, in terms of source over pressure, mass flux and duration of the explosive emission (Fig1.1). Explosions from the NE crater produce short (<3 sec high amplitude 20 – 80 Pa at 400 meters from the source) pressure wave, while explosions from SW crater are recorded as low amplitude (10 – 30 Pa at 400 meters from the source) long – lasting (5 -15 seconds) infrasonic signals, where a first transient is commonly followed by a complex infrasonic coda *(Ripepe and Marchetti 2002)*. These two clusters can be explained as burst of a large gas pocket while the acoustic coda is controlled by a sustained pressure release

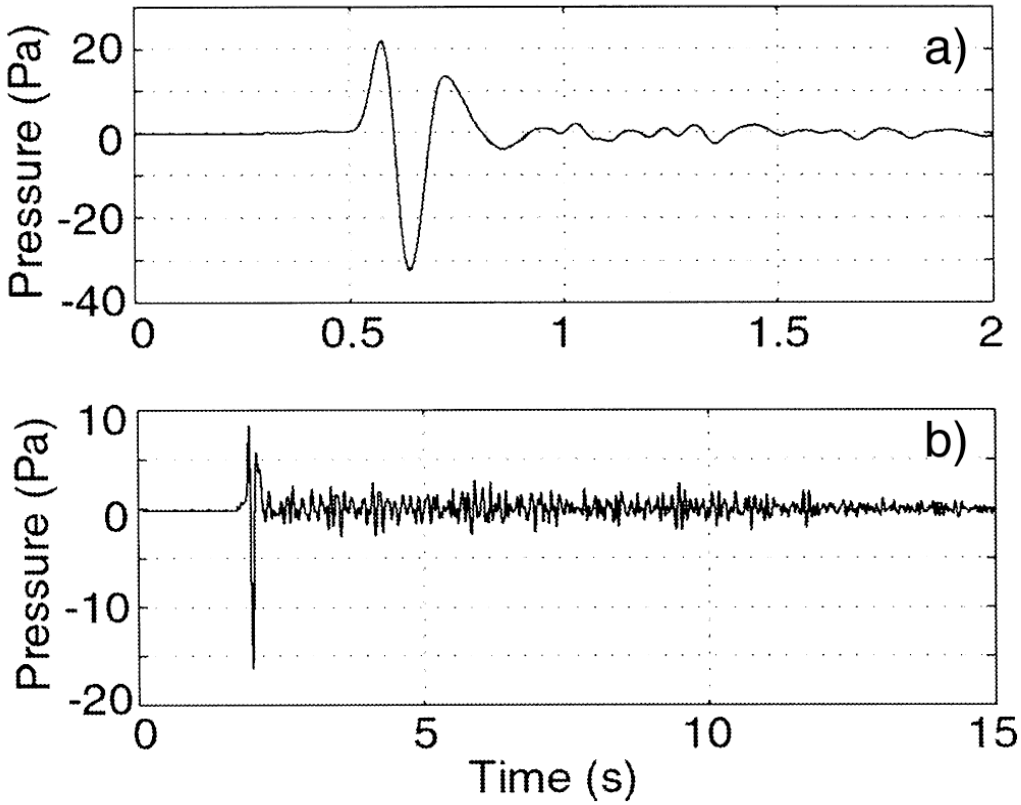

Fig 1.1. Infrasonic waves obtained from the stacking of the infrasonic records related explosions at (a) NE crater and (b) SW crater (from Ripepe and Marchetti 2002)

Degassing of a magmatic system is generally understood as a quasi – steady *(Allard et al., 1994)*, non-explosive passive mechanism, occurring when the slow exsolution process allows the continuous pressure compensation of the gas during its rising through the magma column. However, at Stromboli, infrasound indicates that the degassing occurs also in overpressured conditions, and is associated to the bursting of small gas pockets at the magma – free surface *(Ripepe et al., 2007)*. This intermittent release of gas induces in the atmosphere small (< 1 Pa at a distance of 250 m) infrasonic pulses (*Ripepe and Gordeev, 1999)* and occurs regularly at nearly 1 – 2 second time interval (Fig 1.2b) .

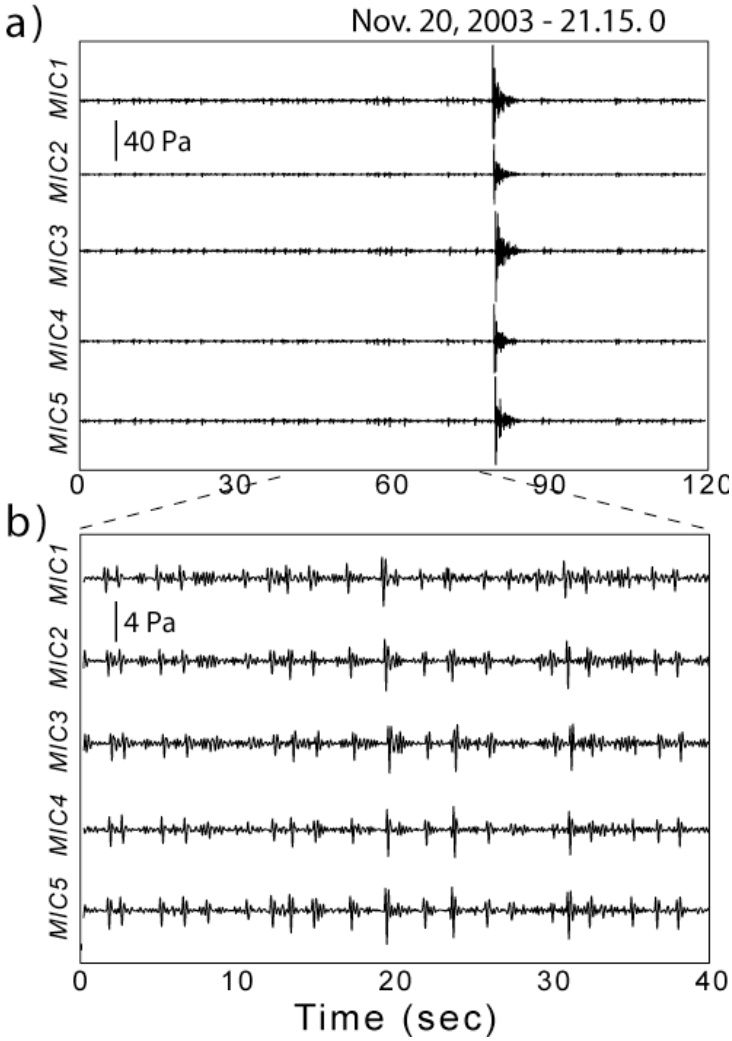

Fig 1.2. (a) Recordings of coherent data reaching the five elements of the array and showing the very low – amplitude intermittent degassing in the back ground, together with one explosive event. (b) Details of small – amplitude infrasonic transients repeating at 2 second time intervals (from Ripepe et al., 2007)

1.2 Significance of the Infrasound signal

Infrasound can provides then a great deal of information regarding gas velocity, gas mass flux and plume height associated to the explosions *(Sparks, 1998; Vergniolle and Caplan – Auerbach, 2006; Caplan – Auerbach et al., 2010)*. Woulff and McGecthin (1976) have suggested to use the acoustic power to estimate gas velocity during volcanic explosions. The total acoustic power Π in watts, emitted in a half sphere of radius equal to the distance *r* between the vents and the pressure sensor, and radiated during a time interval T, given by:

$$\Pi = \frac{\pi r^2}{\rho_{air} c T} \int_0^T \left| p_{ac} - p_{air} \right|^2 dt \qquad 1.1$$

where ρ_{air} is the density of the air, c = 340 m/s is the sound speed and $p_{ac} - p_{air}$ the excess pressure *(Lighthill, 1978)*. Acoustic power can thus be easily estimated from the acoustic record. However the relationship between acoustic power and gas velocity depends strongly on the source model, which can be a monopole, a dipole or a quadripole.

Frequency content of the infrasound waveforms recorded at Stromboli is around 3 to 6 Hz *(Ripepe and Marchetti, 2002; Vergniolle et al., 1996)* with a resulting wavelength in the range of 60 to 120 meters, much larger than the source dimension at the vents, which are usually inferred to be 4 to 10 m in diameter *(Vergnolle and Brandeis, 1994; Genco and Ripepe, 2010)*. This small dimension of the source allows to simplify the mechanism of the explosion to a point source (monopole), and to treat the radiation as isotropic.

For a monopole source, the excess pressure depends on the rate of mass flux *q (Lighthill, 1978)* flowing out the vent that, for a semispherical source of radius *R*, is equal to:

$$q = 2\pi R^2 \rho_{air} U \qquad 1.2$$

where *U* is the radiate expansion velocity. Assuming small monochromatic oscillations ω (ω =2π*f*) at frequency *f*, acoustic power Π radiated in an infinite space is:

$$\Pi = K_m \frac{2\pi R^2 \rho_{air} U^4}{c} \qquad 1.3$$

This indicates that acoustic power depends mainly on gas velocity U, while K_m is an empirical constant *(Vergniolle and Caplan – Auerbach, 2006)*. Mass flux and gas velocity are therefore the crucial parameters to recover, as they are closely related to the bulk gas emission, which is the primary factor characterising the eruptive magnitude. As a consequence, it is of great relevance to calculate mass flux and gas velocity as this provides the estimation of the explosion size and improve the risk assessment.
Volcano acoustic is a useful tool for the management of the risk at Stromboli and, more in general for explosive volcanoes, but the reliability of the parameters depends strongly on the absolute value of the pressure recorded and on the goodness of acoustic waves.
Infrasound monitoring has presently assumed the role of a powerful technique for risk assessment on active volcanoes and then we have carefully analysed how the propagation of sound is controlling both amplitude and waveform of acoustic pressure in near – source (< 1 km) conditions.

1.3 Means and Techniques used

Infrasound may provide the critical constrains to the physics of the source process acting at open vent systems and is a powerful technique for risk assessment on active volcanoes.Small aperture infrasonic arrays can efficiently and precisely locate the infrasonic source position *(Ripepe and Marchetti, 2002; Garcés et al., 2003; Johnson et al., 2004; Ripepe et al., 2010)*. And fast computing time allows real – time monitoring of the position of the explosive source *(Ripepe et al., 2004b)*. Sharp reductions of infrasonic activity at single eruptive vents, which might lead to an increased level of alert, being possibly related to the blocking of the vent can be easily detected . Moreover, the more accurate evaluation of infrasonic amplitudes may be used to better assess the intensity of explosions, to achieve an updated and more complete characterization of the explosive status of active volcanoes
Previous studies on acoustic pressure, were focused on the identify at the source parameters under the assumptions of a waveform not contaminated by scattering, diffraction and reflection of topography neither by the absorption of the atmosphere.
However, the crater rims at Stromboli are bordered by a ridge about 160 meter height. Such as barrier, is less than 200 meter from vents (Fig 1.3) at a distance comparable with the wavelength of 60 -120 meter, > of the recorded infrasound. Thus, scattering, diffraction and reflection effects may be possible, and can modify the wave field in terms of amplitude and frequency content of the sound.

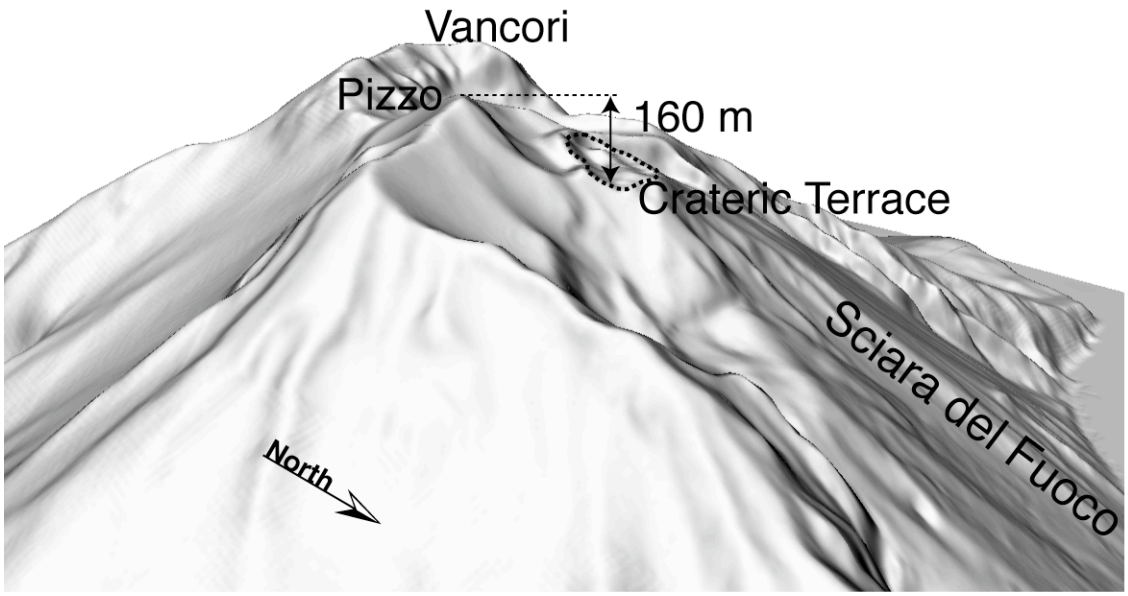

Fig 1.3. Map 3D of Stromboli showing the morphology of the summit of the Volcano. The crater terrace, towards SUD, is bordered by a topographical barrier 160 meter higher. Thus, the wave pressure, with a wavelengths in order of 60-120 meter, propagating intercepts along the path the Pizzo Hill.

Sound Propagation

The atmosphere is a complex medium and the propagation of sound in the atmosphere is a complicated process involving a number of physical phenomena. Sound waves spread geometrically above a ground which may be acoustically “hard” or acoustically “soft”, affecting both the phase and amplitude of sound reflected from the ground. Source and receiver positions determine the attenuation due to atmospheric and the phase difference between the direct and reflected sound at the receiver. Obstacles may be encountered along the propagation path causing shadow zone, diffraction and/or scattering of the sound waves. Wind and temperature gradients cause sound to refract either upward or downward, also leading to shadow zone or multiple reflections, respectively. Additionally, fluctuations of wind and temperature by i.e. atmospheric turbulence, may cause sound to be scattered into acoustical shadow zone.
All the factors mentioned above affect outdoor sound propagation. A more details explanation of these factors and their influence is given in the following sections.

2.1 Geometrical spreading - atmospheric absorption

Sound can be generated by monopole, dipole or quadripole sources. In the numerical models described in this text and the calculations that follow it is assumed for simplicity that all sources are monopole sources.

2.1.1 Geometrical spreading

A monopole source is a point source that generates spherical waves. In a spherical sound wave the sound pressure at any given time is constant within each spherical surface centered at the source, given an ideal atmosphere.
The sound pressure of a harmonic spherical wave can be represented by equation (2.1)

$$p(r) = \frac{1}{r} p_o e^{ikr} \qquad 2.1$$

where $p(r)$ is the sound pressure at the position r, r is the distance from the source and p_o is a pressure at the source. It can be seen that the amplitude of a spherical wave at a distance r is given by $p(r) = p_o / r$, which implies that the amplitude decreases with increasing the distances from the source, see Figure 2.1.

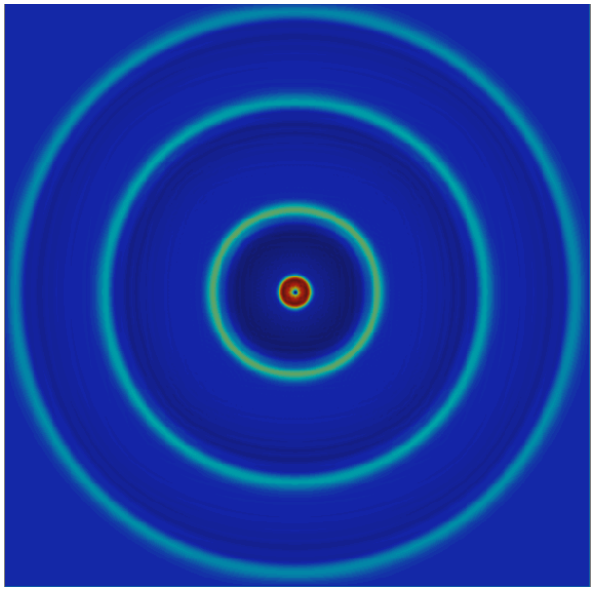

Figure 2.1. Cross-Section of the spherical sound pressure field of a harmonic monopole source. The figure shows how the amplitude of the waves decreases with increased distance from the source located at the center

2.1.2 Atmospheric absorption

In a real atmosphere the decrease in amplitude of the spherical wave is larger than in an ideal atmosphere. This is due to the effect of atmospheric absorption that is the loss of energy in a sound wave from dissipative processes in the atmosphere.
Atmospheric absorption is caused by two effects that attenuate sound propagation in the atmosphere *(Hedlin, 2008)*.

1. Thermal conduction and viscosity of air.

2. Relaxation losses of oxygen and nitrogen molecules in air

The attenuation due to the first effect is twofold. Firstly, temperature gradients in a sound wave are partly reduced by heat flow, depending on thermal conductivity of the air. Secondly, velocity gradients in a sound wave are partly reduced by transfer of momentum transfer, depending on the viscosity of the air. In both cases the energy of the sound wave is converted into heat.

The attenuation due to the second effect takes place on a molecular level. When a sound wave propagates through the atmosphere it causes periodic compressions and expansions of the air. During theses cycles of compression and expansion some energy is converted into heat, and then is the sound wave looses energy.
Absorption mechanism is cumulative, thus, the total attenuation coefficient of sound, in the air is expressed as dB/m, and is given by the linear sum of the attenuation components associated to each individual effect.
Attenuation coefficients computed using the expressions given in *Sutherland and Bass (2004, 2006)* are shown as a function of altitude in Km for frequencies ranging from 0.05 to 4 Hz in Figure 2.2.

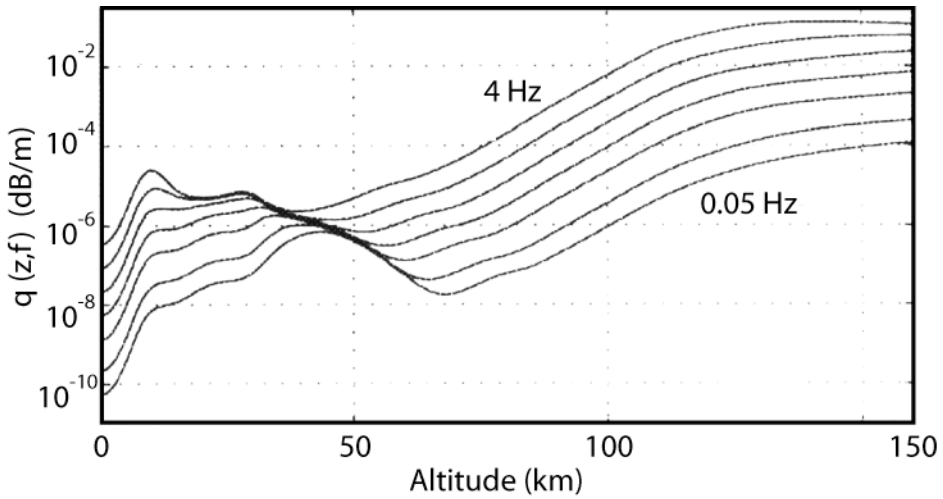

Fig 2.2. Attenuation coefficients for frequencies of 0.05 (lowest curve), 0.1, 0.25, 0.5, 1, 2, and 4 Hz (uppermost curve), compute using the expressions given in Sutherland and Bass (2004).

For infrasonic frequencies, classical absorption dominates at altitudes above 60 Km, and the associated attenuation coefficient, in dB/m, is proportional to the square of the frequency *(Southerland and Bass, 2004)*.
Therefore the absorption coefficient for infrasonic wave recorded at Stromboli Volcano is sufficiently small to be considered negligible, and it is nominally less that 0.001 dB/Km for frequency < 4 Hz *(C. de Groot – Hedlin 2008)*.

2.2 Diffraction at barriers

When sound propagates over a surface waves are reflected from the surface, so they not only direct waves reach the receiver but also reflected waves from topography. Moreover, obstacles along the propagation path, (hills or barriers) will diffracted the sound.

2.2.1 Ground surfaces

Ground can be acoustically characterized by the normalized ground impedance Z which is frequency dependent complex number depending the physical properties of the surface. Ground impedance defined according to equation (2.2), where p and v_n are the complex sound pressure and the normal velocity at the ground surface, respectively,

$$Z = \frac{p}{v_n} \qquad 2.2$$

When a sound wave strikes a porous ground surface, part of the wave is reflected and part is transmitted into the ground (Figure 2.3). The ratio between the reflected and absorbed sound energy depends on the impedance of the material and on the frequency of the sound.
Considering the reflection of a harmonic plane wave on a homogeneous ground surface, with an incident angle normal to the surface. The complex pressure amplitude p in the air above the ground surface will be equal to the sum of the complex pressure amplitude of the incident wave and the complex pressure amplitude of the reflected wave.

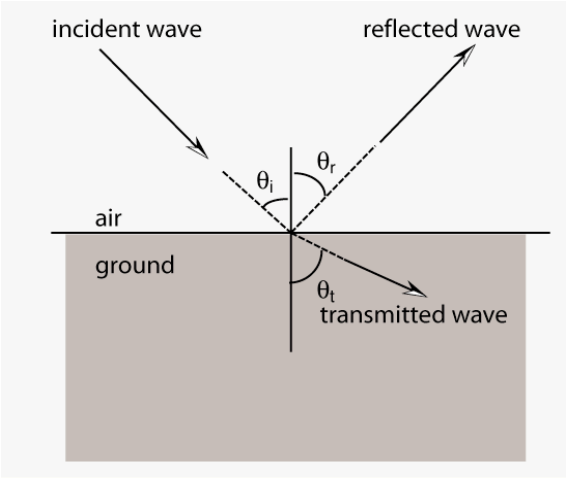

Fig 2.3. Reflection of a sound wave by a ground surface

If the propagation direction is at normal incidence to the ground surface the sound pressure, p, of a plane wave can be described by equation (2.3), where R_p is complex quantity that is called the plane-wave reflection coefficient and p_o is a constant.

$$p(x) = p_o\left(e^{ikx} + R_p e^{-ikx}\right) \qquad 2.3$$

The corresponding complex velocity amplitude v in the air above the ground is defined by equation

$$v(x) = \frac{p_o}{\rho c}(e^{ikx} - R_p e^{-ikx}) \qquad 2.4$$

The ratio $p(x)/v(x)$ is equal to the characteristc impedance ρc of the ground, where ρ and c are density and the sound speed in the ground respectively. Using equations (2.3) and (2.4) with $x=0$ it can be seen that:

$$Z = \frac{1+R_p}{1-R_p} \qquad 2.5$$

which can be written as:

$$R_p = \frac{Z-1}{Z+1} \qquad 2.6$$

Now plane-wave reflection coefficient for normal incidence ($\theta=0$) depends only in the normalized ground impedance. For angle of incidence $\theta\neq0$, the reflection coefficient also depends on θ, and it can be shown that in this case R_p is given by equation

$$R_p = \frac{Z\cos(\theta)-1}{Z\cos(\theta)+1} \qquad 2.7$$

For an acoustically hard surface $R_p = 1$ and for equation 2.5 $Z = \infty$, the sound is reflected with the same phase and amplitude as the incident wave. Examples of acoustically hard surfaces are concrete and water.

2.2.2 Hills and Barriers

Acoustic waves can be diffracted by hills and barriers, or other large obstacles, which can block the sound from reaching areas just behind them, called shadow zones or shadow regions. The effects of hills and barriers are highly influenced by the source and receiver positions and are greatest when the source and receiver are close to the ground, and when the source is not in direct line of sight from the receiver. In these cases the receiver will be in the shadow zone behind the barrier. The effect of a hill on sound propagation from a source near the ground is illustrated in Figure 2.4.

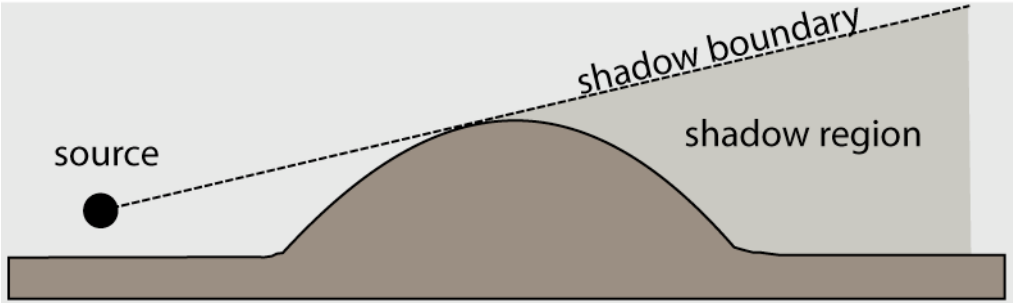

Fig 2.4. Shadow region behind a hill

The efficiency of a barrier to block the sound is highly frequency dependent and, it depends on the relative size of the barrier compared to the acoustic wavelength. This phenomenon is also known as diffraction.
Diffraction involves a change in the direction of propagation of waves as they pass through or around a barrier. The degree of diffraction, that is the amount of sound bent around the obstacle, increase with increasing wavelength and decrease with decreasing wavelength. In fact, when the wavelengths of the wave are largest than the obstacle or opening, diffraction becomes negligible.

2.2.3 Empirical formulae for a thin barrier

The most direct way to investigate the acoustic efficiency of a noise barrier is to perform full-scale field measurements. Alternatively, the acoustic performance of a barrier can be also determined through indoor scale – model experiments.
Nearly 30 years ago, Maekawa *(1968)* measured the attenuation of a thin, rigid barrier, for different source receiver locations. In his experiments a pulsed tone of short duration was used as the source of the noise.
Maekawa described the attenuation of a screen using an empirical approach based on the parameters affecting the screening.

Two important parameters are:

1. The path length from the source to the receiver via the top of the barrier (r_s + r_r) Fig 2.5 and the direct path length from source to receiver R_1, the difference between these length is a measure of the depth of the shadow produced by the screen for the given source and receiver positions.

2. The wavelength of the sound, λ. The longer the wavelength the greater the diffracted wave amplitude is.

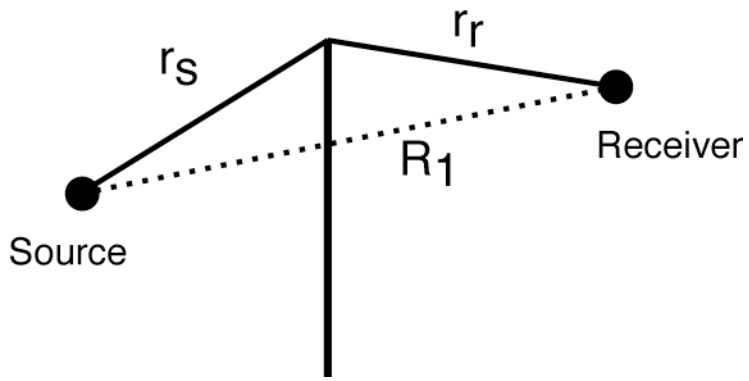

Fig 2.5. Schematic diagram for the diffraction of sound by a semi – infinite plane.

These two parameters were combined into the Fresnel number N in the form:

$$N = \frac{2\left(r_s + r_r - R_1\right)}{\lambda} \qquad 2.8$$

A simple function that fits the Maekawa data quite well is

$$IL = 10\log\left(3 + 20N\right) \qquad 2.9$$

where *IL* is the insertion loss of the screen, that is the attenuation produced by barrier.
The above formula was originally defined only for $N > 0$, but is often used for $N > -0.05$ *(Tatge, 1973)*. More accurate formulae have been proposed by Kurze and Andersson *(1971)*, that has been used widely:

$$IL = 5 + 20\log\left(\frac{\sqrt{2\pi N}}{\tanh\sqrt{2\pi N}}\right) \text{ for } N > 0 \qquad 2.10$$

The Maekawa chart (Fig 2.6) and its associated empirical formulae predict only the amplitude of the attenuation and no wave interference effects will be predicted.

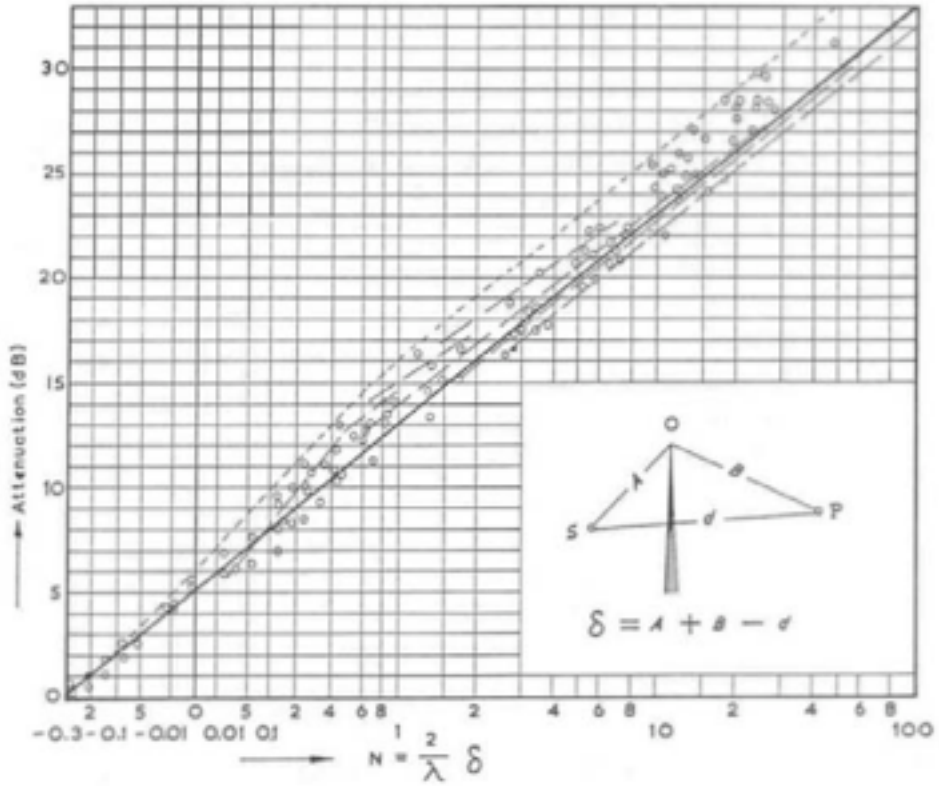

Fig 2.6. Maekawa chart. The insertion loss of the thin screen is plotted against the Fresnel number N

2.3 Meteorological conditions

Meteorological conditions such as temperature and wind variations cause refraction of sound waves and strongly influence the propagation of sound through the atmosphere.

2.3.1 Temperature

The speed of sound in air is a function of the temperature of the air, with increasing temperature the speed of the sound increases. The adiabatic sound speed is given by equation (2.11), where γ is the adiabatic constant of the gas, R is the universal gas constant (8.314 *J/mol K*), P_M is the molecular mass, and T is the temperature (°*K*) of the gas.

$$c = \sqrt{\left(\gamma \frac{R}{P_M}\right)T} \qquad 2.11$$

from which we can obtained an equation widely used:

$$c(T) = \sqrt{\left(\gamma \frac{R}{P_M}\right)T_0 \frac{T}{T_0}} = c(T_0)\sqrt{\frac{T}{T_0}} \qquad 2.12$$

where $c(T_0)$ = 331,6 m/s at T_0 = 273 °K.
From equation (2.12) it can be seen that a temperature variation of 1 °C corresponds rougly to a 0.6 m/s variation in the speed sound for most normal atmospheric temperatures. The presence of a temperature gradient thus produces a spatial variation of sound speed which causes an effect called atmospheric refraction. Atmospheric refraction can be described as the bending (refraction) of a sound wave towards regions where the sound speed is low, this is illustrated in Figures 2.7 and 2.8.

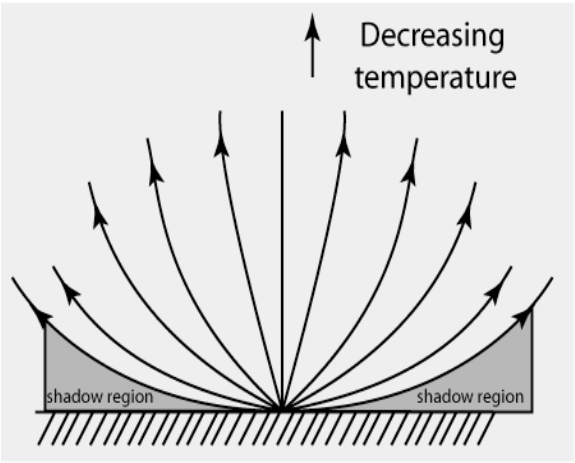

Fig 2.7. Upward refraction and shadow zones caused by a negative temperature gradient.

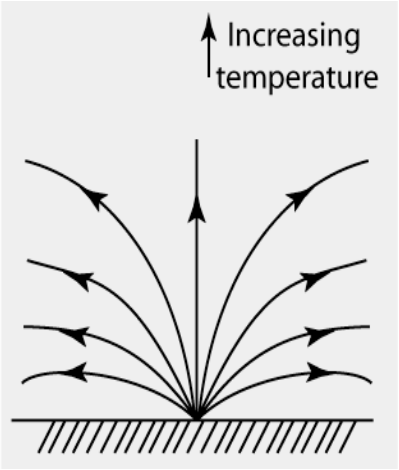

Fig 2.8. Downward and focusing by a positive temperature gradient.

Figure 2.7 depicts refraction caused by a negative gradient in the upward direction. A negative gradient, with the temperature decreasing with altitude, is very common on sunny afternoons. Solar radiation during the day heats the ground which in turn heats the air close to the surface. Since sound moves faster in warmer air, the upper part of wave front will move slower than the lower part. Sound wav will, thus, bends upwards in all direction forming a circular shadow zone.
Figure 2.8 depicts refraction caused by a positive temperature gradient. A positive temperature gradient often occurs at night when the ground cools in the absence of

solar radiation and absorbs heat form surrounding air. These conditions are also common over large lakes or snow covered ground. Under these conditions the situation occurs, that is, sound wave bends downwards in all directions.

2.3.2 Wind

The influence of wind also effects sound propagation. The speed of sound can be approximated as the sound in a non – moving atmosphere plus the wind speed in the direction of propagation, that is sound moves faster in downwind direction than upwind directions. Vertical wind speed gradient commonly exist due to the fact that friction at the ground slows down the moving air, so the wind speed near the ground is always lower. If the sound is propagating against the direction of the wind, upwind, the opposite situation occurs. The sound wave is refracted upward away from the ground forming a shadow zone into which no direct sound propagates. These effect is illustrated at Figure 2.9.

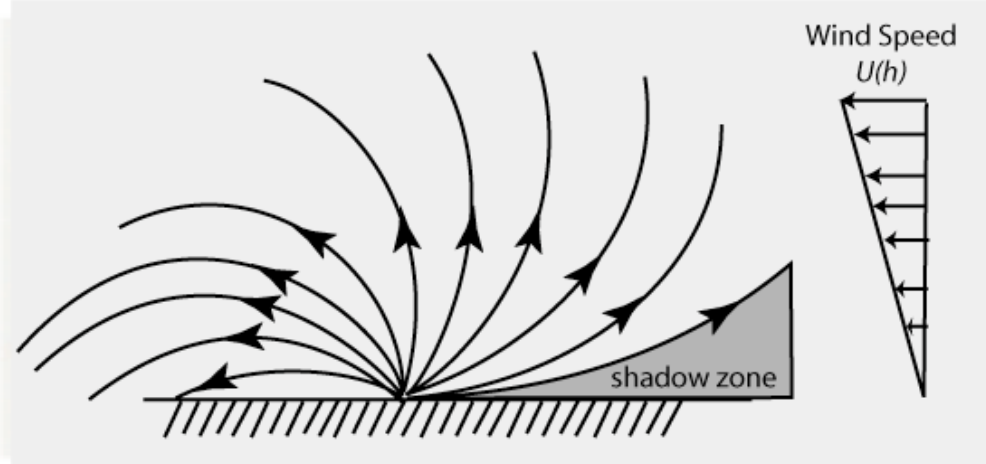

Fig 2.9. Expected refraction effects for an idealized wind speed profile. Upward refraction and shadow zone upwind, downward refraction and focusing downwind.

Measurements

The integrated network of geophysical sensors was deployed by Dipartimento di Scienze della Terra of the University of Florence, at the time of the eruption on Dec 2002. Location of the sensors is visible in Figure 3.1 and consists of 4 seismo - acoustic stations (SAS, STR, ROC, SCI), one 5 – element infrasonic array, one FLIR thermal camera and 3 pinnacle 5000 – series borehole tiltmeters (LFS, OHO, LSC). Each seismo - acoustic station is equipped with a Guralp^{TM} CMG – 40T broadband seismometer, with eigen – period of 30 seconds and sensitivity of 800 V/m/s, and a differential sensor pressure, Honeywell DC001NDC4, with a pressure range of ± 250 Pascal and a sensitivity of 0.01 V/Pa. Moreover, station ROC is equipped with a 15 a degree field of view (FOV) OMEGA^{TM} OS series infrared thermometer, with a sensitivity of 1 mV/°C between -40 and 1100 °C *(Ripepe et al., 2004b*).
Seismic, infrasonic and thermal data are recorded with a 5 – channels, 16 bits A/D converter, at a sampling frequency of 54.2 Hz, and radio transmitted to the recording center (COA) in the village of San Vincenzo, approximately 2 Km away from the summit vents.
Infrasonic analysis of the activity at Stromboli is recoreded by the small aperture array (Fig 3.2), which is placed at a mean elevation of 850 m, and 300 – 450 away from the summit vents (*Ripepe et al.. 2004a,b*). The five elements of the array consist of pre – amplified electric condenser microphones.
The (L) shape geometry and the internal spacing of ~ 100 m. of the array (Fig 3.2) allows the recording of coherent infrasonic waves, in the range of a 1 – 10 Hz frequency band. Their discrimination is particular clear considering a sound speed in the atmosphere of 340 m/s (at 20 °C and 900 m altitude above the sea level) (Fig 3.2). Connection between the five elements of the array is made by a fiber optic cable, which allows the best signal – to – noise ratio and reduces the risk of lightning damage. Infrasound detected by the 5 element is converted to a digital record by a single 5 – channel A/D converter with a sampling frequency of 54.2 Hz (*Ripepe et al. 2006*).

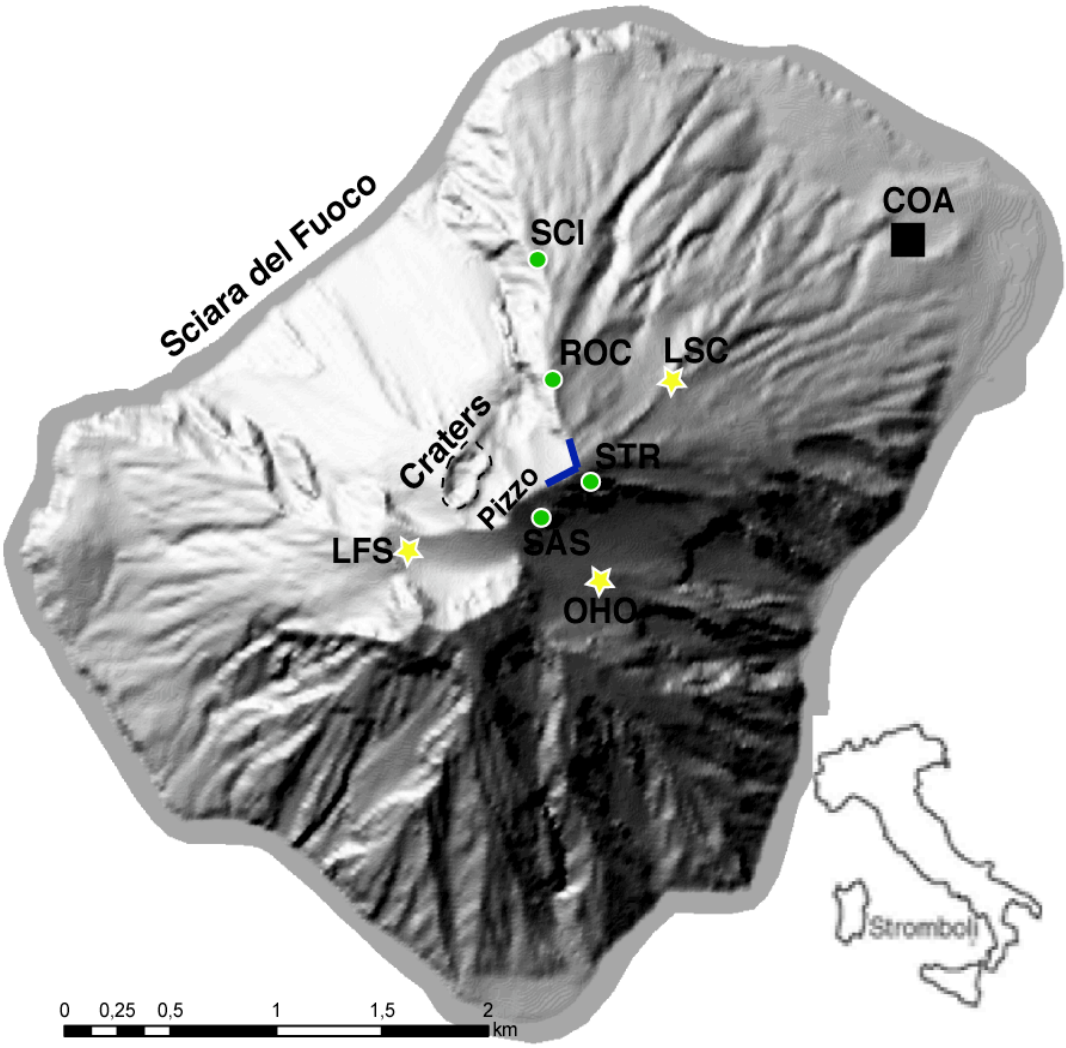

Fig 3.1. Map of Stromboli Volcano showing the position of the seismo – acoustic stations (green – circles), infrasonic array (blue line mettere in rosso), borehole tiltimeters (yellow stars) and recording center (black square) deployed by the Dipartimento di Scienze della Terra, of the Università di Firenze.

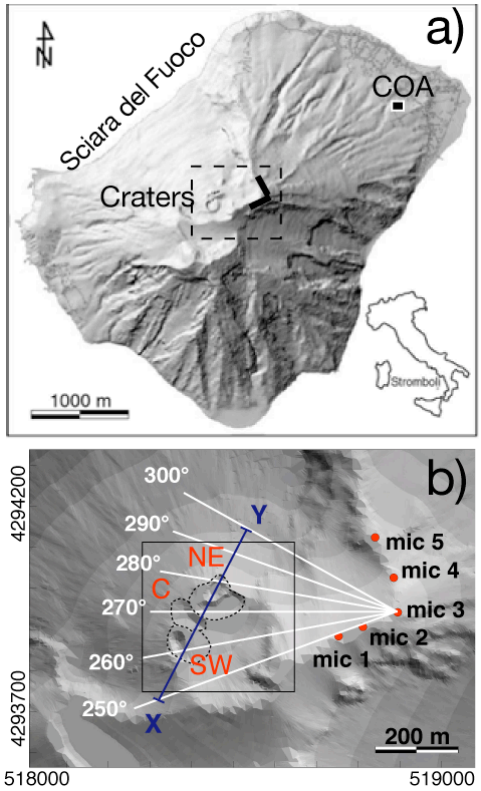

Fig 3.2. Map of the summit of crater (in the upper figure) and a zooming (in the lower figure) showing the position of the array with respect to the vents; and the position of the searching area used in real – time location of the infrasonic source. The grid (square) extends over an area of 400 x 400 m with an internal spacing of 10 m centred on the crater terrace. The position and dimension of the grid allow us to investigate all of the possible infrasonic sources on the crater terrace, and the spacing (10 m) allows a good discrimination between different vents.

3.1 Analysis of Infrasonic Array

One of the main goal for a correct evaluation of the risk, depends on the efficiency to monitor the evolution in time and space of explosive activity at each different vent. This can be achieved using the coherence properties of the infrasonic signals across the array.

The algorithm, for the automatic detection of coherent infrasonic signals, is based on a grid searching procedure *(Ripepe et al., 2007),* operating with a minimum computing time on a single computer and with the highest resolution and, the best coverage of the crater terrace.

On a grid searching procedure, infrasonic source is searched over an area of 400 x 400 m, with a 10 m spacing and centred on the crater terrace at a fixed elevation (z_0) of 750 m a.s.l (Fig 3.2b). For each node (x,y,z_o) the theoretical infrasonic travel times

$\nabla t(x_i,y_i,z_o)$ are calculated at each microphone *(i)* of the array, assuming a spherical wave propagation and a mean sound speed *(c)* of 340 m/s in the atmosphere at 20°*C* and 900 m:

$$\Delta t(x_i,y_i,z_o) = \left[\left(x - x_i\right)^2 + \left(y - y_i\right)^2 + \left(z_o - z_i\right)^2\right]^{1/2} c^{-1} \qquad 3.1$$

where (x_i,y_i,z_i) are the coordinates of the *i-th* element of the array.
According, to equation 3.1, infrasonic signals recorded by the array are delayed by the corresponding theoretical travel time $\nabla t(x_i,y_i,z_o)$ and then the semblance $s_{ij}(x_i,y_i,z_o)$ between infrasound recorded at different couples of station is calculated:

$$s_{ij} = \frac{COV\left[P_i\left(t - \Delta t\left(x_i,y_i,z_o\right)\right),P_j\left(t - \Delta t\left(x_j,yj,z_o\right)\right)\right]}{\sigma\left[P_i\left(t - \Delta t\left(x_i,y_i,z_o\right)\right)\right] \times \sigma\left[P_j\left(t - \Delta t\left(x_j,y_j,z_o\right)\right)\right]} \qquad 3.2$$

where *COV* is the covariance and σ is the standard deviation of the infrasonic records *(P(t))* at stations *i* and *j* of the array, Equation 3.2 is applied to all of the possible permutations among signals recorded at the 5 elements of the array, providing for each node (x,y,z_o) of the searching grid a mean semblance $S(x,y,z_o)$.

$$S(x,y,z_o) = \frac{\sum_{i=1}^{N}\sum_{j=i+1}^{N-1} s_{ij}\left(x,y,z_o\right)}{\sum_{i=1}^{N-1} i} \qquad 3.3$$

where *N* represents the number of array elements *(N = 5)*. Values of $S > 0.6$ are assumed to be indicative of well – correlated signals. The source will be then located in the nodes, which according to the distribution of the mean semblance $S(x,y,z_o)$ have value higher than 0.6 (Fig 3.3a,c).

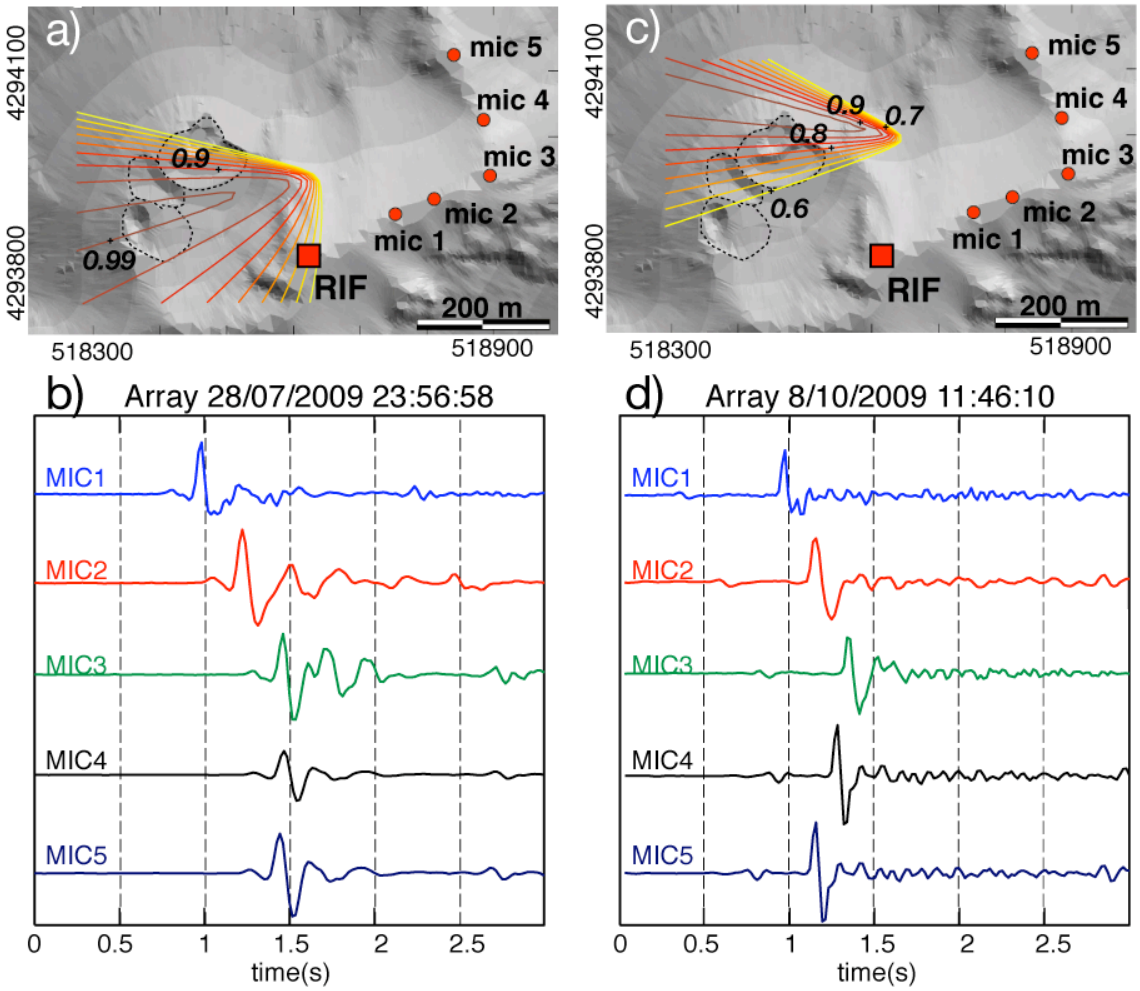

Fig 3.3. Position of the reference station (RIF) located on summit of the Pizzo hill. Examples of source location (a) by array acoustic signals (b) associated with an explosion at the SW crater, recorded during first acquisition campaign between July 29, 2009 and August 8, 2009. (c, d) an explosion at the SW crater recorded during second acquisition campaign September 29, 2009 and October 10, 2009 . Contour lines represent the mean semblance distribution on the grid, discuss in previous section, and indicate the most probable direction of the infrasonic wavefront.

3.2 Data Acquisition

During two surveys of nearly ten days, long each we recorded daily hundreds of explosions in summer of 2009, produced by both explosive vents. The first campaign was between July 29, 2009 and August 8, 2009 and was specifically devoted to investigate the activity at the SW vent (Fig 3.3 b), while the second one between September 29, 2009 and October 10, 2009 investigated the activity at NE vent (Fig 3.3 d).
In both cases a reference station (RIF) was installed at Pizzo (Fig 3.3a,c) at a distance of 280 m from the active vents and with a perfect line – of – sight.
The RIF station was equipped with two differential pressure sensors: 1) one with a Pressure range of ± 250 Pa (Honeywell DC001NDC4), i.e. the same as at the seismo – acoustic stations of the Network, and the other with a Pressure range of ± 2500 Pa (Honeywell DC010NDC4). Data were collected with 24 bits A/D converter, and at a sampling rate of 100 Hz.
The propagation of acoustic wave from the vents to the reference station is in direct line of sight, without any obstacle along the path (Fig 3.8). Therefore, the acoustic pressure, measured in air with perfect weather conditions (dry, sunny, and without wind), is only due to the energy release by the source and to the distance from the source (280 meters), because the absorption coefficient in air is sufficiently small to be considered negligible (see in section 2.1.2).

3.2.1 The SW crater source

Volcanic activity during the first experiments, was characterized by a medium-size strombolian activity, with explosions occurring at a mean rate of 12 per hour, and localized with the infrasonic array at the SW Vent (Fig 3.3b). We selected 135 explosions of the SW Vent, with a good signal-to-noise at ratio at all the 5 stations, were 135 (Appendix, Fig. A.1 – Table A.1). The waveforms recorded at the reference station were all similar, and consisted in a nearly one second long transient characterised by impulsive compression onsets with a positive pulse duration around 0.12 s (Fig 3.4a), and by a peak frequency of about 3.8 Hz (Fig 3.4b), which results in a wavelength of about 89 m.

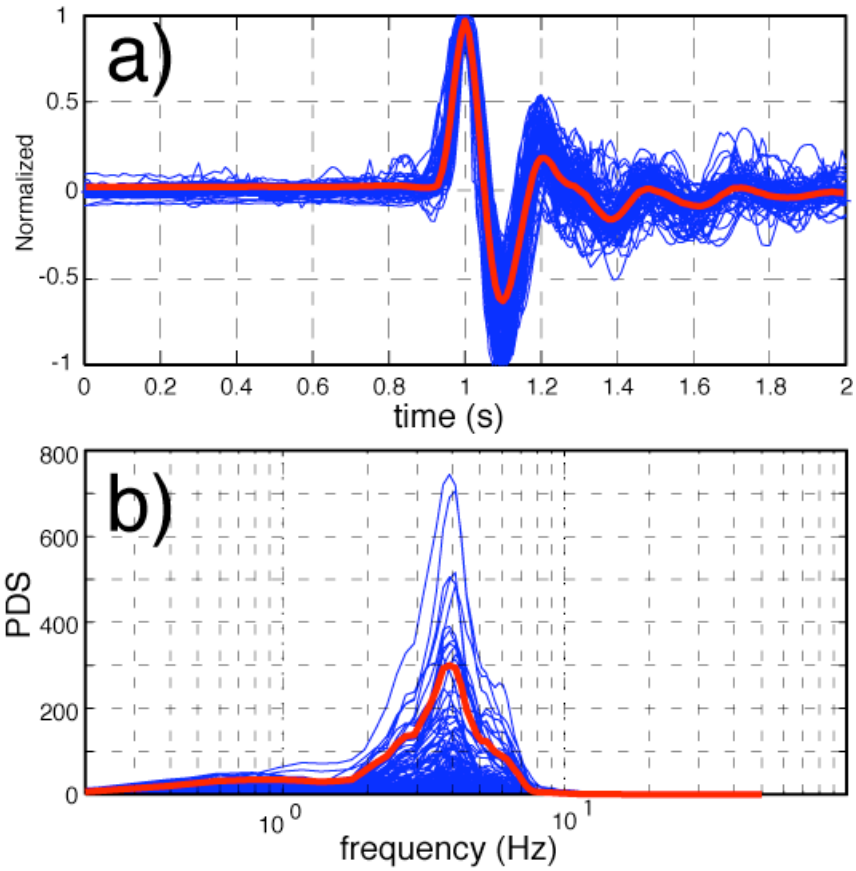

Fig 3.4. a) The 135 Pressure waveforms recorded at the reference station during experimental measurements, and b) Their spectral content closely grouping at 3.8 Hz.

The acoustic pressure recorded at the reference station ranges from 298 Pa to 24 Pa (Fig. 3.5a). The pressure peak for the recorded waveforms exhibit a sharp decrease moving from station RIF to the other stations (Fig 3.5a). Amplitudes at SAS, STR, ROC, SCI are reduced by a factor of 2.6, 3.6, 2, 3.2, respectively (Fig 3.4b). In addition, the peak amplitudes recorded at ROC and STR stations, show an inverted pressure decay (Fig. 3.5a), with pressure values higher at ROC, located at distance from the source greater than at STR station.

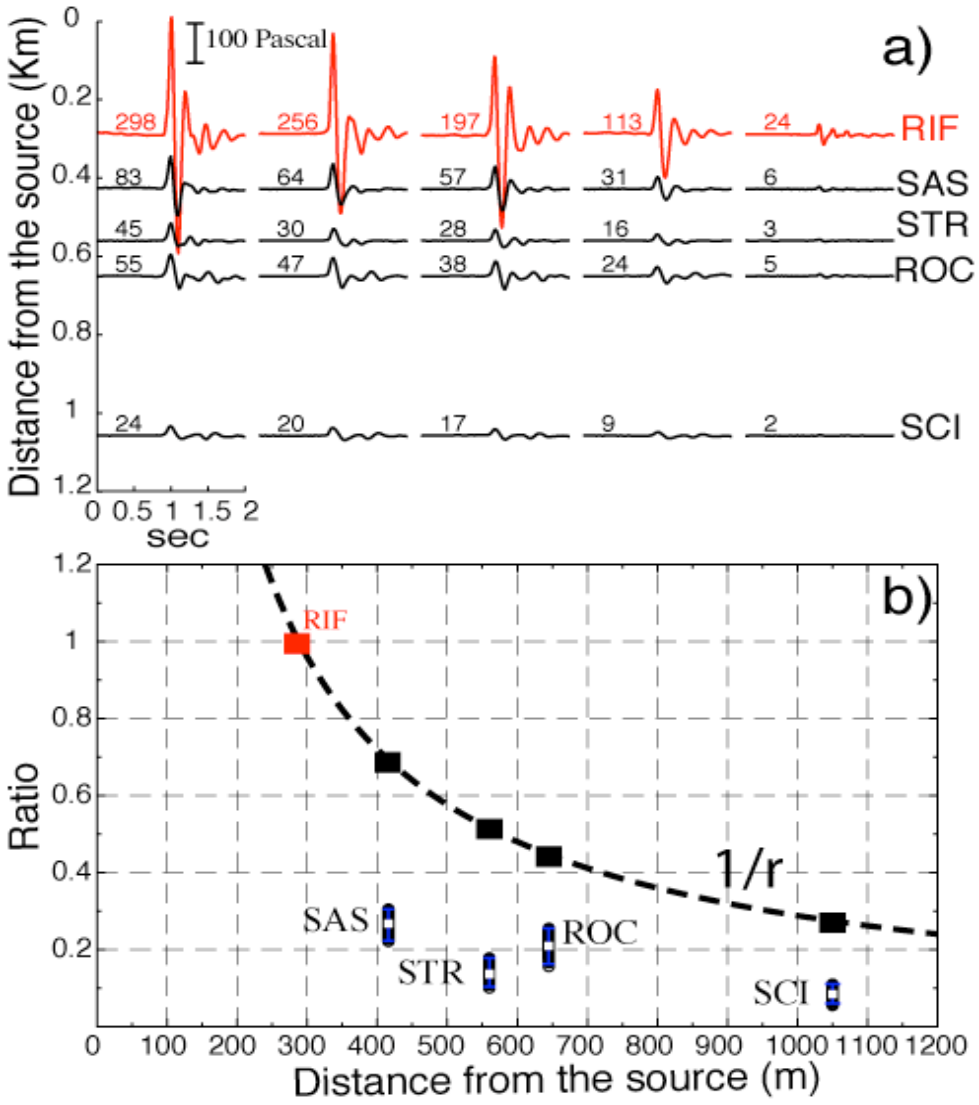

Fig 3.5. a) Pressure waveforms at the 5 recording stations positioned on the crater rim to enhanced the experimental measurements relative to the SW vent source. Their amplitudes are represented in an ascending order, opposite to distances from the source, and labelled with the peak absolute pressure in Pa. b) Ratio of the peak amplitude between the network stations and the reference station for all 135 analysed explosions; the dashed lines is traced through the corresponding values calculated for the same stations, as a function of attenuation for geometrical spreading (1/r).

3.2.2 The NE crater source

A second experiment was performed during the 12 days long period at the end of September 2009, when the explosivity at the NE crater was quite intense, with explosions occurring at a mean rate of 8 per hour. The infrasonic array recorded the 39 explosions with a good signal to noise ratio at all the 5 stations. (Appendix, Fig. A.2 – Table A.2). At the reference station all the signals were very similar to each another, and consisted in nearly one second long transients. They were all characterised by impulsive compression onsets with a positive portion of the pulse lasting around 0.09 s (Fig 3.6a), and by a peak frequency of about 4.3 Hz (Fig 3.6b), which results in a wavelength of about 79 m.

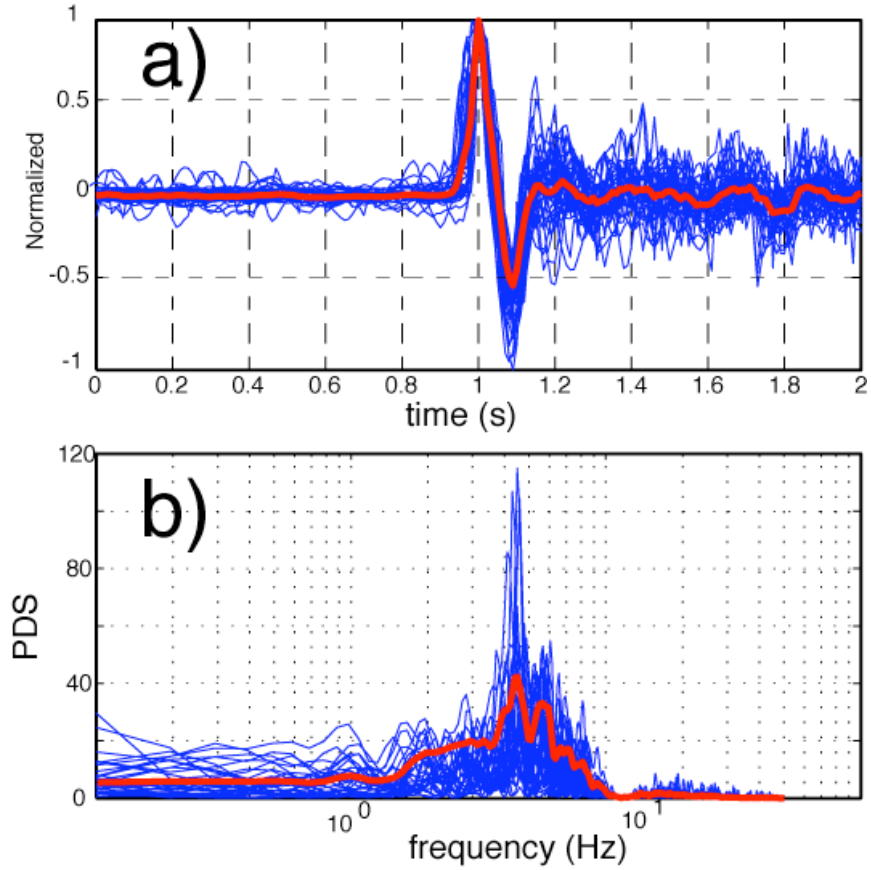

Fig 3.6. a) The 39 Pressure waveforms recorded at the reference station are visualized as normalised for a 2 second duration and their average trend summarised by the red line. b) The spectral distribution of each of the 39 waveforms is clustered around a bimodal distribution, peaked at 4.3 Hz.

Acoustic pressure recorded at reference station ranges from of 41.3 Pa to 16.3 Pa (Fig 3.7a). Pressure propagation exhibit a sharp decrease from RIF station to SAS, STR and SCI stations (Fg3.7ab) and they are reduced by a factor 3.5, 2.5, 1.8 relative

to the amplitude decay for geometrical spreading; in contrast, in the ROC Station the amplitude decay closely follows that of a geometrical spreading. The peak amplitudes recorded at the ROC and SAS stations, show inversion in the decay (Fig3.7 ab), with higher pressure value at ROC, located at a greater distance from the source than SAS. The peak amplitude recorded at SCI, at ~1000 m of distance from the source, is comparable whith these recorded at SAS at only 420 m from the crater but beyond the topographical barrier of Pizzo (Fig 3.8).

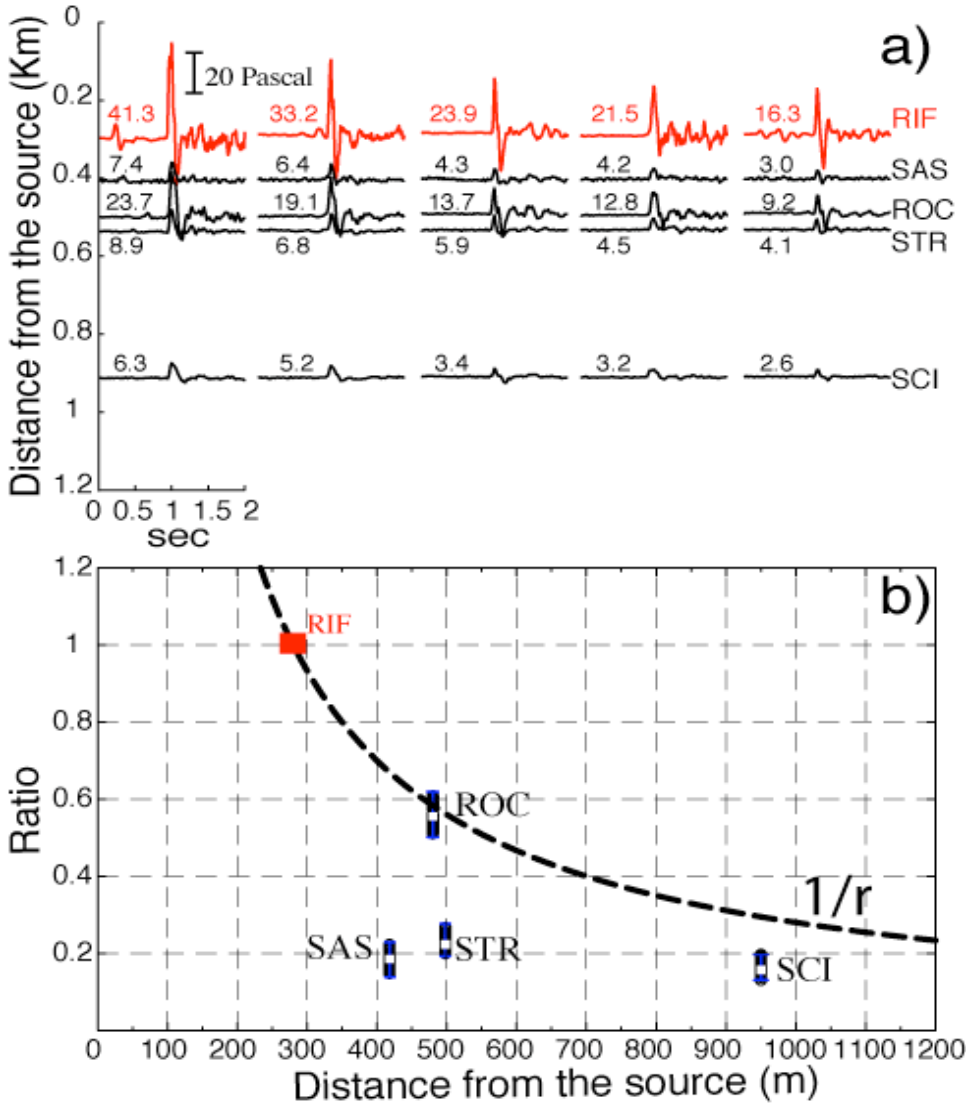

Fig 3.7. a) The recorded pressure waveforms during the experimental using the NE vent source. On each column contains the waveforms recorded at 5 the stations for the same explosion. The waveforms are ordered with ascending the distances from the source, and labelled with the peak absolute pressure in Pa. b) Ratio of the peak amplitude between the network stations and the reference station for all 39 explosions, dashed lines is the function of attenuation for the geometrical spreading (1/r).

3.3 Waveform comparison

The attenuation produced on the infrasonic waveforms, recorded during both acquisition campaigns, indicates a decay markedly greater for stations SAS, STR and SCI, relative to the amplitude decay inferred only for geometrical spreading of an infrasound waveform (Fig 3.5ab, Fig3.7ab).
Besides, the attenuation values for two sources at the same stations are different indicating that the position of the source has strong influence on the amplitude of the recorded waves.
The travel path of the infrasonic waves from the SW and NE vents and the 4 stations is actually blocked by the presence of topographical barriers, namely Pizzo for SAS and STR stations and Bastimento for the SCI station. These barriers may cause a shadow zone and induce diffraction effects on the wave field (Fig3.8).

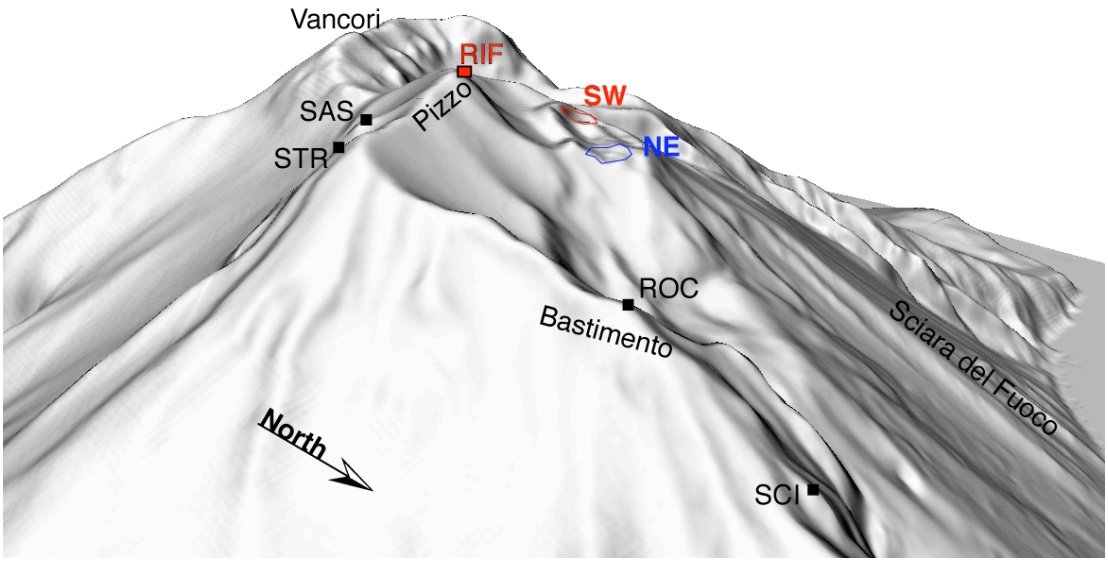

Fig 3.8. Drawing of a 3D map of Stromboli with disposition of stations on the summit .

The effects of diffraction are evidenced also by a the deformations of the negative rarefaction part of the infrasonic wavefield. Infect, comparison of normalized and stacked waveforms recorded at RIF, SAS and STR stations shows clearly that the diffracted wave is acting also a low-pass filter (Fig3.9). The peak pressure in the shadow zone is lower than what expected in a geometrical spreading (Fig3.5ab), and the duration of the signal becomes longer (Fig 3.9a). Both changes are typical characteristics of a low – pass filtering in time domain. Spectra calculated for these waveforms (Fig 3.9b) show that frequency components of 3.8 Hz and higher are reduced to one half of its magnitude in the shadow zone, while the spectral amplitude increases at lower frequency. This low - pass filtering effect is visible also in

previously higher frequency measurements (*C.G. Don, 1991, Papadopoulous and Don 1991*) and agrees with predictions of insertion loss from simple barrier diffraction theories (*A.D. Pierce, 1989*).
The waveforms of the ROC and SCI stations, located on the North east flank of the crater terrace (Fig 3.8), show a coda wave longer than the other tree stations of the Network and have a similar spectral shape (Fig 3.9ab), with peak frequencies shifted to a lower frequency for SCI station. The same behavior is observed for waveforms recorded from the NE vent (Fig 3.10ab). Both figures, 3.9ab and 3.10ab, indicate how the wave field is modified along different paths between station RIF and the Network stations, causing thus the loss of the source parameters.

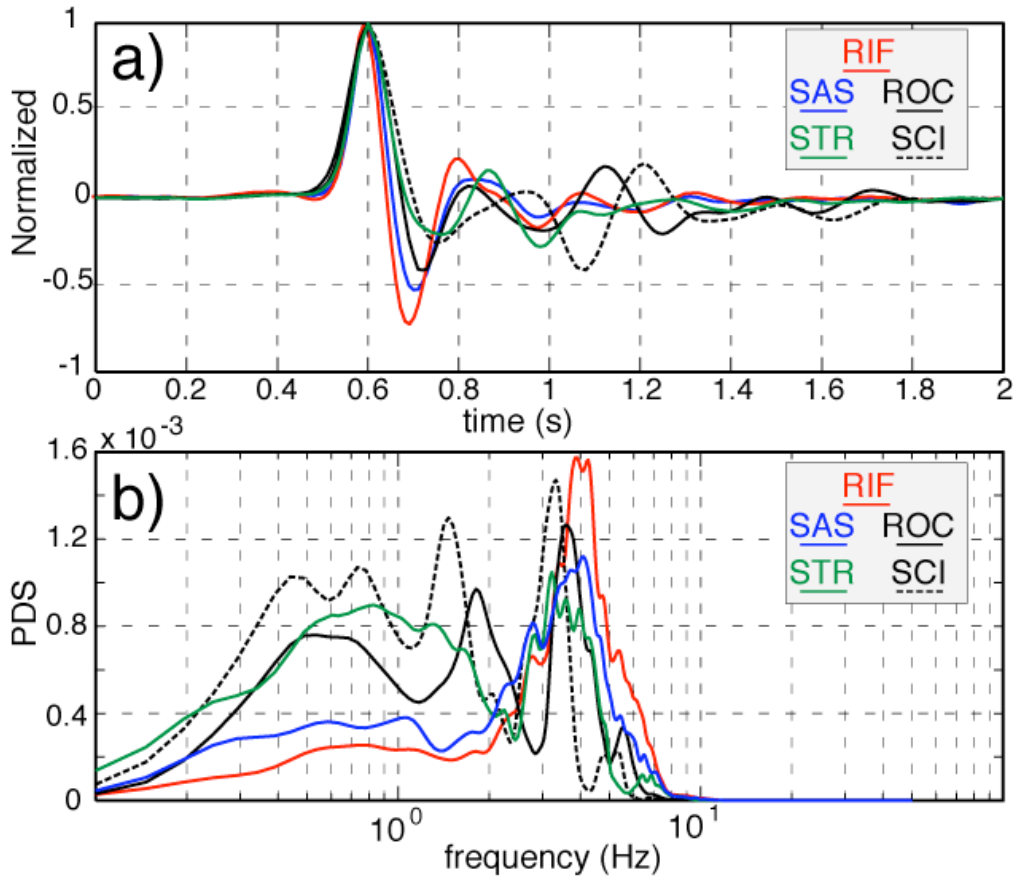

Fig 3.9. The low pass filtering effect produced by diffraction around the Pizzo Hill.a) Infrasonic waves obtained from the stacking of the infrasound records related to the explosions at the SW crater (Appendix, Fig. A.1), whose positive duration is 0.12 seconds for RIF, and increases to 0.18 and 0.21 sec for SAS and STR respectively. b) power spectral densities of the waveforms. The SAS and STR waveforms have far less high – frequency content than that at the RIF.

At the ROC station, in the case of explosions localized to arrive from the SW crater, pressure values reduced by a factor 2 above geometrical spreading are recorded (Fig

3.5), while for explosions of the NE crater, the peaks pressures decay with the law of geometrical spreading (Fig. 3.7). This phenomenon can be explained by the position of the ROC station relative to the two vents. In the first case, the ROC station is not in line - of - sight with the source because it is located at a height of nearly 80 meters lower than the crater terrace, while the first arrival recorded at ROC station is a direct wave for a provenance from the NE crater (Fig3.8). Therefore, even if the peak amplitude of waveforms arriving at the ROC station from NE vent decay according to the geometrical spreading as it occurs for the RIF station, their waveforms are not similar showing a positive duration longer and a peak frequency lower (Fig 3.10ab) for the ROC station. This is indicating that the peak amplitude may decay with the geometrical spreading rate, but the shape waveforms depends from the path, which may generate scattering or reflections changing the waveform shape.

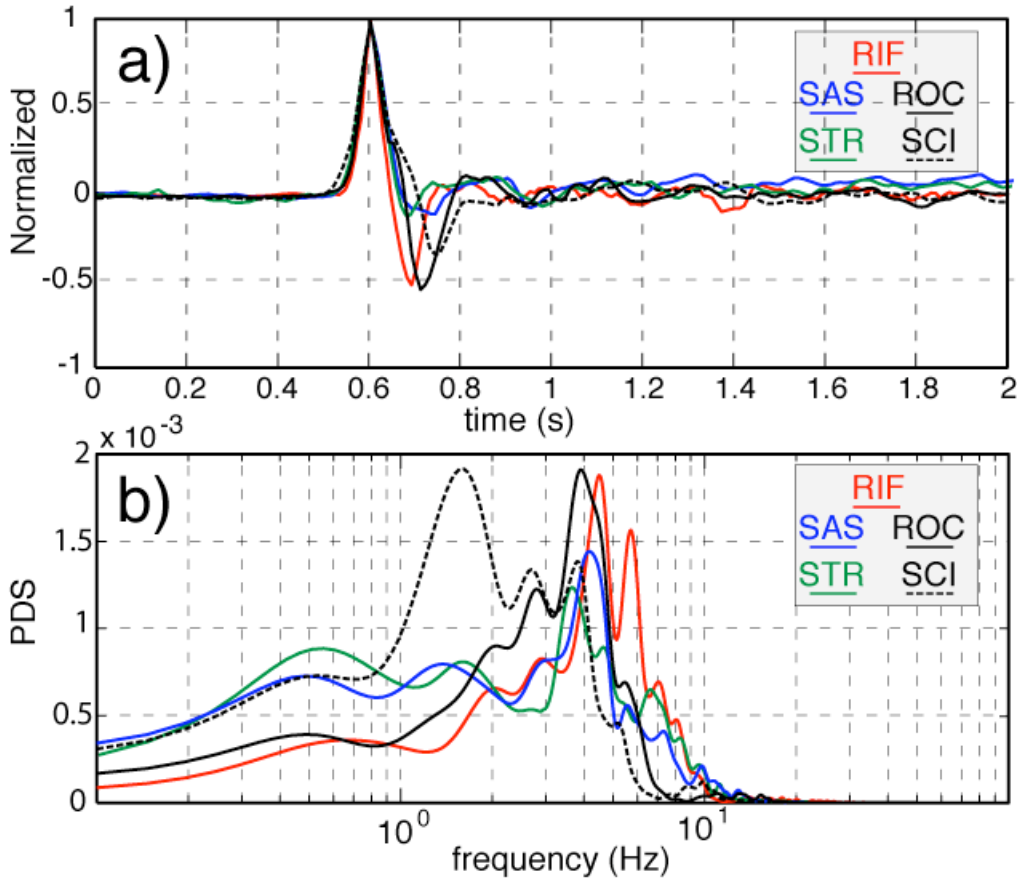

Fig 3.10. Measurements of the low pass filtering effect on the arrivals at the five recording stations, introduced by diffraction of their wave – paths around the Pizzo Hill. a) Stacking of the whole recorded of infrasonic waves produced by explosions at NE vent (Appendix, Fig. A.3); their positve amplitude assumes different durations, being for instance 0.09 seconds for RIF station, and increasing up to 0.11 and 0.12 sec for SAS and STR stations, respectively. b) The power density spectra of the previous waveforms contain a far bigger amount of low frequencies in the recordings from the array stations than that of the RIF waveform.

Finite – Difference Time Domain Modelling

Acoustics plays a key role in volcano monitoring. However, a proper inversion of the infrasonic wavefield needs a detailed analysis of the propagation effects. It is well known that the infrasound wave is affected by complex sound propagation phenomena, such as reflections, diffractions from ground interactions and refractions by wind and temperature gradient.
Each of these phenomena could introduce large distorsions in the acoustic wavefield, which should be taken in account for a proper inversion to the source parameters.
The studies of the effects of this phenomena on the field are extremely difficult and expensive to perform.
Therefore, a theoretical simulation able to quantify the amount these phenomena and to evaluate their effects on waveform would be crucial for understanding sound propagation in a complex environment.
Most currently used numerical methods for outdoor sound propagation, such as fast field program (FFP) and parabolic equation (PE) are incapable of simulating all of the propagation phenomena mentioned above *(Attenborough et alii 1995, Salomons 2001*).
On the other hand, many of these phenomena are readily handled with Finite Difference Time Domain (FDTD) technique.
In recent years, FDTD has gained popularity in simulating different wave propagation in complex systems *(Stepheen 1988, J. Virieux 1984, S. Wang 1996)*.
Among the advantages of the finite difference method there are its capability to include a variety of acoustic source function, complex barriers such as buildings, and spatially varying sound velocity. Moreover, FDTD allows the viewing of the computational results in an animated movie fashion, as this may provide insights in to the complex wave propagation phenomena arising from the interaction of the waves pathways with obstacles.
Nevertheless, there are significant drawbacks of finite difference time domain that include implementing a time domain impedance boundary conditions for the ground and controlling numerical instabilities and sudden contrast in material properties.

It will be shown how the conclusive results may assume a robust constrains on the quantitative solution, of the mentioned problems, given the flexibility of the FDTD technique and the increasing capability of modern computers in outdoor sound propagation modelling.
In this chapter, the equations for sound propagations in a non – moving medium and in a two – dimensional plane will be applied to the topographical section of Stromboli. The finite difference method is based on the expressions of acoustical propagation as a set of first order velocity – pressure coupled differential equation.
The basic technique is to divide the spatial domain into a discrete grid of nodes and to approximate the derivatives appearing in the equations of motion using finite differences between adjacent grid values. Similarly, the time variable is also divided into discrete steps and evaluated using finite differences *(Yee, 1966)*.

4.1 The finite – difference method

The FDTD-method is presently a well known and versatile method for simulating many problems in different wave propagation in the time domain for the one, two or three dimensional space. The finite difference time domain method was introduced by Yee, in 1966, to study electromagnetic wave propagation *(Yee, 1966)*. The method employs a discretization of time and space to express the coupled first – order Maxwell's equations as difference equations. In this case the acoustic propagation is based upon basic motion equation and the equation of continuity.
In a 2-D Cartesian coordinate system, the wave pressure p and the horizontal and vertical particle velocity u e v, respectively satisfy the following equation *(J. Virieux, 1984, S. Wang, 1996)*:

$$\frac{\partial p}{\partial x} = -\rho \frac{\partial u}{\partial t} \tag{4.1}$$

$$\frac{\partial p}{\partial y} = -\rho \frac{\partial v}{\partial t} \tag{4.2}$$

$$\frac{\partial u}{\partial x} + \frac{\partial v}{\partial y} = -\frac{1}{\rho c^2} \frac{\partial p}{\partial t} \tag{4.3}$$

Where ρ is the density and c is the velocity of the medium.

To derive into finite difference form these partial differential equations, time and space need to be both discretized. The lattice spacing δ of the grid should be sufficiently small, to give on adequate sampling density.
Therefore, the first order partial derivatives of a field parameters *f(x, y; t)* relative to *x* and *y* can be approximated as the following central differences:

$$\frac{\partial f(x,y;t)}{\partial x} \rightarrow \frac{1}{2\delta}\left[f^{(n)}(i+1,j) - f^{(n)}(i-1,j)\right] \quad 4.4$$

$$\frac{\partial f(x,y;t)}{\partial y} \rightarrow \frac{1}{2\delta}\left[f^{(n)}(i,j+1) - f^{(n)}(i,j-1)\right] \quad 4.5$$

Central differences provide a second order accuracy compared to the biased differences. Similarly, the partial derivative of *f(x, y; t)* relative to *t* can be approximated as:

$$\frac{\partial f(x,y;t)}{\partial t} \rightarrow \frac{1}{2\Delta t}\left[f^{(n+1)}(i,j) - f^{(n-1)}(i,j)\right] \quad 4.6$$

Here, following Yee's annotation where *i* and *j* are the spatial indices representing discretized *x* and *y* respectively, and *n* is the temporal index, and substituting these differences expressions into equations (4.1, 4.2, 4.3), the following recurrence relations are obtained:

$$u_{i+1/2,j}^{n+1/2} = u_{i+1/2,j}^{n-1/2} - \frac{\Delta t}{\rho_{i,j}\delta}(p_{i+1,j}^{n} - p_{i-1,j}^{n}) \quad 4.7$$

$$v_{i,j+1/2}^{n+1/2} = v_{i,j+1/2}^{n-1/2} - \frac{\Delta t}{\rho_{i,j}\delta}(p_{i,j+1}^{n} - p_{i,j-1}^{n}) \quad 4.8$$

$$p_{i,j}^{n+1} = p_{i,j}^{n} - \Delta t \rho_{i,j} c_{i,j}^{2}\left(\frac{u_{i+1/2,j}^{n+1/2} - u_{i-1/2,j}^{n+1/2}}{\delta} - \frac{v_{i,j+1/2}^{n+1/2} - v_{i,j-1/2}^{n+1/2}}{\delta}\right) \quad 4.9$$

The staggered Cartesian grid used in Equations (4.7, 4.8, 4.9) is sketched in Figure 4.1. Equations show how new values of pressure and particle velocity are obtained from previous values on the staggered grid.

There are two steps to determine the size of grid and the length of time steps to warrantee numerical stability when implementing the FDTD algorithm. First, for a second order finite difference, as in this study, 20 spatial nodes for the main wavelength considered are needed to suppress unwanted numerical dispersion.

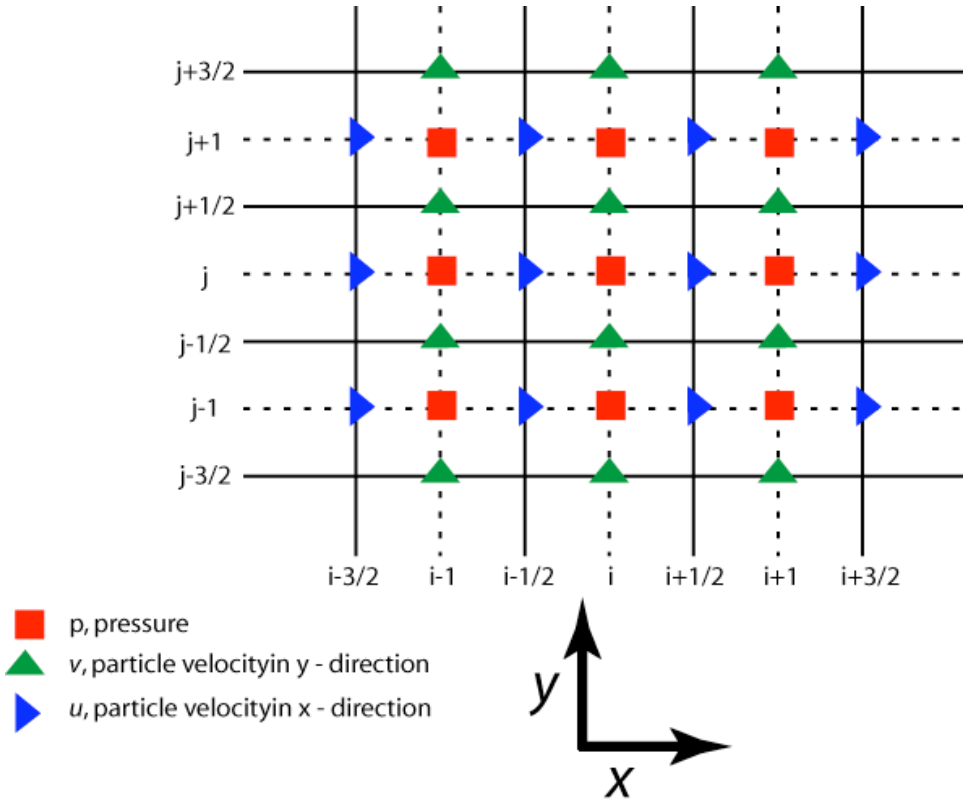

Fig 4.1. The sketch of the two – dimensional staggered grid system in the x – y plane used for the present simulation of the acoustic field by the finite – difference method. The index i is used to indicate x coordinates, and the index j to indicate the y coordinates.

Next, for a given lattice grid size δ, the time step must meet the theoretical Courant stability criterion *(S. Wang, 1995)*

$$\Delta t \leq \frac{\delta}{c\sqrt{2}} \qquad 4.10$$

for the two dimensional case.

However, for problems involving materials having a high impedance contrast, the Courant conditions of the equation may not be sufficient to reach the numerical stability. A more robust stability criterion, with a much smaller time step, has been then applied to the our calculation by the term

$$\Delta t = \frac{\delta}{16c} \tag{4.11}$$

and this will be discussed further below, following what introduced by Liu and Albert*, (2006)*.

4.1.1 Two dimensional approximation

Solution of the finite difference equations, discussed in the previous section, requires a very fine spatial grid for accurate results. This requirement normally limits finite difference calculations for sound propagation problems to super computers. To reduce the computational time and to make manageable the problem on a personal computer, its actual three-dimensional solution is simplified to the two-dimensional case, which still keep a sufficiently good approximation. The two- dimensional model has substantial benefits but also introduces a certain number of approximations and limitations to the numerical solution. While the kinematics of solution (e.g. the speed and the arrival times) remain accurate, the propagation dynamics (pressure amplitudes) differs from the three – dimensional situation and must be corrected if the solution is to be compared to real measurements (*D. Albert et al., 2005*).

While in the real physics world, a pressure point source generates a spherical acoustic wave with a geometrical spreading of 1/r, in the two – dimensional model a line source is used. For a line source, the shape of the wavefront is a cylinder, and waves are called cylindrical waves. Let's imagine two wave fronts, which make 2 cylinders with the same axes (Fig 4.2). The radius to the outer cylinder is r_2, and greater than that of the inner cylinder r_1 . Thus, the surface areas of the outer S_2 and inner S_1 cylinders are $4\pi r_2 L$ and $4\pi r_1 L$, respectively.

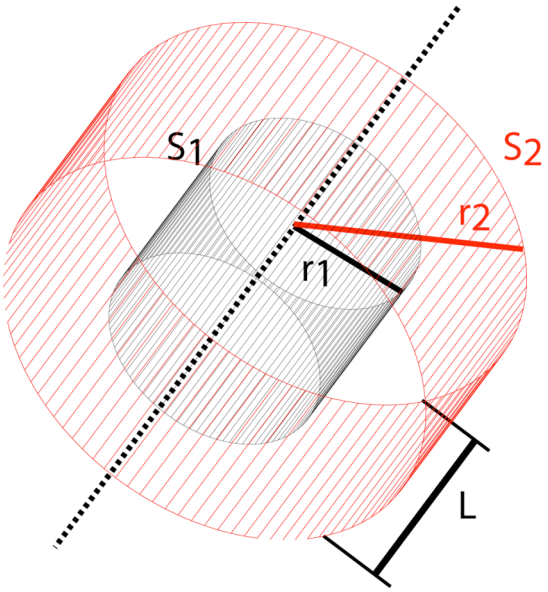

Fig 4.2. Representation of the two cylindrical wave fronts to which the considerations discussed are referred.

It can be noted that the total energy flowing through the outer and inner cylinder at a given time should be the same, according to the principle of energy conservation. Therefore:

$$E_2 = E_1 \tag{4.12}$$

$$I_2 S_2 = I_1 S_1 \tag{4.13}$$

$$I_2 4\pi r_2 L = I_1 4\pi r_1 L \rightarrow I_2 = \left(\frac{r_1}{r_2}\right) I_1 \tag{4.14}$$

where I is Energy intensity, that is the total energy E_{total} flowing through a unit area dS in a unit time dt, and thence

$$I = \left(\frac{E_{total}}{dSdt}\right) = \frac{EcdtdS}{dSdt} = Ec = \frac{1}{2}\rho\omega^2 A^2 c \tag{4.15}$$

where ω is the angular frequency, c is the propagation velocity of the wave, A is the amplitude of the wave and ρ is density of the air. Substituting equation 4.15 in 4.14 we have:

$$\frac{1}{2}\rho\omega^2 A_2^2 c = \left(\frac{r_1}{r_2}\right)\frac{1}{2}\rho\omega^2 A_1^2 c \tag{4.16}$$

$$A_2 = \sqrt{\frac{r_1}{r_2}} A_1 \tag{4.17}$$

The amplitude decay with $1/\sqrt{r}$ for waves generated by a line source, being the shape of the wavefront cylindrical, is generally referred as the geometric spreading for cylindrical waves. Thus the two-dimensional modelling results are renormalized by an factor of $1/\sqrt{r}$.

4.1.2 The source function

Infrasound represents the time history of the atmospheric pressure perturbation (Δp) relative to the background atmospheric pressure. The excess pressure, measured at a distance of 280 meters from vents (Fig 3.5, Fig 3.7), is in the order of 10^1 - 10^2 Pa, that compared to atmospheric pressure (~ 10^5 Pa) is very small. Thus, the infrasound signal can be treated as linear elastic waves rather than non – linear shock – wave. Infrasound recorded at Stromboli have 3.8 and 4.3 Hz frequency content (Fig 3.4, Fig. 3.6), that generates a wavefield with a wavelengths of ~ 90 m. - 80 m., i.e. larger than the source dimension, usually inferred for the vents of 4 -10 m. in diameter. It, then, allows to approximate the source as a point, which radiates isotropically.
According to the linear theory of sound excess pressure due to an acoustic monopole source *(Lightill, 1978),* the pressure perturbation is represented as follows:

$$\Delta p = \left(\frac{1}{2\pi r}\right)\left[\frac{dq\left(t + r/c\right)}{dt}\right] \qquad 4.18$$

where *q(t)* is the mass flux from a point source.
Fig 4.3 shows a synthetic acoustic pressure trace calculated according to equation 4.18.

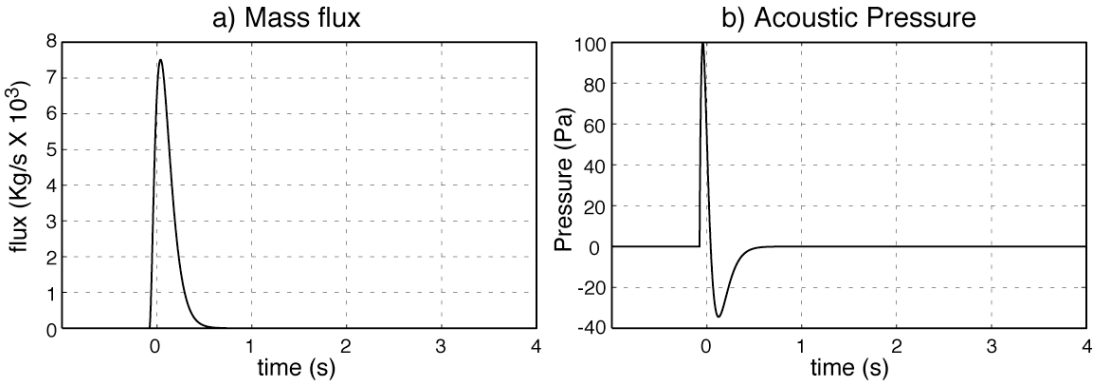

Fig 4.3. The diagrams representing the function of mass flux of the gas, in (a) and the synthetic acoustic pulse, in (b), where the generation of a transient acoustic pressure pulse is due to the gas release from a point source. The arbitrary mass flux (a) is intended to represent a rapid degassing onset followed by more gradual tapering. In (b) transient pressure pulse is calculated according to equation 4.18. *(Lightill, 1978; Johnson, 2000).*

The waveform source shown in Fig 4.3b may be modelled as a theoretical blast wave source presented by Reed *(1977)*. The equation referred above is the analytical expression for the source pressure as a time function:

$$p(t) = A\left(1 - a\left[ft - b\right]^2\right)\exp\left(-cft\right) \qquad 4.19$$

where *p(t)* is the source waveform at time *t*, *A* its amplitude, *a*, *b* and *c*, are fixed to determine the delay, rise time, and amplitude of negative peak of the source waveshape, and *f* is the central frequency of the pulse (*Reed, 1977*).
The flexibility of equation 4.19 as source function allows to simulate in the finite difference method a wavefront consistent with the measured one. Values for 3.8 Hz and 4.3 Hz have been used to produce the source waveforms for FDTD simulations at the SW and NE vents respectively (Fig 4.4).

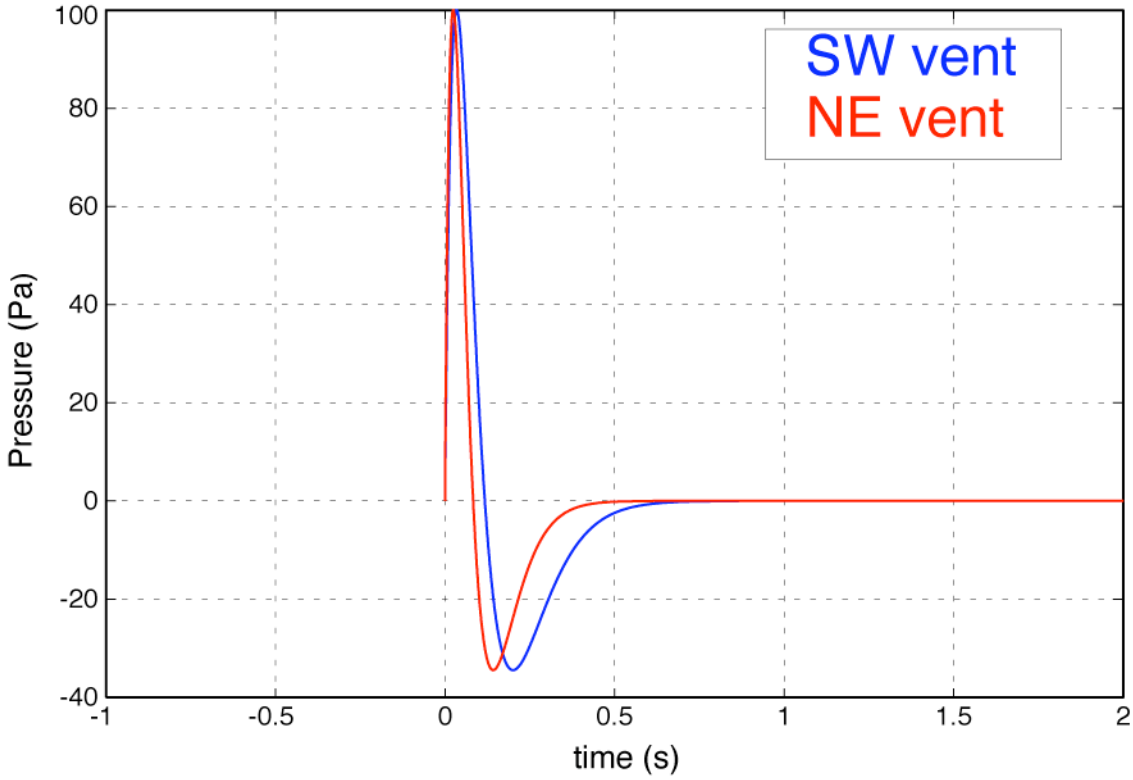

Fig 4.4. The shape of the pulses sources used in the finite – difference calculations calculated from equation 4.19 with the parameter values of f = 3.8 Hz (blue line) and f = *4.3* Hz (red line) for SW and NE vent, respectively, a =25, b = 1/5 and c = 5.

4.1.3 Parameters used in the simulations

The boundary conditions for a free surface topography are closely following the study of Liu and Albert *(2006)*. The rock of Stromboli has a nominal density of 2700 Kg/m^3 and an acoustic wave velocity of 1600 m/s *(Ripepe and Braun, 1994)*. The air has been considered a homogeneous and non-moving fluid, density of the 1.2 kg m^{-3} and sound velocity of 340 m s^{-1}. The resulting very large impedance contrast with air requires stability condition stronger than the classic Courant condition *(Schroder and Scott, 2002)* so that the final selections of grid size and time step were determined on the impedance contrast between the media. However, the simulation becomes too heavy and unrealistically expensive in terms of CPU time.
To avoid these problems, contrast must be reduced to a manageable level. In these simulations, therefore, the density contrast is limited to nearly 1/20 instead of the true ratio of 1/2000, drastically reducing the density of the topography from 2700 Kg/m^3 to a value of 27 Kg/m^3. Physically, this change does not affect the arrival times of the wavefront or the propagation behavior. Using, a lower density for topography it reduces the impedance ratio for approximately 15000 to about 150, and slightly change the reflection and trasmission coefficients. For example, the true normal reflection coefficient value of 0,99994 will be replaced by a value of 0.98974, about a nearly 1% change in reflection coefficient *(Liu and Albert, 2006)*.
As just above mentioned, these solutions have been assumed following Schroder and Scott *(2002)*, who pointed out how a high impedance contrast may introduce numerical instabilities in the finite difference solution.
Three steps have therefore been taken in the calculations presented here to eliminate these instabilities *(Ilan and Loewenthal, 1976)*.
First, the impedance contrast between air and topography was reduced by lowering the density of topography, in order to reduce the impedance ratio from 150000 to 150, still maintaining unaltered the reflection coefficient and wave velocities.
Secondly, the grid layer at the air – topography boundary uses the average impedance between air and topography instead of the full impedance contrast.
Finally, the time step is reduced from the classical Courant condition given in equation (4.10) to the much more robust condition of equation (4.11).
We will slow how better this values are able to make a simulation with high stability and good accuracy. Rigid boundaries may introduce complications in the discretization of complex geometries and can cause further numerical instability and then were not included in the calculations.

4.2 Simulations

We apply this method to the topography profile of Stromboli intersecting the infrasonic stations of RIF, SAS, STR, ROC, SCI and passing for the SW and NE vents (Fig 4.5 ab).

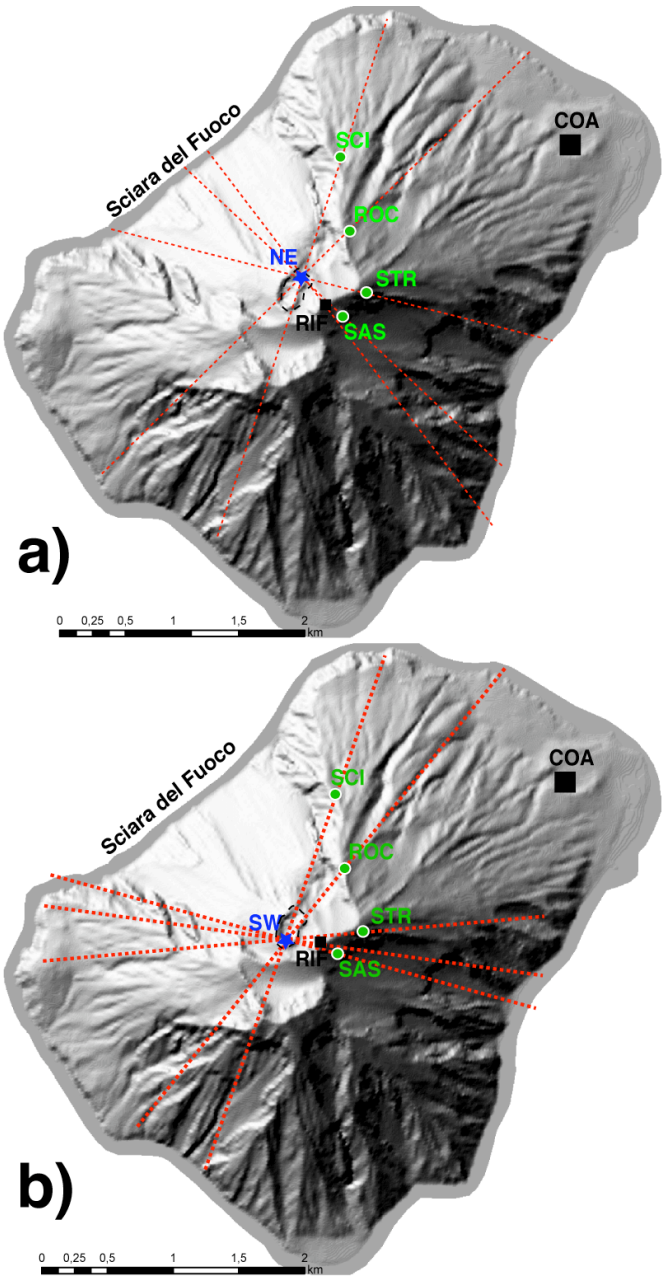

Fig 4.5. Map of Stromboli Volcano showing the position of the acoustic stations and five the topographic section with the sources locates at the NE crater (a) and the SW crater (b).

For each 2D simulation, a grid of 954 x 520 nodes was used with a of 5 m. spatial sampling; thus, the simulation area is 4770 x 2600 m. The time step was 0.919 milliseconds and the simulation ran for 7617 time steps, providing a total time window of 7 seconds (Fig 4.6). In the calculations, the topography was assigned a density of 27 Kg/m^3 and an acoustic wave speed of 2000 m/s, while of the air we used a density of 1.2 kg/m^3 and a sound speed of 340 m/s as discussed earlier. For the frequency band of less than 5 Hz and propagation distances shorter than 2000 m, as used here, the intrinsic absorption of the atmosphere is negligible and has been ignored (see section 2.1.2).

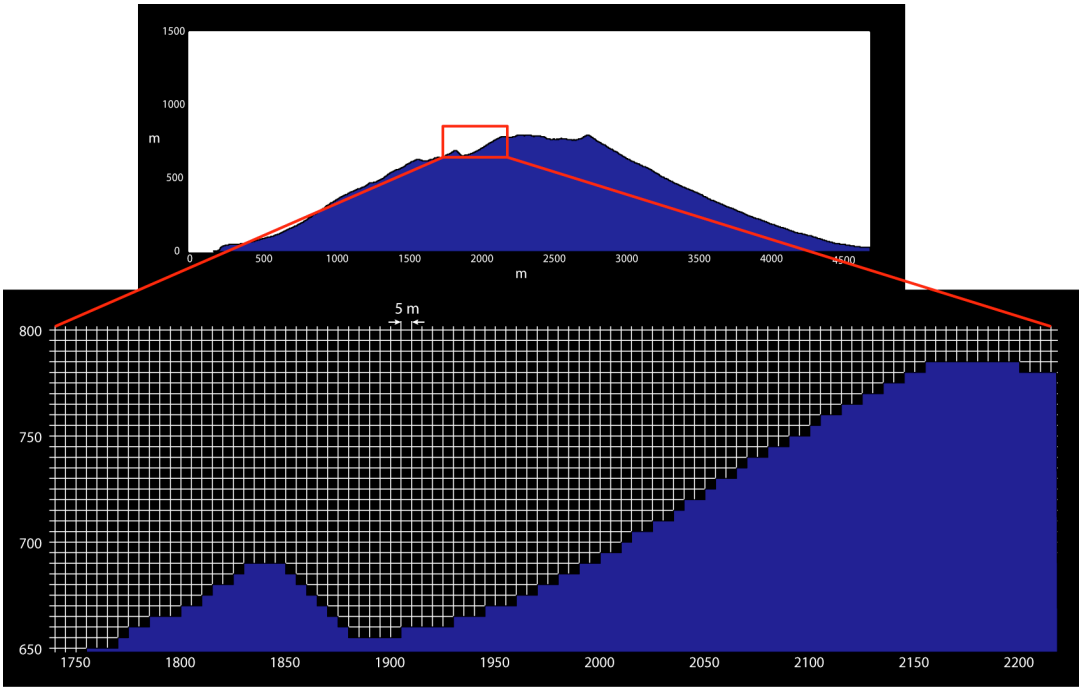

Fig 4.6. Sketch of the model setup for a two – dimensional solution. The staggered grid is discretized in a 5 meters spacing node distribution on the topographic profile through the summit crater.

4.2.1 Topographic effect of the Pizzo Hill

The main benefit of using finite difference method is the possibility of saving snapshots of the pressure wave field at each time step.
Assembling together a sequence of snapshots, a movie of wavefield propagation is produced. This is very useful for understanding the details of the waveforms recorded at any individual sensor.
Figure 4.7a shows some selected wavefield snapshots for the topographic section crossing the SAS station (fig 4.5). It can be seen how, the wave - front propagating

toward the SAS station (Snapshots 1.20 sec – 1.50 sec Fig 4.7a) is diffracting around the summit of Pizzo, producing a sensible amplitude decrease of the wave - front. While on other side of the source moving toward the point R (Right) (Fig 4.7 b), at the same distance of ± 420 m from the source origin amplitude is higher. Amplitude decays produced by the Pizzo is a factor of 1.4 compared to the virtual station R.

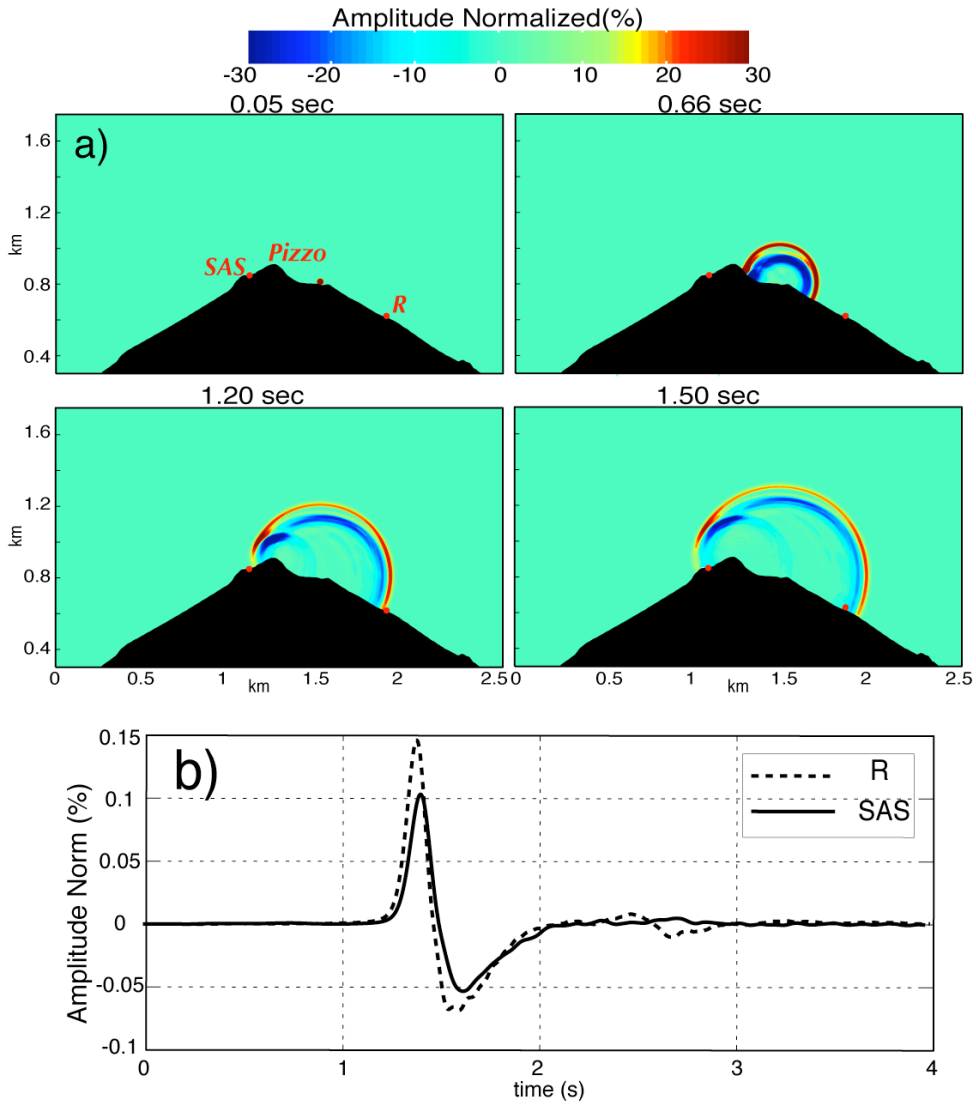

Fig 4.7. a) The movie frame generated using the finite – difference time domain method discussed in the text. Snapshots represent acoustic wave produced by a source positioned in the SW vent when encountering the actual obstacle of topography through Section SAS. The sound pressure is normalized to the maximum amplitude at the source. b) Synthetic time series of the same two stations located 420 m away from the source from either side of the previous simulation. The dashed trace (R station) has higher amplitude than the signal at SAS station located beyond the topographic barrier of Pizzo.

4.2.2 Source propagation from SW vent

The waveforms obtained from the simulations are fully shown in Appendix (Fig B.1, Fig B.3, Fig B.5, Fig B.7, Fig B.9) for a source positioned in the SW vent, and is here reported in Figure 4.8. We calculated by FDTD method the waveforms in absence of the topographic obstacle (dashed – line in Fig 4.8), using a flat rigid semi – space (Fig B.11).
The amplitudes are normalized to the peak amplitude calculated at the RIF station, and as expected decay with the geometrical spreading.
To assess acoustic performance, the insertion loss (IL) of the barrier (sometimes known as the attenuation, Att) is often used. The insertion loss is defined as it follows:

$$IL = 20\log\left(\frac{p_{w/o}}{p_w}\right) \qquad 4.20$$

where p_w and $p_{w/o}$ is the pressure with or without the presence of the barrier.
In the table 4.1 the insertion loss at the Network stations is shown.

Station	INSERTION LOSS (dB)
SAS	8.71
STR	10.85
ROC	5.57
SCI	8.51

Table 4.1. Insertion Loss calculated for the Network stations as the ratio of the peaks amplitudes of the waveforms with and without the topographic barrier, obtained by the FDTD method with source located at the SW vent.

The presence of the topographical barrier of Pizzo along the path between the source and the STR, and SAS stations (Appendix Fig B.3, Fig B.5) cause a higher attenuation value compared to the normal decay by geometrical spreading. Besides, this account for the pressure inversion between ROC and STR stations, with the amplitude at ROC resulting higher than at STR, although ROC is located at a greater distance than STR. The ROC station is not in line – of – sight with the SW vent, and acoustic path is obstructed by the edge of the crater terrace that generates the diffraction of the wave field, causing an insertion loss of 5.57 dB (Appendix Fig B.7).The acoustic wave field between the source and SCI station is also diffracted by the edge of the terrace crater and is also obstructed by the presence of the Bastimento ridge (Appendix Fig B.9) which brings the insertion loss up to 8.51 dB.

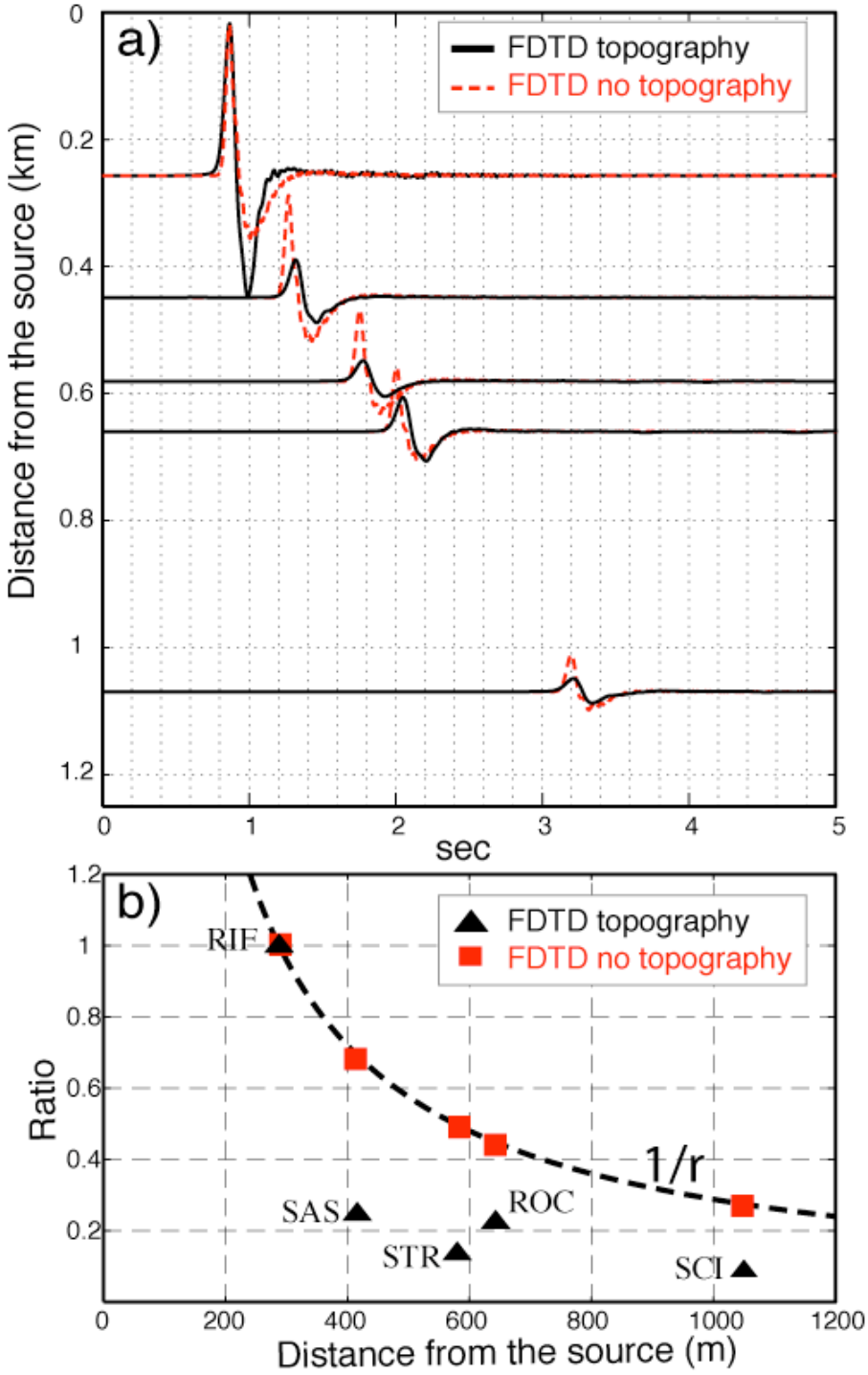

Fig 4.8. a) Comparison between waveforms calculated with the FDTD method in absence of topographic barriers in a half – space (dashed red line) and waveforms obtained with the topographic barrier (continuous line), for the source located at SW vent. b) Ratio of the peak amplitudes at the single stations and with the reference station (RIF).

4.2.3 Source propagation from NE vent

The waveforms in Figure 4.9 are the results of the FDTD wavefield simulations shown in Appendix B (Fig B.2, Fig B.4, Fig B.6, Fig B.8, Fig B.10) with the source positioned in the NE vent (Fig 4.9 a). Again, we calculated with the FDTD method the waveforms in absence of the topographic barrier (dashed – line in Fig 4.9), using a flat half– space, (B.12).
In this case acoustic amplitudes decay according to the geometrical spreading and show a higher value than when the topography is considered (Fig 4.9ab).
The Insertion Loss calculated for the Network stations as the ratio of peak amplitude of the waveforms with or without the topographic barrier is obtained by the FDTD method are and shown in table 4.2.
The presence of the topographical barrier along the path between source and the stations (Appendix Fig B.4, Fig B.6) causes higher attenuation values also in the case of a source located at NE vent.

Station	INSERTION LOSS (dB)
SAS	11.08
STR	5.93
ROC	0.04
SCI	3.41

Table 4.2. Distribution of the amplitude decay, the Insertion Loss in decibel, affecting the Network stations, calculated as the ratio of peaks amplitudes of the waveforms with or without topographic barrier. The simulation obtained by the FDTD method with source located at NE vent.

Differently from the previous simulation the ROC station, with the source locate at SW vent, is now in line of sight with the NE source (Appendix Fig B.8), and waves that decay following the geometrical spreading.
However, all the other stations present an amplitude attenuation higher than what expected induced by the irregular topography
The path between the source and SCI station is obstructed by the Bastimento ridge that generates diffraction of the wave field causing an insertion loss of 3.41 dB, that is an amplitude of nearly half (Appendix Fig B.10).

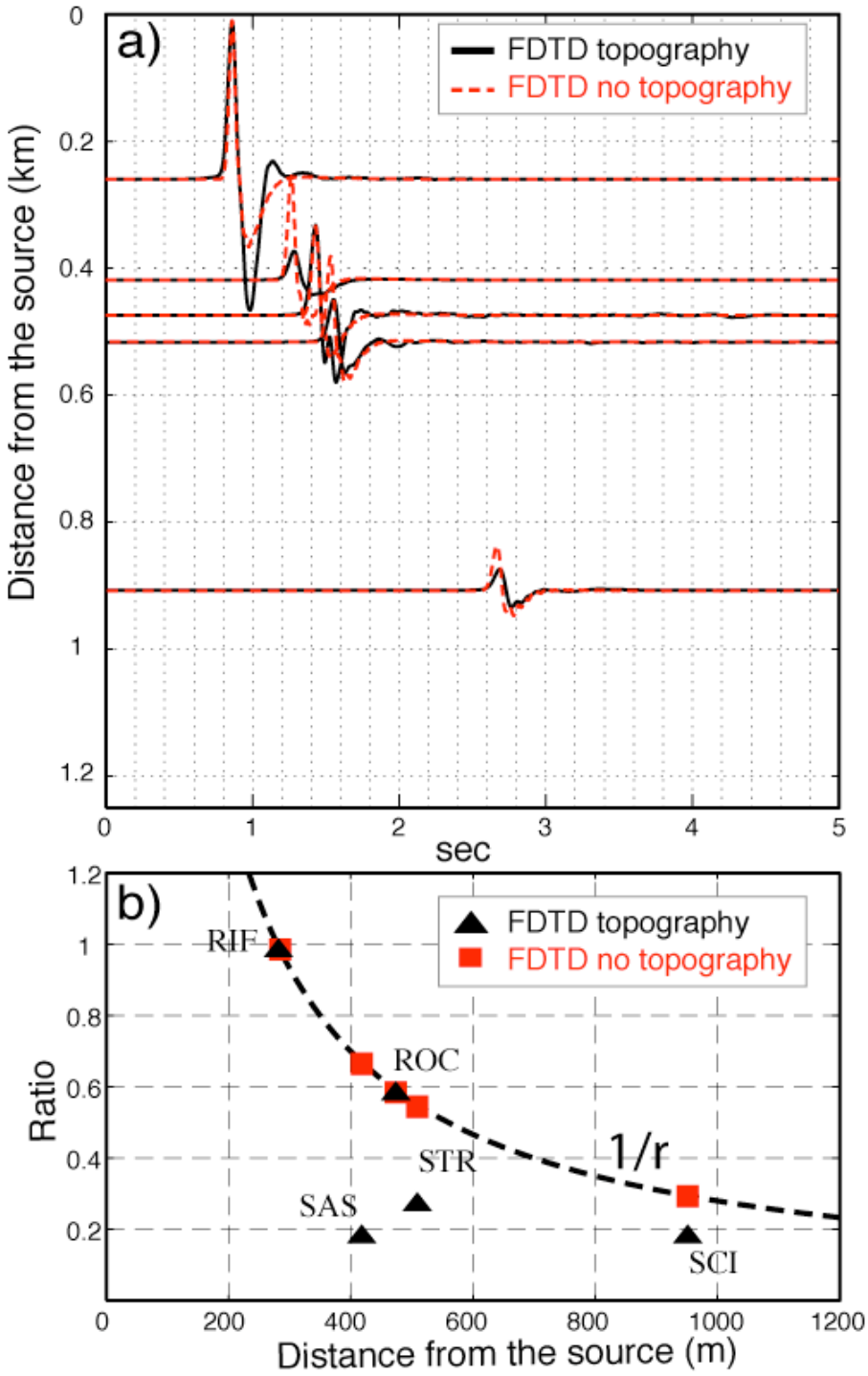

Fig 4.9. a) Comparison between waveforms calculated with the FDTD method in absence of the topographic barrier using a flat half space (dashed red line) and waveforms obtained with the topographic (continuous line), for the source located at NE vent. b) Ratio of the peak amplitudes for the waveforms shown in (a) between the stations and the reference station (RIF).

4.2.4 Theoretical pressure distribution

The FDTD simulation demonstrate how amplitude distribution with geometrical spreading can be altered by volcano topography (Fig 3.5b, Fig 3.7b). This insertion loss is generated by diffraction and reflection of wave field, producing a considerable attenuation of amplitude of acoustic pressure. The effect of Stromboli topography on the field pressure is determined numerically using finite – difference method.
The total effect of the volcano topography on the field pressure has been determined considering 18 topographic sections (one every 10 degrees from 10°N to 180° N) and crossing the two sources at the SW and NE crater.
The waveforms have been calculated, on 150 points every 20 m for each topographic section for a total of 3000 points on the volcano.
In this way we obtain the amplitude distribution of the pressure wave field on the Stromboli topography (Fig 4.10 ab). From fig 4.10 shows how the pressure distribution is tightly dependent on the presence of topographic barrier. Infact the elevated morphological height of Pizzo and Vancori limit southward the distribution of the pressure, where the amplitude quickly decreases down to -80 Db.

Stations	ATTENUATION VALUE	
	SW VENT (dB)	NE VENT (dB)
RIF	- 49.1878	- 48.8995
SAS	- 61.3125	- 63.8221
STR	- 66.4976	- 60.1368
ROC	- 62.1539	- 53.6099
SCI	- 70.3438	- 64.1620

Table 4.3. Attenuation values for all the stations, to be applied to the actual recordings of the infrasonic network for a correct estimate of the pressure values at the source.

The loss prediction by FDTD method at all stations is show in Table 4.3. These values, calculated from the two maps in Figure 4.10, contain the attenuation caused both by geometrical spreading and path effects.
The map of the pressure distribution (Fig 4.10) allows thus to determine univocally the pressure at the source and indicates which is the vent location for an infrasonic station.

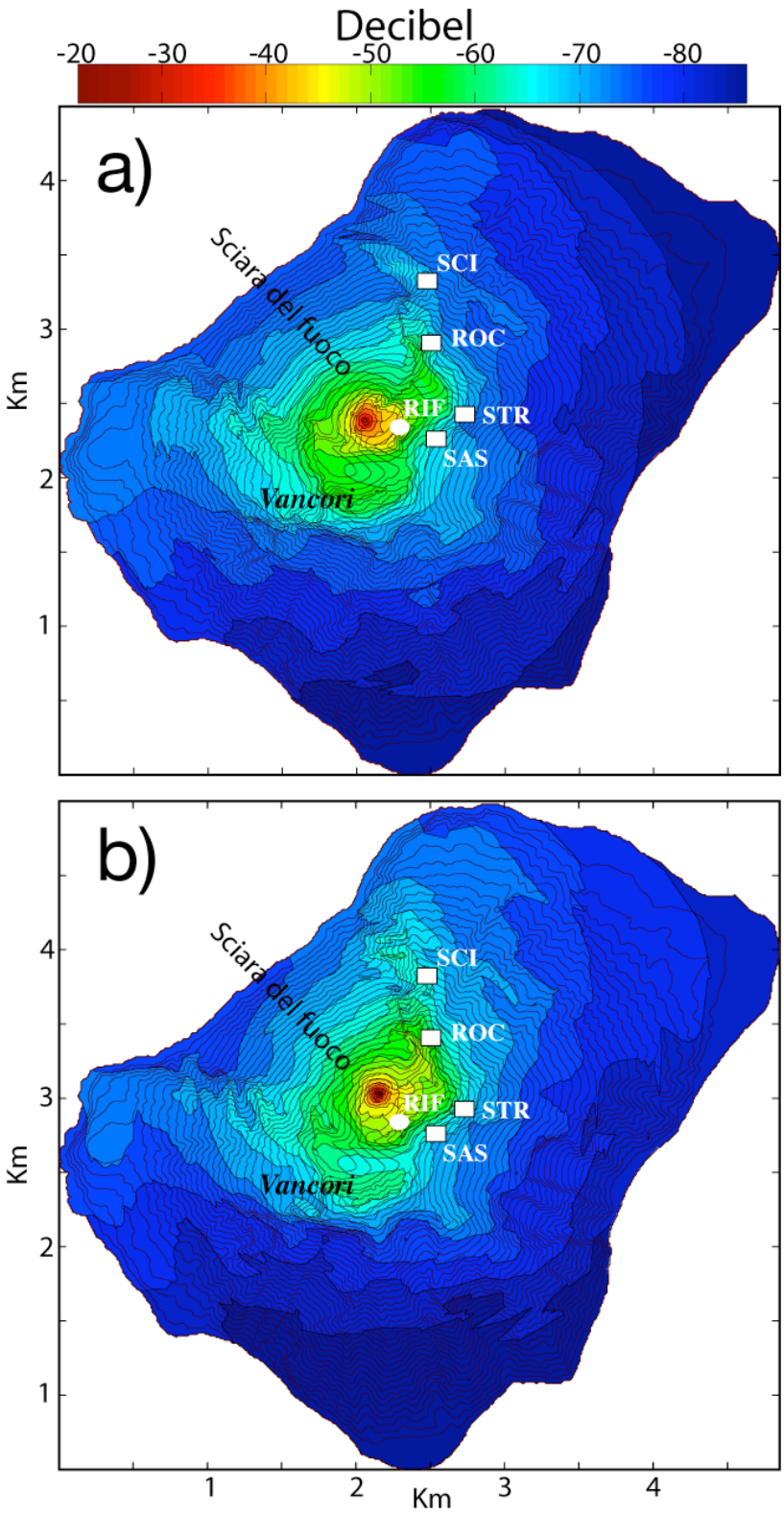

Fig 4.10. Theoretical pressure distribution calculated with FDTD method for source located at SW vent a), and b) for NE vent.

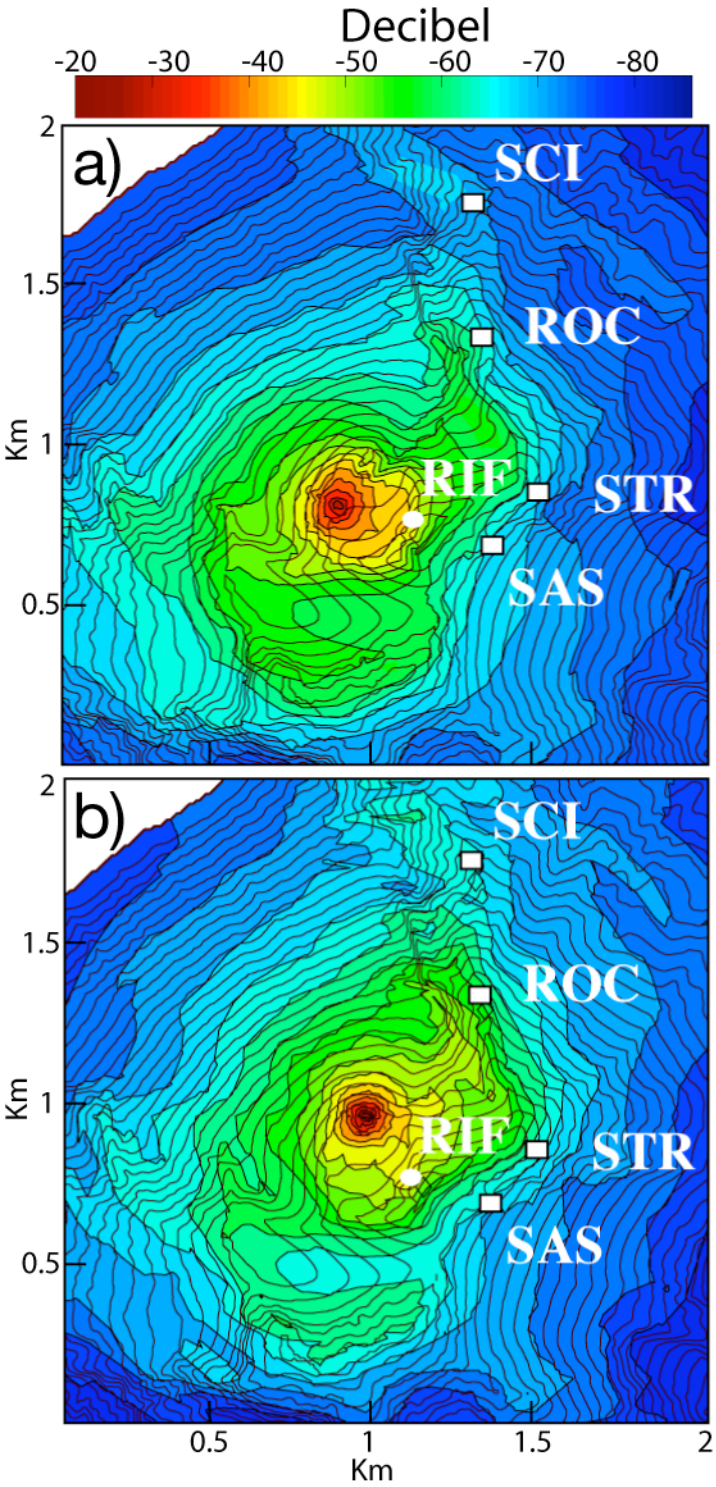

Fig 4.11. Zoom on the stations of the theoretical pressure distribution of the Figure 4.10 for source located at SW vent a), and b) for NE vent.

Discussion

The experimental measurements of acoustic wave generated by explosions at SW (3.1.1) and NE (3.1.2) craters are compared with the result of the FDTD modelling. Synthetic waveforms at five stations were calculated as in chapter 4 and compared with the stacking of the real waveforms as shown in Figures 5.1 and 5.2.
The particularly good fit provides the strong evidence on the ability the finite - difference method, has to generate and to reproduce the pressure wave field recorded in real situations.

The comparison between the observed and calculated waveforms, for both sources (Fig 5.1 and Fig. 5.2), underlines how the great attenuation registered at SAS and STR stations, far from the predicted geometrical spreading decay, is induced by the topographical barrier of Pizzo. This is evident in the snapshots at the SAS station, for both the source at the NE and SW vents, and in the movie at 1.03 seconds and 1.20 seconds (Appendix Fig B.3, Fig B.4). The propagation of the wavefronts in the snapshots of the SAS station show how the first arrival clearly follows the path of a diffracted wave. The same behavior is observed in the snapshots of the acoustic wave propagation for STR station (Appendix Fig B.5, Fig B.6), where the amplitude of the wave – field decreases progressively when the wave – front propagates along the topography towards the station.

The pressure peak calculated at ROC station for both sources is in good agreement with these recorded ones (Fig 5.1 and Fig 5.2), showing an attenuation of -6 dB for the acoustic wave generated at the SW vent, while amplitude of the pressure wave decays according to the geometrical spreading in the case of a source located in the NE vent. However, the FDTD snapshots of the ROC station (Appendix Fig B.7), show how the wave - front in time interval of 0.75 until 1.46 seconds is also diffracted by an edge of the crater terrace. Morphology of the carter terrace and location of the source and of station may produce diffraction due to topographic bumpy along the wave ray path *(Don, 1991)*. The ROC station has perfect in line – of

– sight with the source in the NE vent (Appendix Fig B.8), and thus the first arrival is a direct wave and no diffractions are observed.

At station SCI, acoustic pressure shows an attenuation of -9.9 dB and -4.2 dB for the SW and NE sources, respectively, much higher than a decay with the geometrical spreading (Fig 5.1 and Fig 5.2). The ray path between the two sources and SCI is blocked by the Bastimento ridge (Appendix Fig B.9 and Fig B.10), which obstacle reduces the amplitude of the wave field. In the case of a source generated in the SW crater this effect is increased by the diffraction produced by the edge of crater the terrace (Snapshots at time 0.75 sec and 1.88 sec Fig B.9).

In all cases, the agreement between observed and calculated waveforms is very good, in particular for the peaks of the positive amplitudes and positive pulse duration, although minor differences may be seen. The actual recordings show a negative peak and a second arrival peak in their waveforms that are respectively smaller and larger in amplitude, than in the calculated waveforms. These differences may be due to lateral diffraction of the topography which are not considered in the two – dimensional solution as to the source function used to model the source dynamic. The good agreement between observed and numerical amplitude decay has allowed to obtain the attenuation values at the stations in decibel (Table 4.1).
This attenuation has been applied to the measured peak amplitude (Fig 5.3 and 5.4) improving the estimation of the overpressure at the source. The standard deviation of the pressure amplitude for each explosion at all station drops from about 0.6 to about 0.15. Which, implies that, at each station, it is possible to calculate the overpressure at source with a maximum margin of error of ± 7 %.

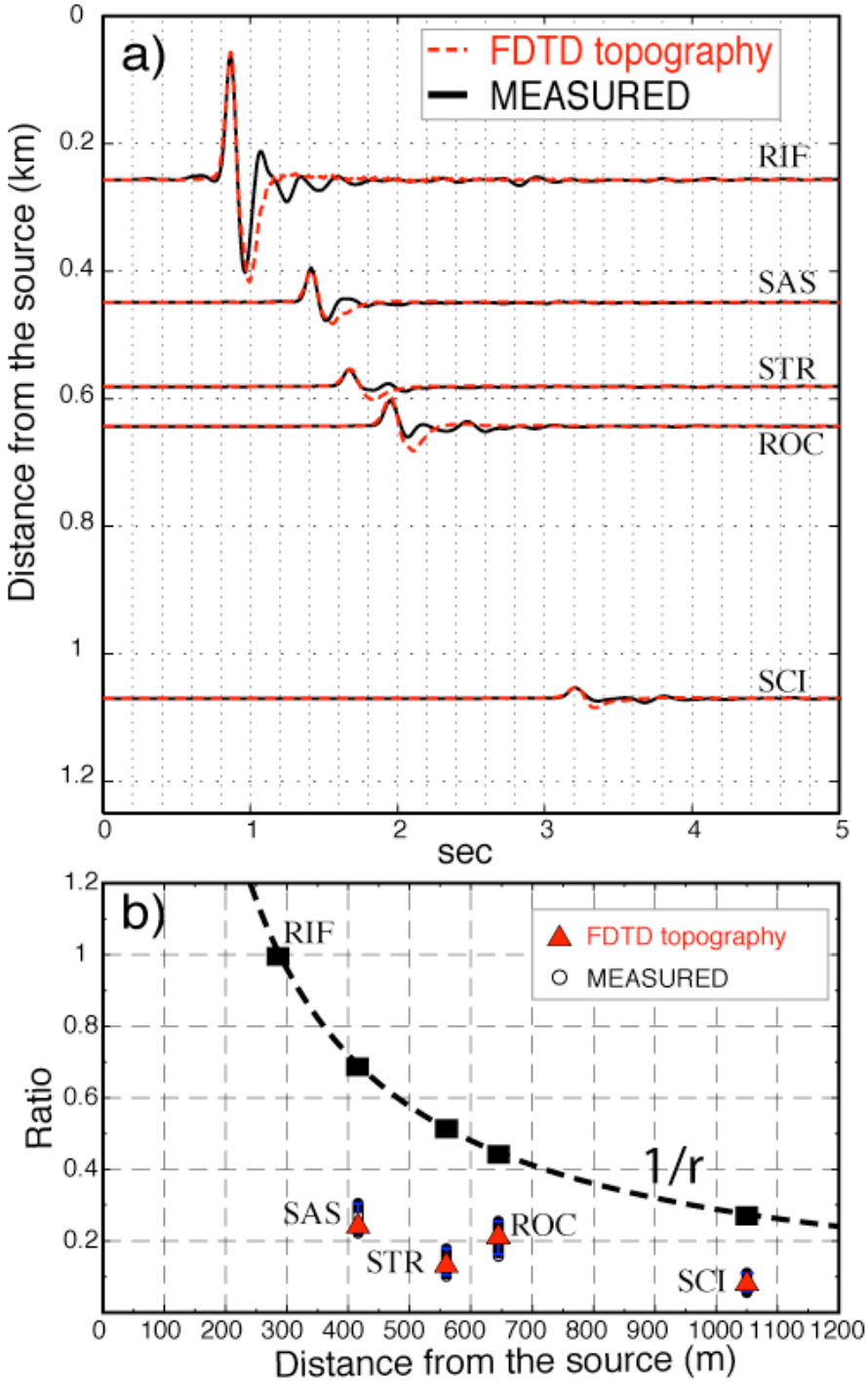

Fig 5.1. Comparison between waveforms. a) The values calculated by means of the FDTD method are represent with the red dashed line and the stacking of waveforms recorded during the first acquisition campaign relative to the source located at SW vent are on the black continuous line. b) Ratio of peak amplitudes between the stations and the reference station (RIF) is calculated from the recordings of 135 waveforms (black circles) and the waveforms calculated with FDTD method (red triangle).

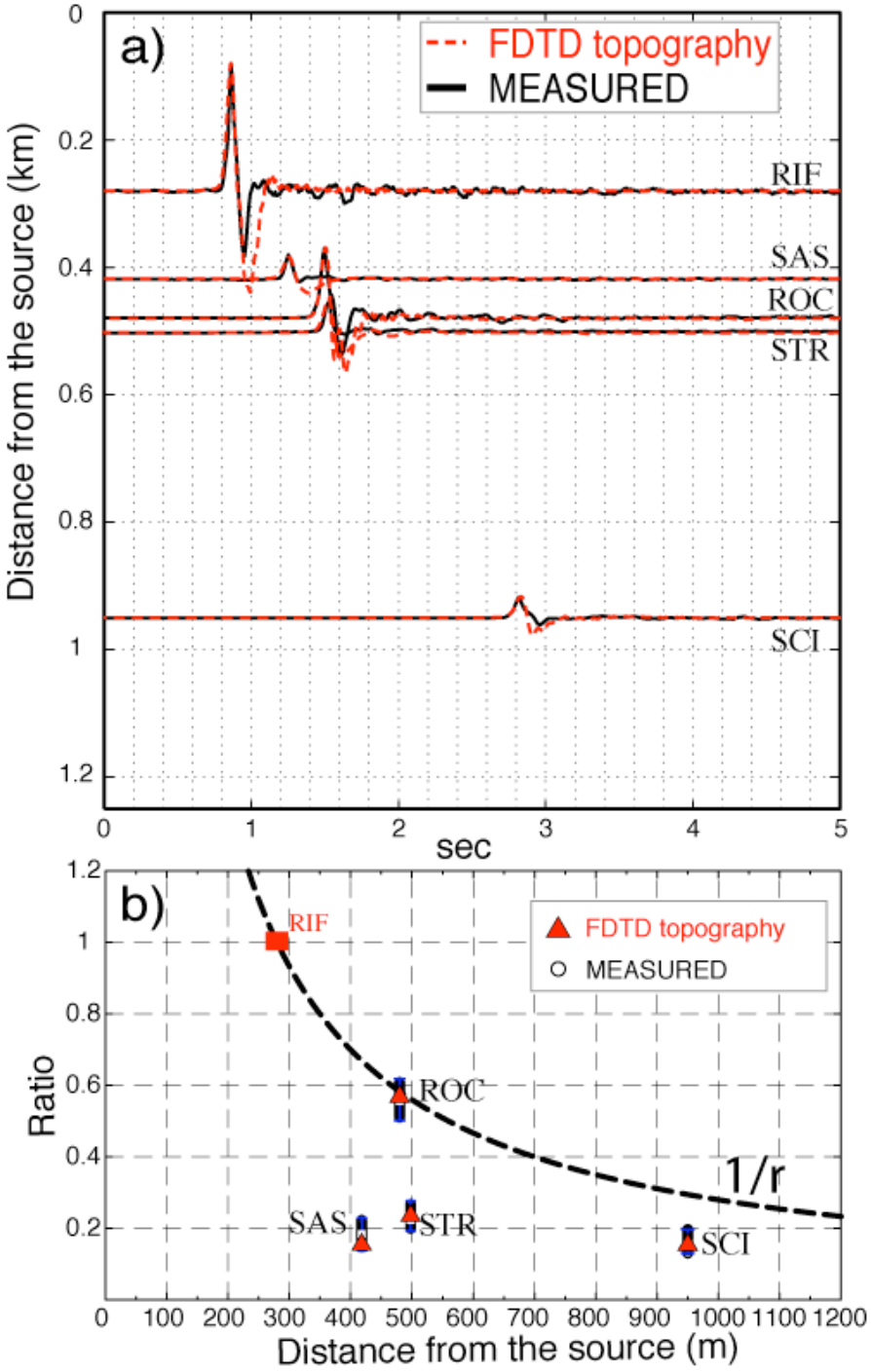

Fig 5.2. a) The waveforms calculated with the FDTD (dashed red line) are compared with the staking of waveforms recorded during the second acquisition campaign (continuous black line) using the source located at NE vent. b) The curve resulting from ratio of peak amplitude decays relative to the Network stations and reference station (RIF), from 39 recorded waveforms (black circles), against the decays of the corresponding waveforms calculated with the FDTD method (red triangles).

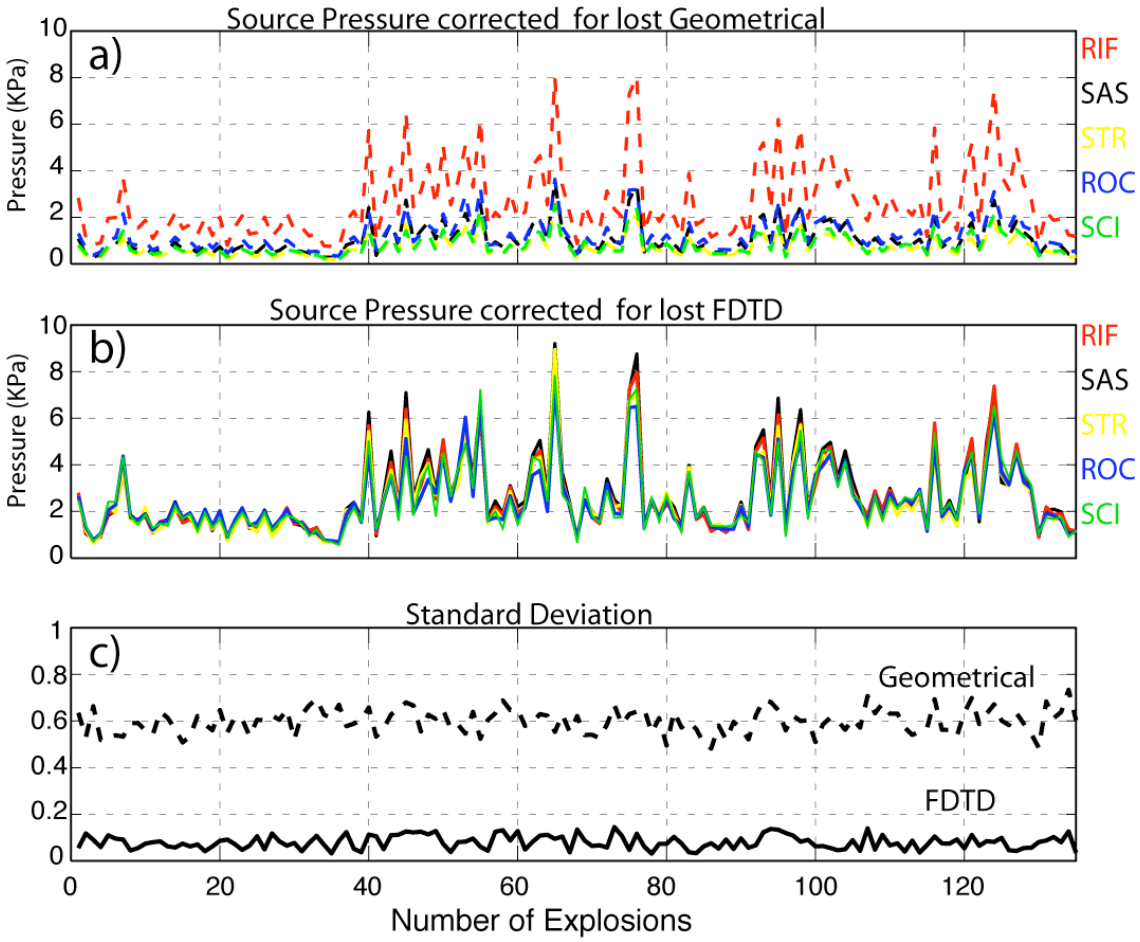

Figure 5.3. a) The resulting pressure at the source, as calculated using the decay for the geometrical spreading at all stations recorded during the first acquisition campaign and with source located at the SW vent. b) The new pressure at sources calculated after the loss – prediction from FDTD method. c) Comparison between normalized standard deviations calculated for each of the 135 explosions at five stations corrected for geometrical spreading (Dashed line) and for loss – prediction from FDTD (continuous line) where a decrease from 0.6 to 0.15 occurs .

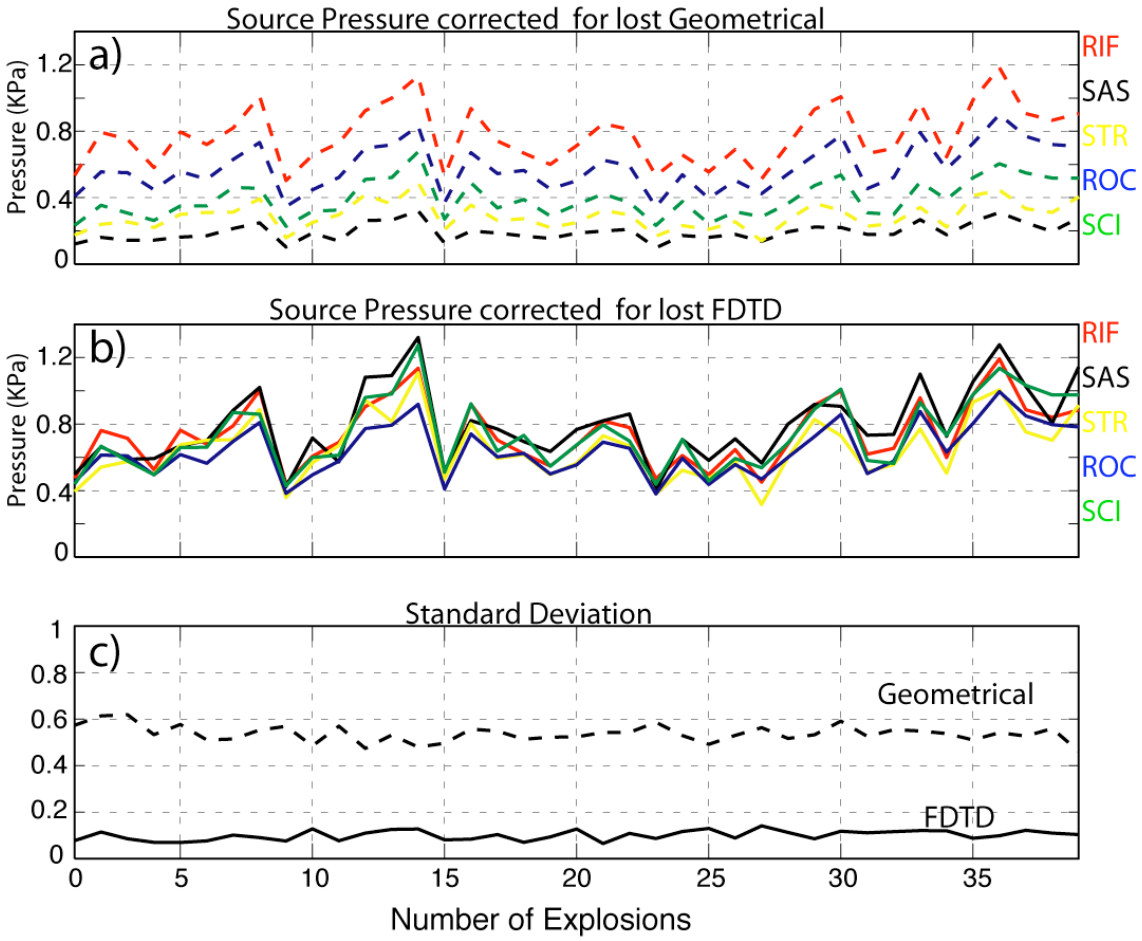

Figure 5.4. a) Pressure at the source calculated as a function of geometrical spreading for all stations recording during the second acquisition campaign and for source located at NE vent. b) Pressure at the same source calculated using the loss – prediction derived from the FDTD method. c) Comparison between normalized standard deviations calculated for each of the 39 explosions recorded at the five stations and corrected for the assumption of a geometrical spreading rate (The upper line dashed) and for applying the FDTD loss – prediction (The lower continuous line) shows a the decrease from 0.6 to 0.15 .

Conclusions

In last decade, acoustic measurements have been performed on a number of active explosive volcanoes. The initial group of studies was ascribing the sound radiated during eruptions to the resonance of the conduit propagating both in the magma and in atmosphere *(Buckingham and Garcès 1996, Garcès and McNutt 1997, Marchetti et al. 2004)*.

While a second class of studies relates the source of sound to eruption dynamics, such as the sudden uncorking of the volcano *(Johnson et al. 1998, Vergnolle and Caplan Auerbach 2004)*.

Woulff and McGecthin *(1976)* were among the first to investigate the acoustic signal associated to the gas release. In their paper, Woulff and McGecthin, described a relation between acoustic pressure and velocity of the gases ejected from volcanic vent. The velocity of ejecta at the vent is one of the major parameters to study dynamics of the volcanic plumes. Ballistic studies *(Chouet et al. 1974, McGetchin et al. 1974, Ripepe et al. 1993)* have been used in the past time to constrain velocities, radar measurements have been a recent major improvement *(Dubosland et al. 1999, Hort at al. 2003)*. This technique may, however, be difficult to implement as equipment is both heavy and high energy consuming.

Pressure sensors have also been used to detected eruptions at distances of several kilometres and to estimate the pressure at vent *(Morrisey and Chouet 1997a,b, Ripepe et al. 2010)*.

For large eruptions they indicate that the excess pressure range over two orders of magnitude from ~0.4 MPa during strombolian eruptions at Stromboli to the largest eruptions, ~ 7.5 MPa at Mount St. Helens (USA) and ≥ 5 MPa at Pinatubo (Philippines). Open conduit volcanoes such as Stomboli, are an efficient source of low frequencies (1 – 5 Hz) acoustic waves. Craters, at Stromboli, are located on a flat terrace bordered by a hemi – circolar edge of about 150 meter higher (Fig 1.3) acting as barrier, and less than 200 meters distant from vents. Wavelengths in the order of 80 – 90 meter are closely comparable in dimension with the actual geometry of the crater geometry. Thus, diffraction and reflection effects caused by the topography

may be possible, and could modify the pressure wave field in terms of both amplitude distribution and frequency content.
In order to evaluate these effects, a comparison between experimental data and synthetic waveforms calculated by finite – difference time domain (FDTD) has been performed. Infrasonic data were collected during 2 different surveys, separating the wavefield produced by the two different vents, and, with the source to receiver distances ranging from 0.25 to 1.1.
The numerical modelling has shown great coherence with the field measurements, which confirms that the presence of a topographical barrier along the path between source and station produces diffracted waves. The diffraction acts as a strong low – pass filter, greatly reducing frequencies above 3.8 Hz, whose peak amplitude decays by to -11 dB.
The finite difference time domain method was used to calculate theoretical waveforms using a simplified two – dimensional representation of the topography.
This method is fast and produce a good agreement with measured arrival times, peak amplitudes and waveforms characteristics, for which no analytical solution exists. The comparison shows that the limitation to a two – dimensional geometry speeds up the calculations significantly, while introducing only small errors in the accuracy. This simulation method contains useful prospects for investigating acoustic wave propagation in other volcanoes, such as Etna, Eyafiallajoekull (Iceland) and Montserrat (West Indies), where infrasonic arrays have been installed by the Dipartimento di Scienze della Terra.
We have then demonstrate that scattering and diffraction effects are caused by topography of the crater rim, and that come modify the pressure wave field in their amplitude and frequency content.
Thus, future works dealing at defining source parameters, such as on how the excess pressure at the source, or to determine mass flux and/or gas velocity, from pressure waveforms, must take into account the path effects for their correct assessment.

APPENDICES

A. Measurements

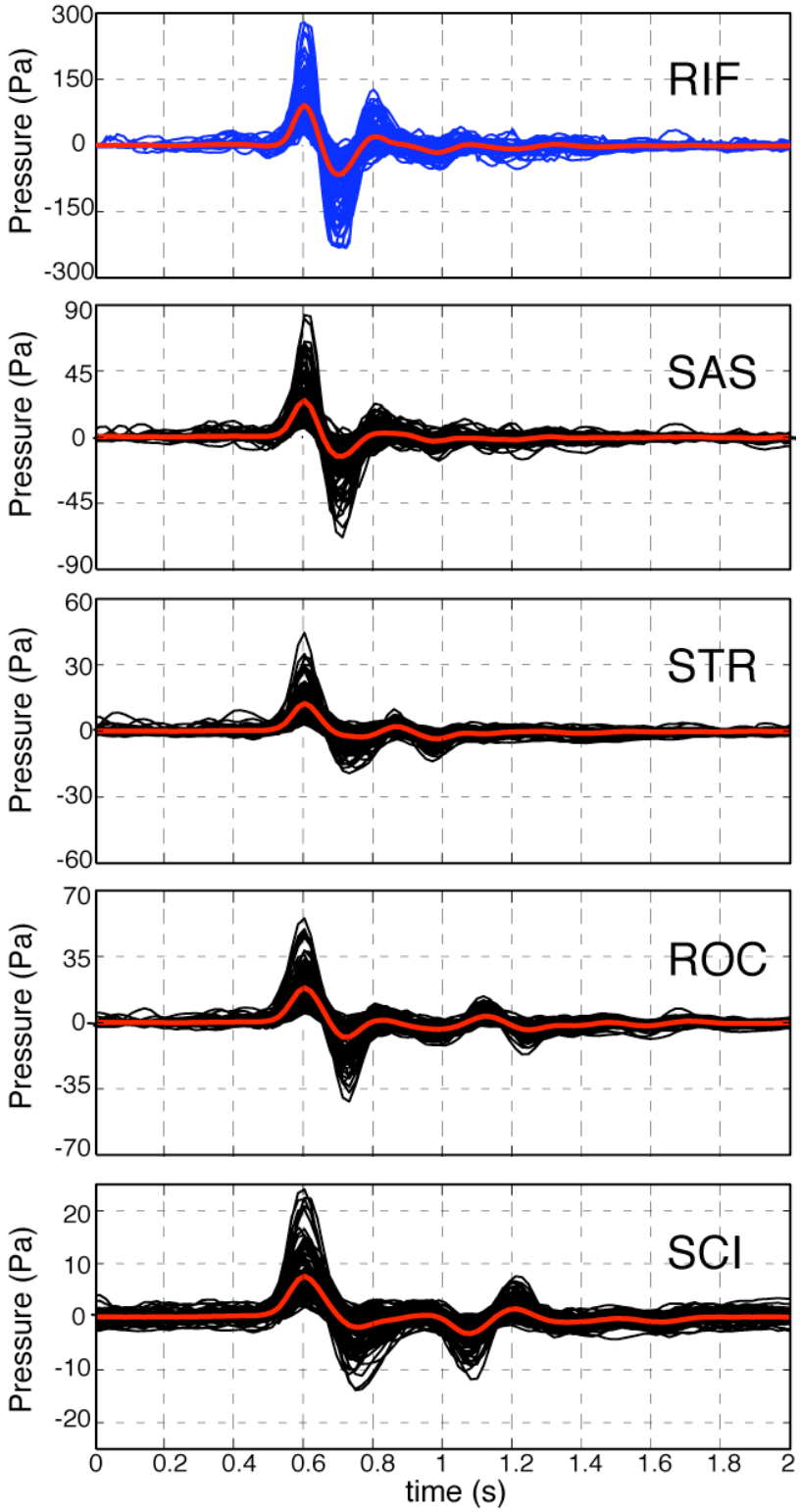

Fig. A.1. The 135 waveforms recorded at 5 stations during the first acquisition campaign carried out at Stromboli from 28/07/2009 to 7/08/2009 with source located at SW crater, and staking waveform (in red line) at each station.

TIME	Azimuth °	MAX Pressure (Pascal)				
		RIF	SAS	STR	ROC	SCI
28Jul2009 23:56:59	261.4	98	25.1	12.7	19.7	7.6
29Jul2009 00:29:27	261.4	39	9.5	6	9.9	4.3
29Jul2009 00:31:57	261.4	28.7	7.1	3.2	5.7	2.2
29Jul2009 00:40:42	261.4	31.5	8.9	4.9	7.8	3.2
29Jul2009 01:10:45	261.4	68	16.6	11.2	15.3	7.4
29Jul2009 01:28:48	261.4	69.1	18.2	9.7	17	7.4
29Jul2009 02:07:05	261.4	127.5	33.2	18.8	32.5	13.4
29Jul2009 02:37:45	261.4	61.2	16.5	8.1	12.9	5.5
29Jul2009 02:38:38	261.4	53.2	14.2	7.3	12.2	4.4
29Jul2009 03:07:17	261.4	64.7	16.3	10.8	14.1	5.7
29Jul2009 03:24:55	261.4	37.7	9.7	5.6	8.9	4
29Jul2009 03:51:12	261.4	55.1	14	6.4	11.5	4.5
29Jul2009 03:51:42	261.4	55.4	14.8	7.5	11.8	4.3
29Jul2009 03:59:23	261.4	75.7	21.7	10.4	17.4	6.8
29Jul2009 04:16:24	261.4	52.6	14.6	9.2	13	5.2
29Jul2009 04:52:33	261.4	58.4	15.6	8.9	14.5	5.8
29Jul2009 05:03:39	261.4	44.2	11.5	5.5	9.7	3.6
29Jul2009 05:16:06	261.4	68	17.6	9.3	15.6	6
29Jul2009 05:24:48	261.4	42.3	10.6	6.3	10.3	4
29Jul2009 05:35:33	261.4	69.4	17.2	8.5	15.1	5.2
29Jul2009 06:37:37	261.4	27.7	7.7	3.7	6.7	2.8
29Jul2009 07:01:39	261.4	54.7	14.4	6.7	12	4.5
29Jul2009 07:10:29	261.4	71.6	17.7	9.6	16	6
29Jul2009 07:21:14	261.4	44.2	11.7	6.7	10.5	4.6
29Jul2009 07:25:26	261.4	46.8	11.9	5.6	11.4	4.2
29Jul2009 07:52:22	261.4	69.7	18.5	9	15	6
29Jul2009 08:23:46	261.4	41.6	10.8	4.6	9.5	3.6
29Jul2009 08:47:45	261.4	53.2	13.5	6.5	12.1	4.8
29Jul2009 08:51:10	259.3	75.6	18.6	9.5	15.5	5.7
29Jul2009 09:05:37	261.4	50.7	13.3	8.5	11.6	5.2
29Jul2009 10:07:56	261.4	54.3	12.6	7.3	11.4	4.6
29Jul2009 10:37:42	259.3	41.3	9.8	5.4	8	2.9
01Aug2009 07:03:46	261.4	45.9	10.4	4.9	8.1	3.8
01Aug2009 12:52:09	261.4	26.7	6.6	3.2	5.8	2.3
03Aug2009 10:16:42	261.8	26.2	6.7	3.6	5.5	2.1
03Aug2009 10:22:27	261.8	24.5	5.8	3	5	1.7

05Aug2009 04:23:34	264.2	64.4	19	10.3	14	4.7
05Aug2009 04:28:18	264.2	78.4	21.5	10.6	17.5	6.7
05Aug2009 04:59:04	261.4	57.4	15.5	8	11.4	4.8
05Aug2009 05:01:30	261.4	198.5	56.3	27.1	33.7	13.5
05Aug2009 05:24:35	264.2	36.1	8.6	6	9	3.7
05Aug2009 05:46:40	261.4	84.8	24.3	12.6	18	7.3
05Aug2009 06:41:26	261.4	143.3	41.3	18.8	26.2	11.1
05Aug2009 06:54:43	264.2	74.2	19	10.5	14.4	4.9
05Aug2009 07:33:07	261.4	223.3	63.9	29.6	38.1	13.5
05Aug2009 07:53:25	264.2	84.9	23.6	11.5	14.4	5.6
05Aug2009 07:54:48	264.2	108.5	33.1	17.5	19.5	10.1
05Aug2009 08:25:42	261.4	148.2	41.9	20.2	25.1	12.2
05Aug2009 08:26:06	264.2	88.5	24.9	13.6	20.7	5.5
05Aug2009 09:03:25	264.2	176.1	45.6	22.1	32.5	13.9
05Aug2009 09:22:18	261.4	88.1	24	13.3	18.1	8.1
05Aug2009 10:09:24	264.2	124.2	33.2	15.6	28.3	11.8
05Aug2009 10:23:13	264.2	177.1	50.4	27.5	45	15.1
05Aug2009 11:05:46	264.2	114.2	30.8	15.3	19.7	9.2
05Aug2009 11:24:32	264.2	213.7	59.8	32.8	49.5	22.3
05Aug2009 11:38:08	264.2	57.3	15.2	7.5	12	4.9
05Aug2009 12:11:43	261.8	76.6	22	10.2	12.9	6.1
05Aug2009 12:14:03	264.2	65.4	17.1	8.3	12.3	3.9
05Aug2009 12:47:23	264.2	106.3	28	14.2	19.9	7.7
05Aug2009 13:02:18	261.4	67.5	19.8	8.7	12.8	4.4
05Aug2009 15:06:22	264.2	77.4	21.9	10.8	16.1	6.8
05Aug2009 16:01:05	261.4	146	39.6	20.8	26.4	13.4
05Aug2009 16:09:30	261.4	160.9	45.4	21.7	28.1	12.8
05Aug2009 16:38:47	261.4	88.1	24.8	12.1	14.9	7.5
05Aug2009 17:04:42	261.4	298	82.9	44.7	55	24.2
05Aug2009 17:22:05	264.2	117.6	32.9	16	23.5	8.4
05Aug2009 18:12:12	264.2	75.1	21.2	11.3	16.3	7
05Aug2009 18:38:59	261.4	30.3	7.6	4.8	6.6	2
05Aug2009 20:09:32	264.2	87.1	23.2	13	18.6	9.4
05Aug2009 20:29:12	264.2	61	17.9	9.8	12.9	5.6
05Aug2009 21:08:10	264.2	51.7	14.8	8.7	12.4	4.7
05Aug2009 21:17:27	264.2	108.5	30.6	15.3	23.7	8.9
05Aug2009 22:54:37	261.4	81.6	22.4	10.9	14.3	5.3
05Aug2009 23:05:55	261.4	70.2	19.5	11.5	13.9	5.4

05Aug2009 23:25:02	261.4	253.3	64.4	33.7	48	20.9
06Aug2009 00:23:09	261.4	278.7	78.8	35.1	48.4	22.3
06Aug2009 01:02:17	264.2	48.5	12	6.2	9.5	3.7
06Aug2009 01:56:43	264.2	82.6	22.7	12.3	18.7	7.9
06Aug2009 02:10:28	264.2	63.4	16.2	9.5	12.9	4.8
06Aug2009 03:06:28	261.4	80.6	23.5	14.1	18.9	8.3
06Aug2009 03:39:01	261.4	70.7	19.6	9.2	12.6	5.5
06Aug2009 03:58:08	261.4	42.6	11.6	6.4	10.2	3.4
06Aug2009 04:05:28	264.2	134.7	35.8	19.4	26.9	11.5
06Aug2009 04:52:24	265.2	58	14.9	9	12.7	5.3
06Aug2009 05:43:10	264.2	65.8	18.9	11.1	16.1	6.6
06Aug2009 05:43:50	264.2	40	11.9	6.9	9.9	4.3
06Aug2009 05:58:27	264.2	46.6	11.7	7.3	9.5	4.2
06Aug2009 06:05:09	264.2	39.2	10	6.5	9.2	4.2
06Aug2009 06:12:19	264.2	48.1	12.7	6.8	9.2	4.3
06Aug2009 06:43:38	264.2	73.1	21.6	11.3	16.5	5.7
06Aug2009 07:08:41	264.2	42.8	12.1	6.6	10	4.4
06Aug2009 07:13:57	261.4	160.4	43.2	21.5	30.4	12.9
06Aug2009 07:51:26	265.2	180.2	49.5	22.8	29.3	11.7
06Aug2009 08:04:44	264.2	81.7	22.1	10.2	13.7	5.6
06Aug2009 08:11:16	261.4	215.1	61.8	28.3	38	15.4
06Aug2009 08:23:24	264.2	40.5	11.4	7.2	10.1	2.8
06Aug2009 08:34:39	264.2	141	39.2	20.4	27.4	10
06Aug2009 08:40:35	264.5	201.5	57.3	28.5	37.8	16.9
06Aug2009 09:06:36	264.2	68.4	19.3	9.9	14.1	5.1
06Aug2009 09:13:23	264.2	110.6	32.9	18.5	26.7	10.5
06Aug2009 09:16:31	264.2	154.2	42.3	21.9	29.6	14.2
06Aug2009 09:20:35	265.2	167.2	44.7	21.7	33.1	14.2
06Aug2009 09:36:59	264.2	114.6	30.8	16.2	23.6	9.3
06Aug2009 09:42:04	264.2	142.7	41.4	20.5	31.2	12.8
06Aug2009 10:34:40	261.8	103.2	29.7	14.1	20.4	8.1
06Aug2009 10:52:00	261.4	79.2	21.1	11.3	16.5	7.6
06Aug2009 20:19:41	261.8	64.3	16.4	7	11.8	4.2
06Aug2009 20:52:40	261.4	101	25.7	12.9	20	8.2
06Aug2009 21:02:10	261.4	69.8	18.4	8.1	12.7	5
06Aug2009 21:13:02	261.4	101.8	26.9	12.9	20.6	8
06Aug2009 21:26:09	265.2	77.6	19.8	9.2	16.2	6.5
06Aug2009 21:48:31	264.2	84.9	22.5	11.8	18.8	8

06Aug2009 22:37:19	264.2	72.4	19.4	10.2	17.4	7.7
06Aug2009 23:48:56	261.4	93.8	24.9	14	22	8.8
07Aug2009 00:11:09	261.4	41.2	12.1	5.7	8.6	3.7
07Aug2009 02:01:41	261.4	202.4	46.1	21.9	35.9	16.6
07Aug2009 02:28:55	264.2	60	16.7	8	13.2	6
07Aug2009 03:02:20	261.4	76.2	22.3	10.2	16.6	7.3
07Aug2009 03:33:31	264.2	49.9	14.5	6.8	12.4	5.1
07Aug2009 03:58:10	264.2	131.4	30.3	16.8	27.8	10.9
07Aug2009 04:13:45	261.4	179.4	41.5	18.7	33.2	14
07Aug2009 04:25:37	264.2	59.7	14.1	8.6	12.7	5.8
07Aug2009 04:41:05	264.2	165	45.1	21.3	30.4	13.3
07Aug2009 04:42:49	264.2	258.1	63.6	30.3	47	20.1
07Aug2009 04:47:03	264.2	131.1	29.2	17.9	27.4	13.1
07Aug2009 05:06:55	264.2	110.5	28.1	15.3	23.4	10.6
07Aug2009 05:20:40	261.4	170.9	42.9	22	33.5	14
07Aug2009 05:39:16	261.4	118.6	31.6	15.8	24.2	11.2
07Aug2009 05:44:03	264.2	95.4	25.2	14.1	22.2	9.7
07Aug2009 06:02:35	264.2	31	9	5.5	7.7	3.2
07Aug2009 06:10:44	264.2	76.8	18.3	9.6	14.3	5.3
07Aug2009 06:37:07	261.4	65	18.9	8.1	13.6	5.2
07Aug2009 06:46:19	264.2	66.7	17.8	8.4	12.2	5.4
07Aug2009 22:04:11	264.2	43.1	9.9	4.8	7.3	2.8
07Aug2009 23:20:08	264.2	40.7	9.7	5.8	8.6	3.6

Table A.1. Infrasonic event recorded during the first acquisition campaign from 28/08/2009 to 7/08/2009. Infrasonic back – azimuth inferred from array analysis are specified in column 2. The max pressure of each event and for each station are shown from 3 to 8 column.

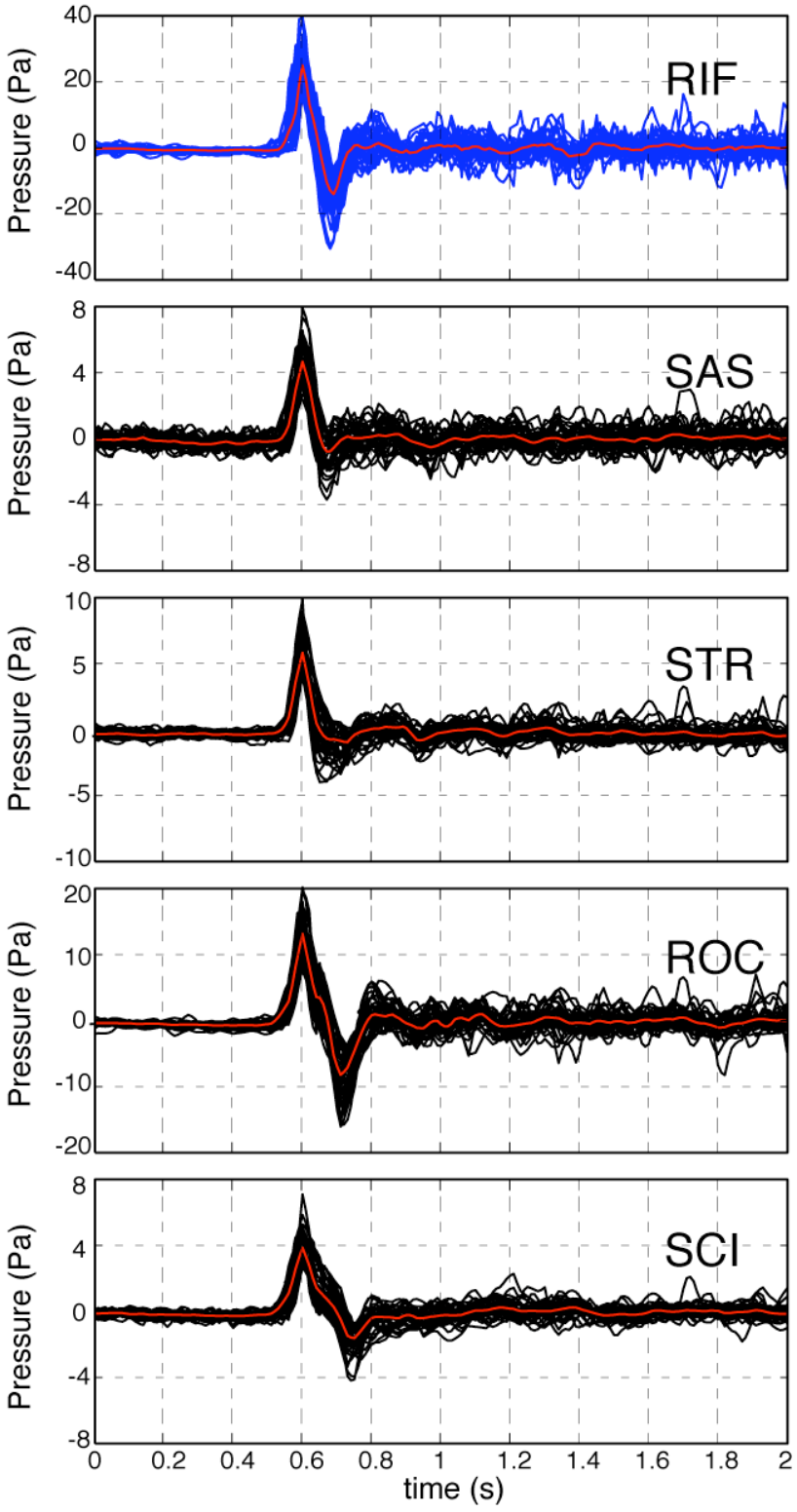

Fig. A.2. The 39 waveforms recorded at 5 stations during the second acquisition campaign carried out at Stromboli from 30/09/2009 to 8/10/2009 with source located at NE crater, and staking waveform (in red line) at each station.

TIME	Azimuth °	MAX Pressure (Pascal)				
		RIF	SAS	STR	ROC	SCI
30Sep2009 06:13:04	279.62	16.5	2.9	4.1	9.5	2.5
30Sep2009 07:40:05	279.62	26.4	3.9	4.8	14.6	3.7
30Sep2009 09:37:29	279.62	24.8	3.4	5.1	13.6	3.2
30Sep2009 11:28:14	279.62	18.3	3.4	4.4	10.4	2.8
30Sep2009 13:04:27	279.62	26.5	3.9	6	14.5	3.7
30Sep2009 13:11:32	279.62	23.6	4.1	6.2	12.9	3.7
30Sep2009 15:44:02	279.62	27.4	5.1	6.3	15.1	4.9
30Sep2009 22:31:21	279.62	34.8	5.9	7.9	19.2	4.8
30Sep2009 22:56:18	279.62	15.3	2.5	3.2	8.7	2.4
30Sep2009 23:03:07	279.62	21.1	4.5	5	12.3	3.4
30Sep2009 23:13:40	279.62	24	4.3	6	13.7	3.4
30Sep2009 23:36:04	279.62	31.4	6.3	8.4	17.2	5.4
01Oct2009 08:05:36	279.62	34.4	6.3	7.2	18.9	5.5
01Oct2009 08:07:25	279.62	39.4	7.7	9.9	22.3	7.1
01Oct2009 13:49:48	279.62	16.3	3	4.2	9.1	2.9
01Oct2009 14:26:45	279.62	32	4.8	7.1	18.6	5.2
01Oct2009 15:08:10	279.62	24.4	4.5	5.3	14.4	3.6
03Oct2009 15:32:26	279.62	21.6	4	5.5	12.8	4.1
05Oct2009 13:02:01	279.62	19	3.7	4.4	11.4	3.1
05Oct2009 15:39:17	279.62	23.3	4.5	5	13.5	3.8
06Oct2009 04:41:04	279.62	28.5	4.8	6.5	15.8	4.4
06Oct2009 20:44:46	279.62	27.1	5	5.9	14.9	3.9
06Oct2009 21:34:20	281.28	16.4	2.3	3.4	9.2	2.5
07Oct2009 08:02:42	281.28	21.2	4.1	4.6	12.2	4
07Oct2009 14:50:47	279.62	17.2	3.8	4.2	10.7	2.6
07Oct2009 17:35:42	279.62	22.5	4.3	5.1	13.2	3.3
08Oct2009 00:40:28	279.62	15.7	3.3	2.8	8.9	3
08Oct2009 00:48:09	279.62	23.6	4.7	5.3	13.7	3.8
08Oct2009 06:14:30	279.62	31.8	5.3	7.4	18.7	5
08Oct2009 06:35:45	279.62	34.7	5.3	6.5	20.2	5.6
08Oct2009 09:04:43	279.62	21.5	4.3	4.6	12.5	3.2
08Oct2009 09:50:18	279.62	22.7	4.3	4.9	13.9	3.2
08Oct2009 10:04:21	281.28	33.2	6.4	6.9	19.1	5.2
08Oct2009 10:09:43	281.28	20.8	4.2	4.5	11.9	4.1
08Oct2009 11:14:19	279.62	33.9	6.1	8.3	19.1	5.5

08Oct2009 11:46:11	281.28	41.4	7.4	8.9	23.7	6.4
08Oct2009 11:54:12	281.28	30.8	6	6.7	17.2	5.8
08Oct2009 12:53:45	279.62	29.2	4.7	6.2	16.8	5.5
08Oct2009 15:23:41	279.62	30.8	6.6	8.1	17.9	5.5

Table A.2. Infrasonic event recorded during the second acquisition campaign from 30/09/2009 to 8/10/2009. Infrasonic back – azimuth inferred from array analysis are specified in column 2. The max pressure of each event and for each station are shown from 3 to 8 column.

APPENDICES

B. Simulations

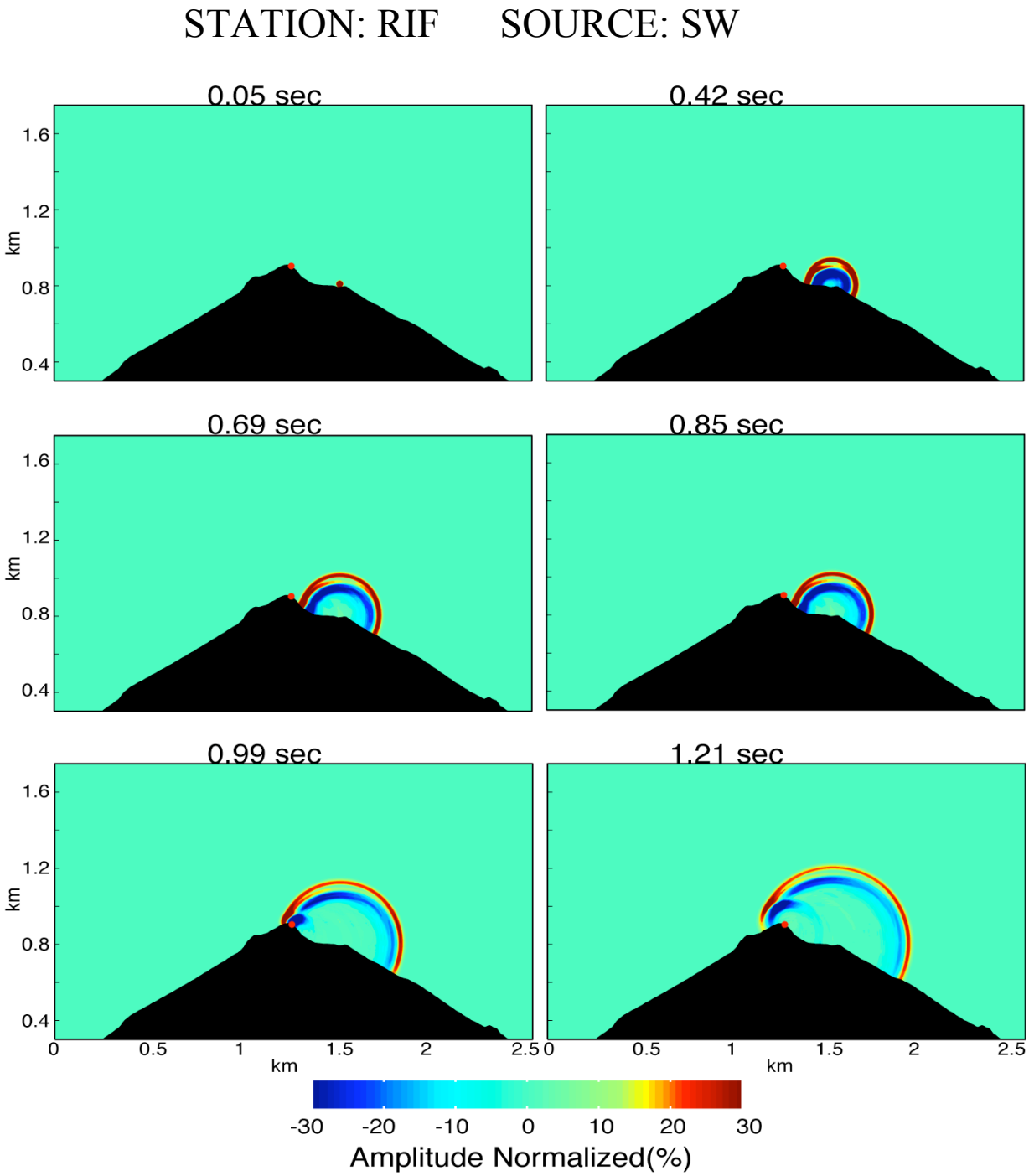

Fig B.1. Snapshots of acoustic wave produced by source located at the SW vent interacting with topographic section of the RIF station.

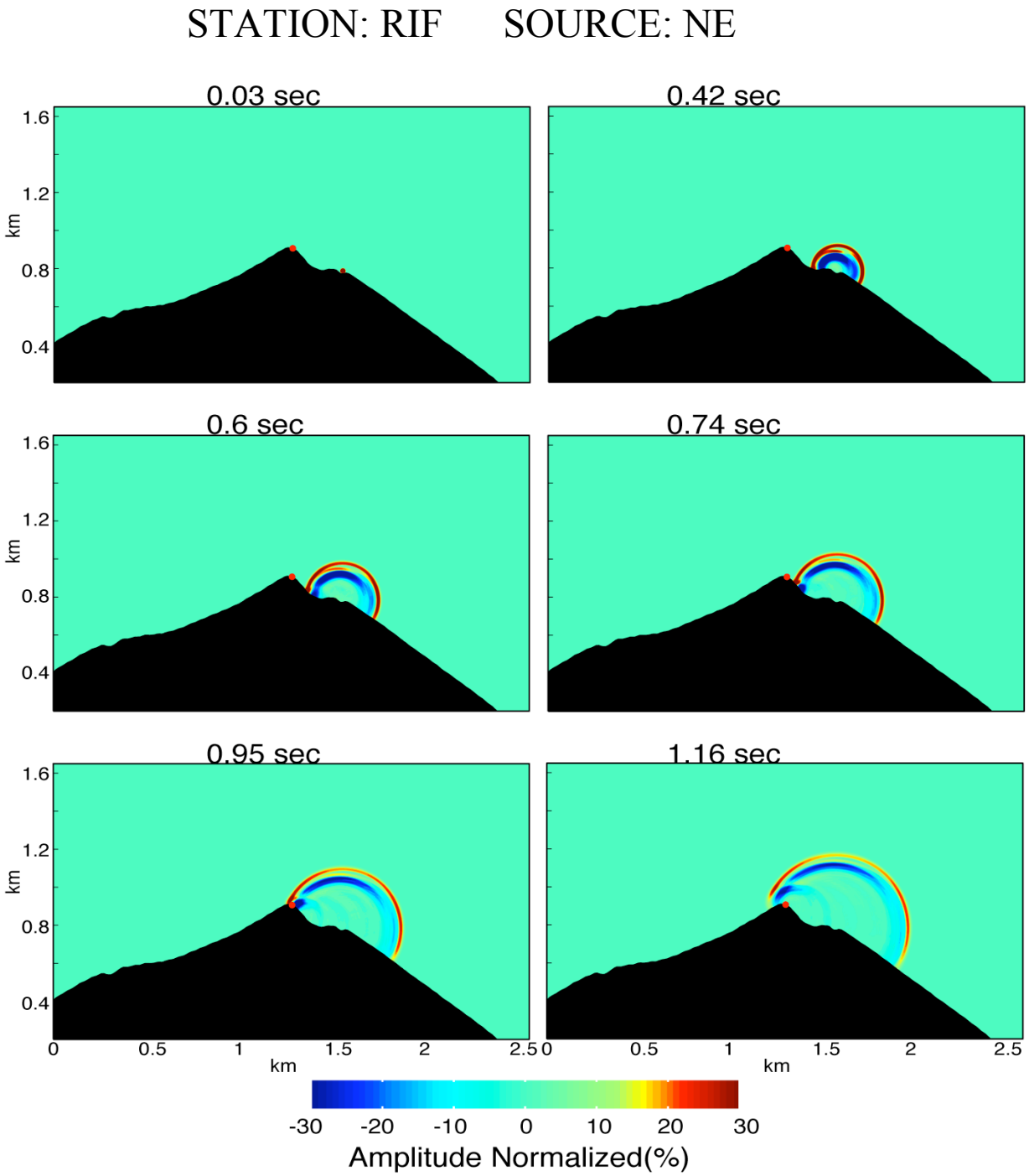

Fig B.2. Snapshots of acoustic wave produced by source located at the NE vent interacting with topographic section of the RIF station.

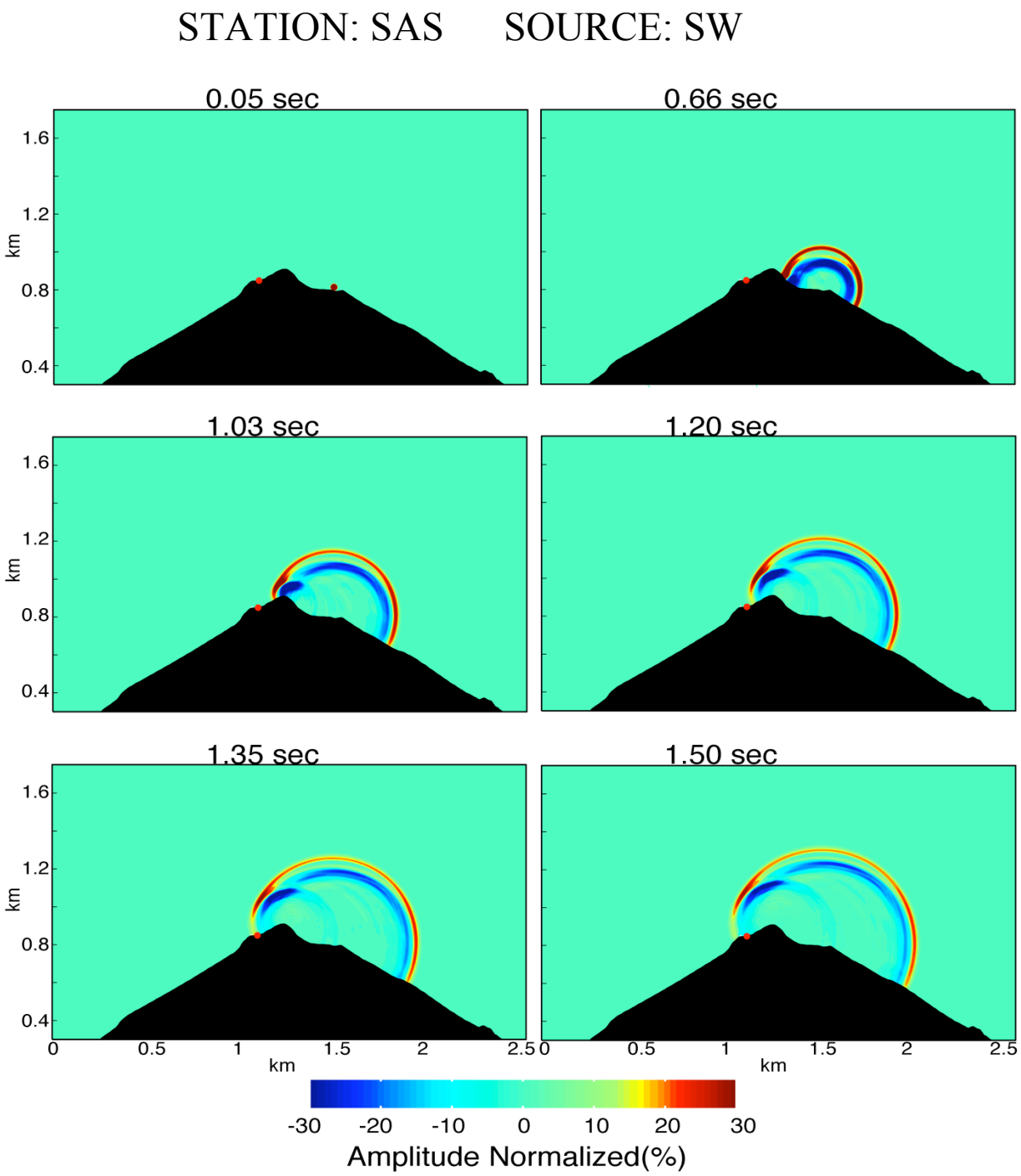

Fig B.3. Snapshots of acoustic wave produced by source located at the SW vent interacting with topographic section of the SAS station.

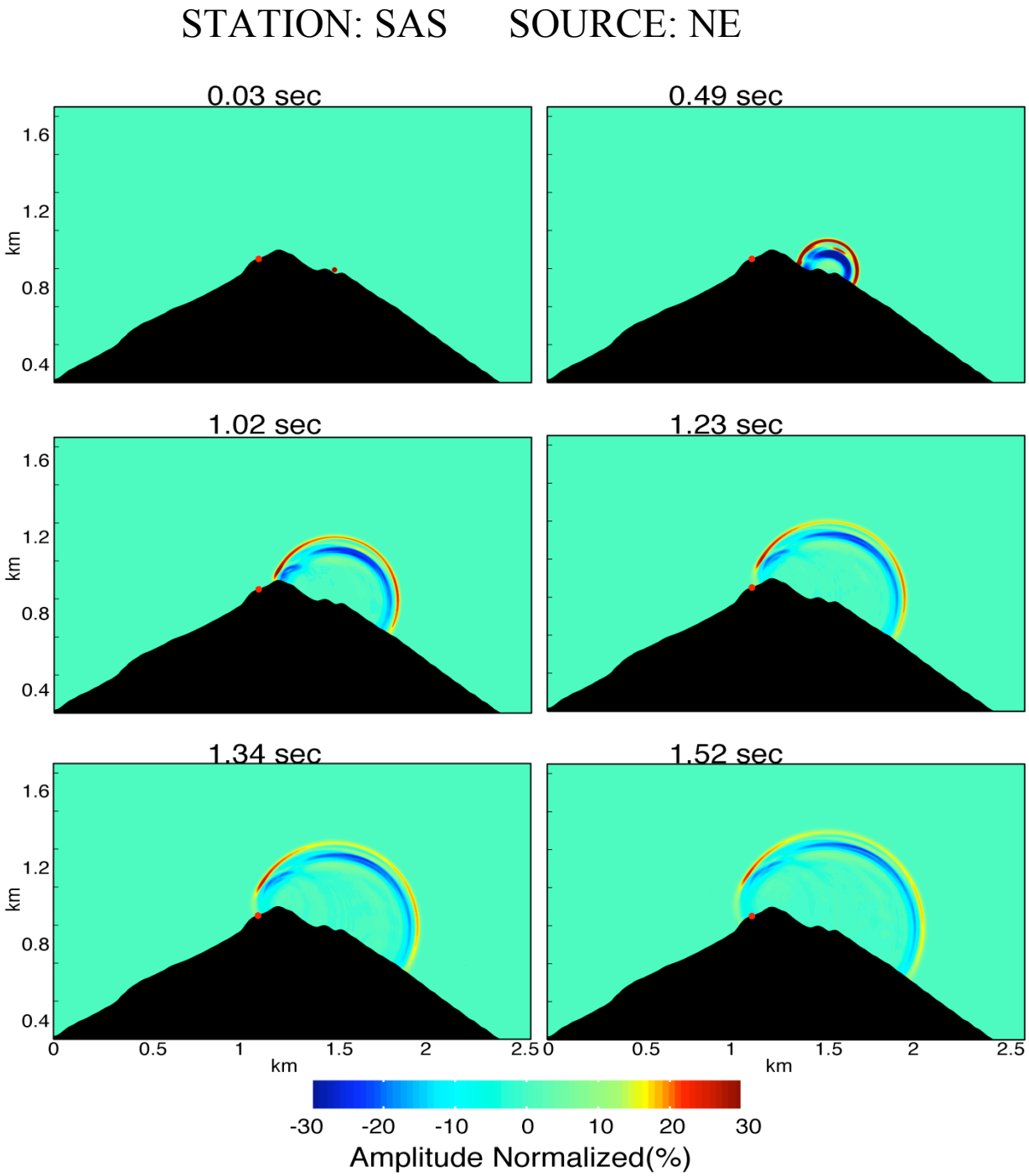

Fig B.4. Snapshots of acoustic wave produced by source located at the NE interacting with topographic section of the SAS station.

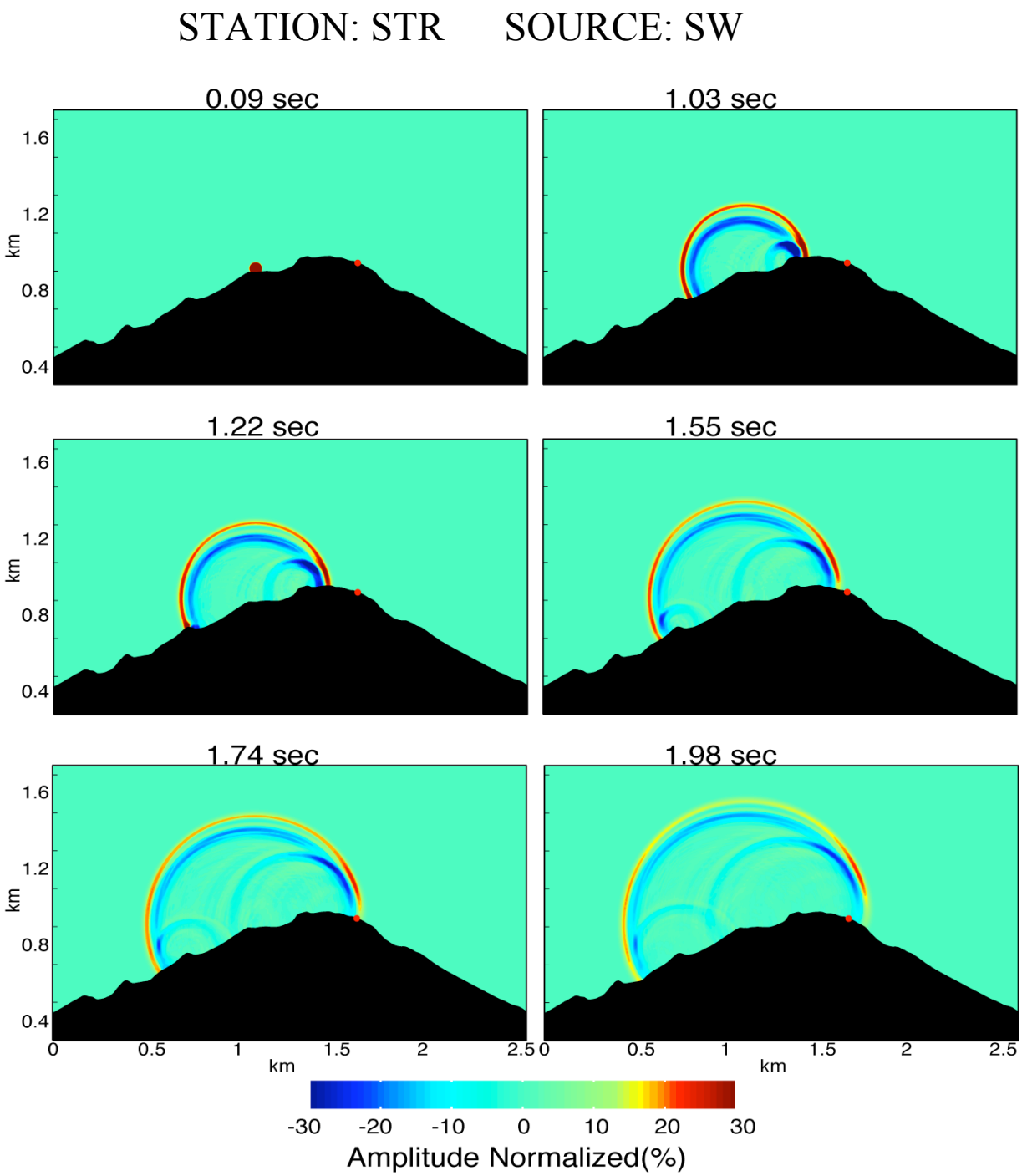

Fig B.5. Snapshots of acoustic wave produced by source located at the SW interacting with topographic section of the STR station.

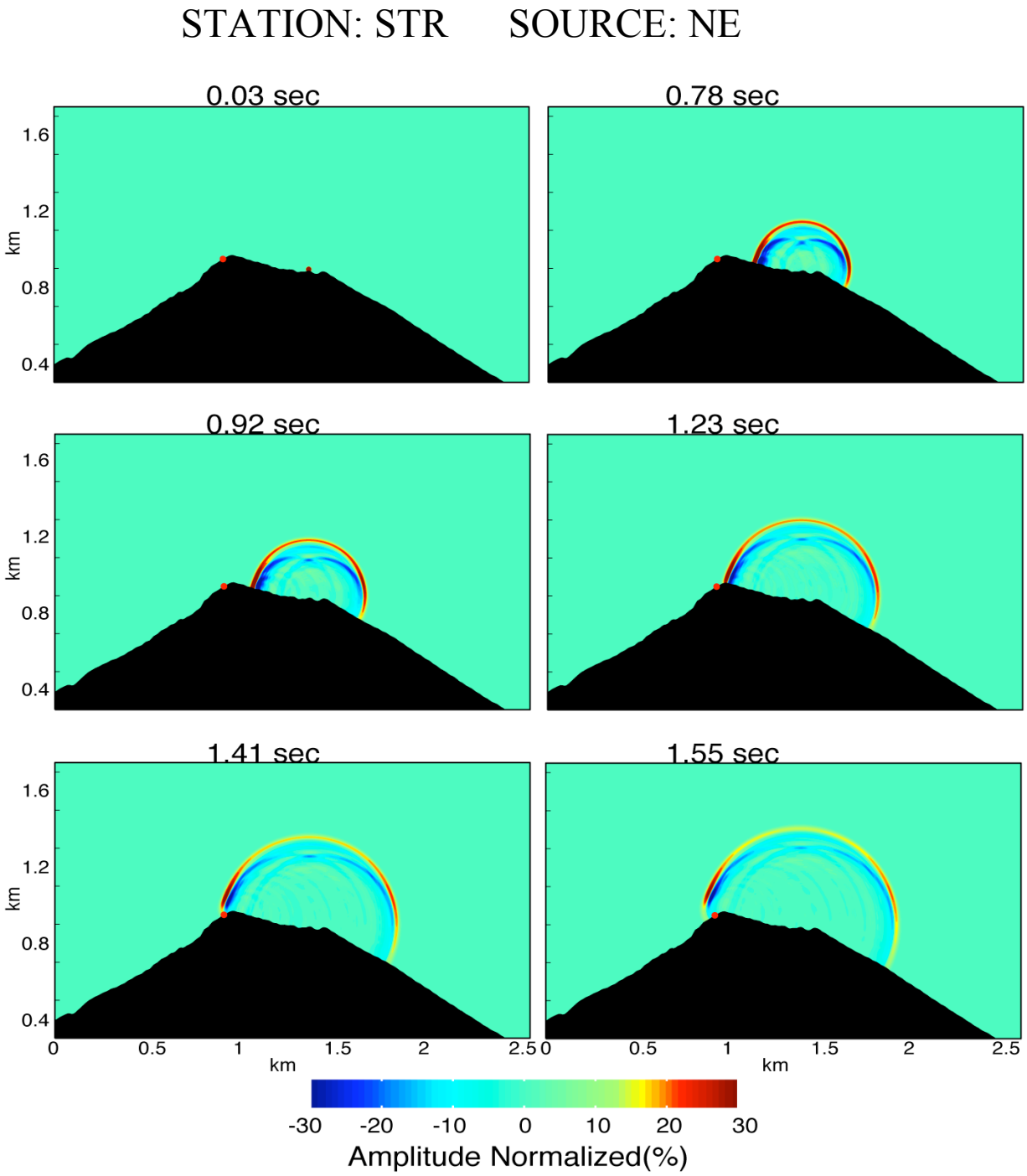

Fig B.6. Snapshots of acoustic wave produced by source located at the NE vent interacting with topographic section of the STR station.

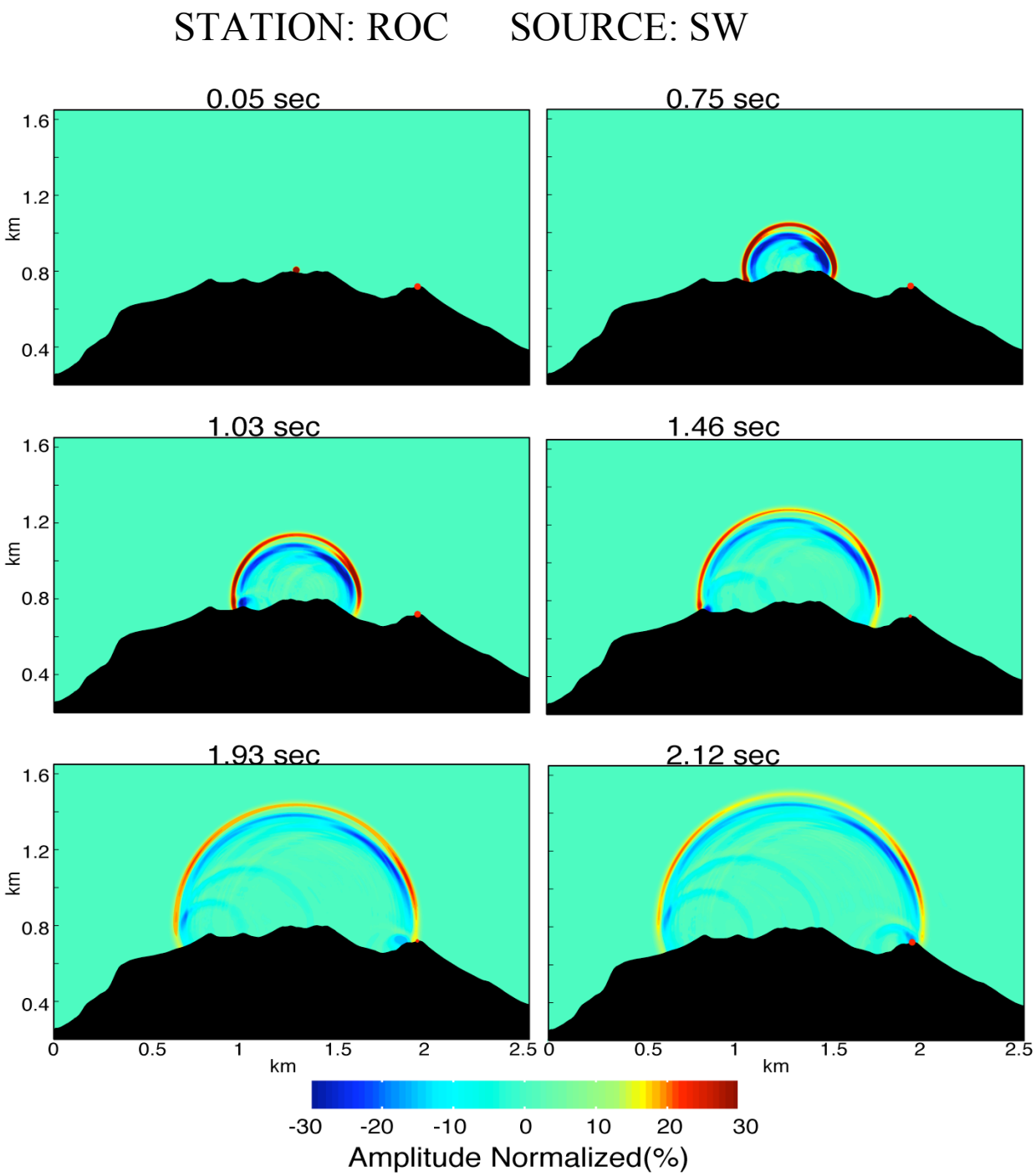

Fig B.7. Snapshots of acoustic wave produced by source located at the SW vent interacting with topographic section of the ROC station.

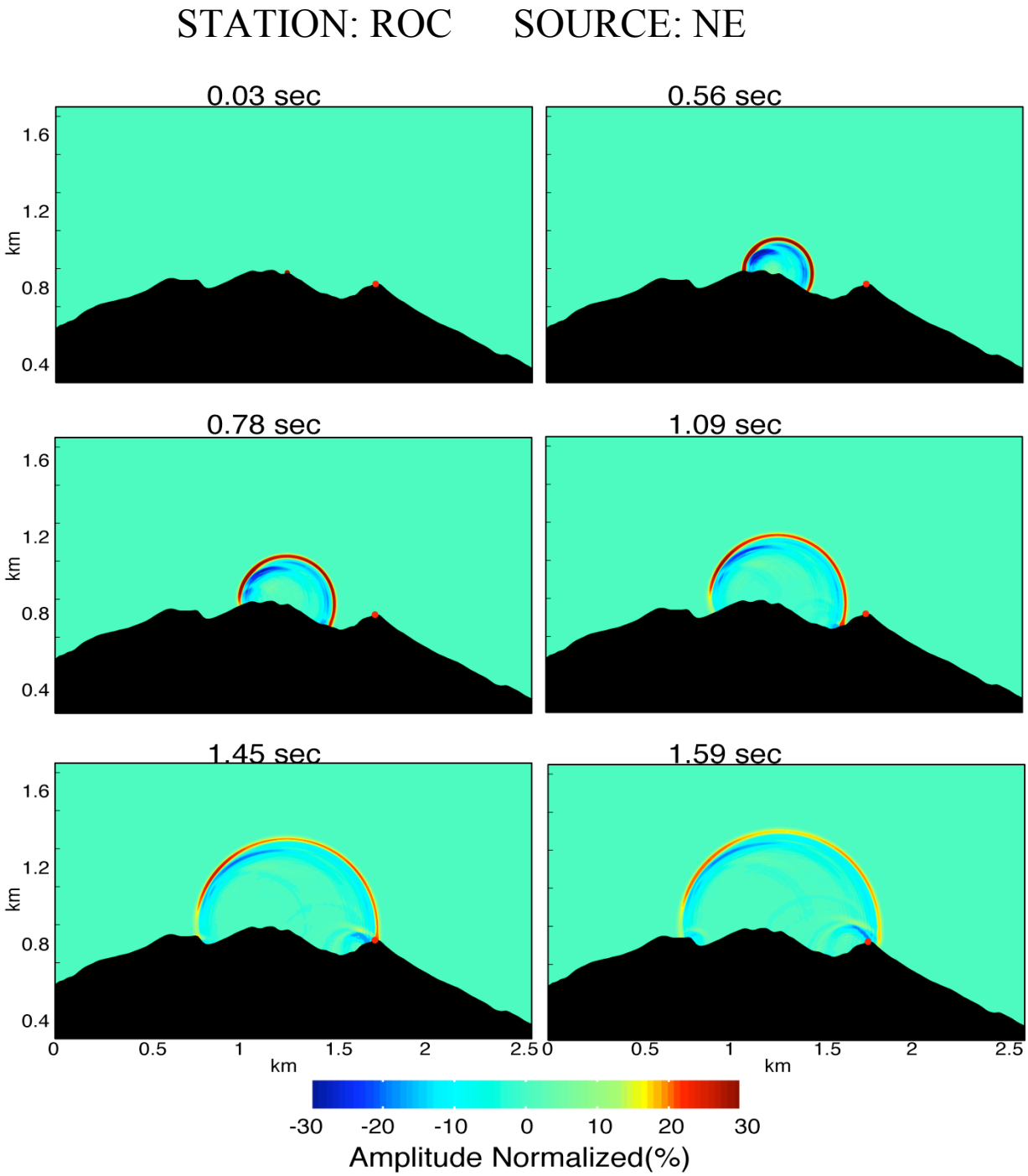

Fig B.8. Snapshots of acoustic wave produced by source located at the NE vent on the topographic section of the ROC station.

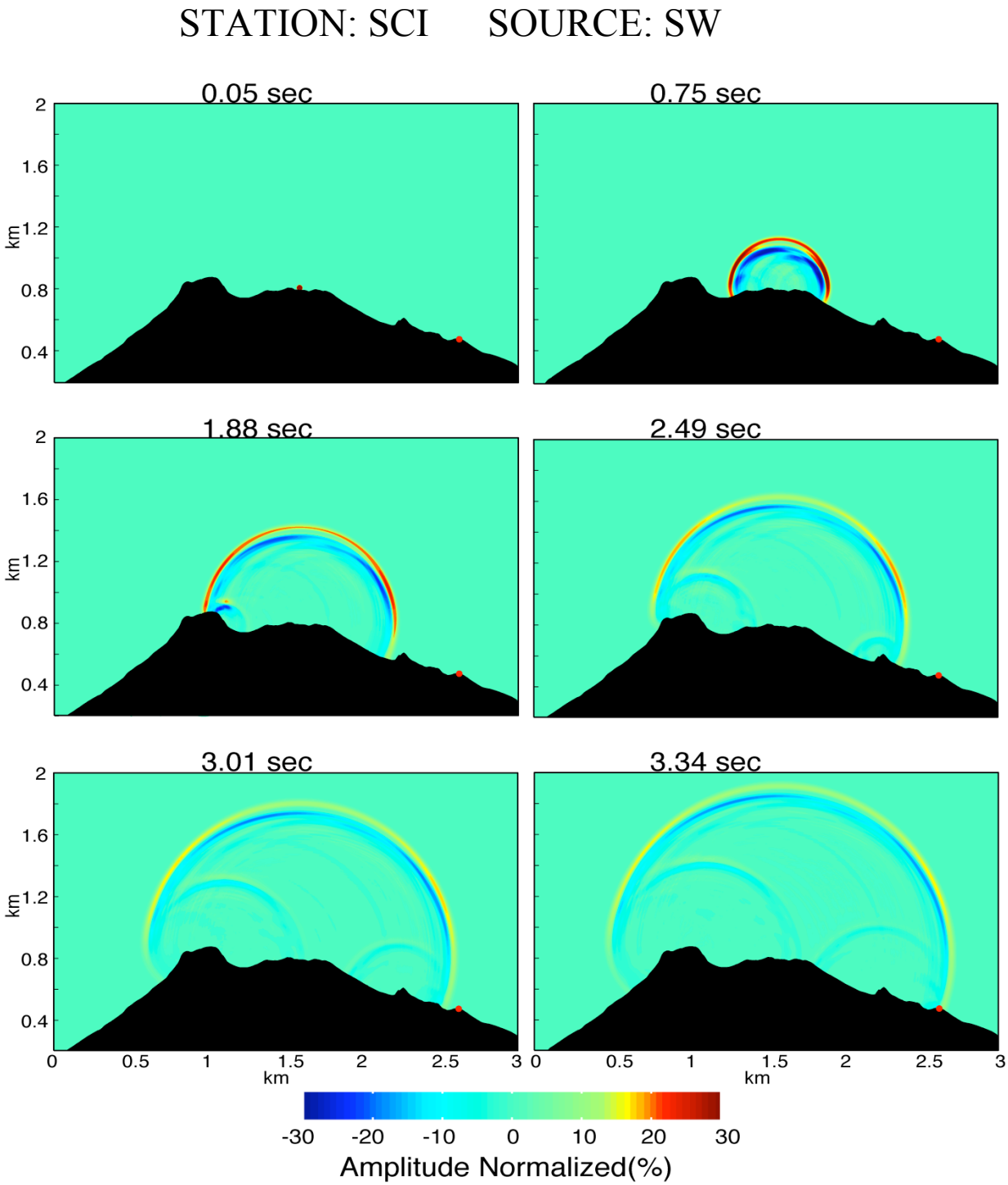

Fig B. 9. Snapshots of acoustic wave produced by source located at the SW interacting with topographic section of the SCI station.

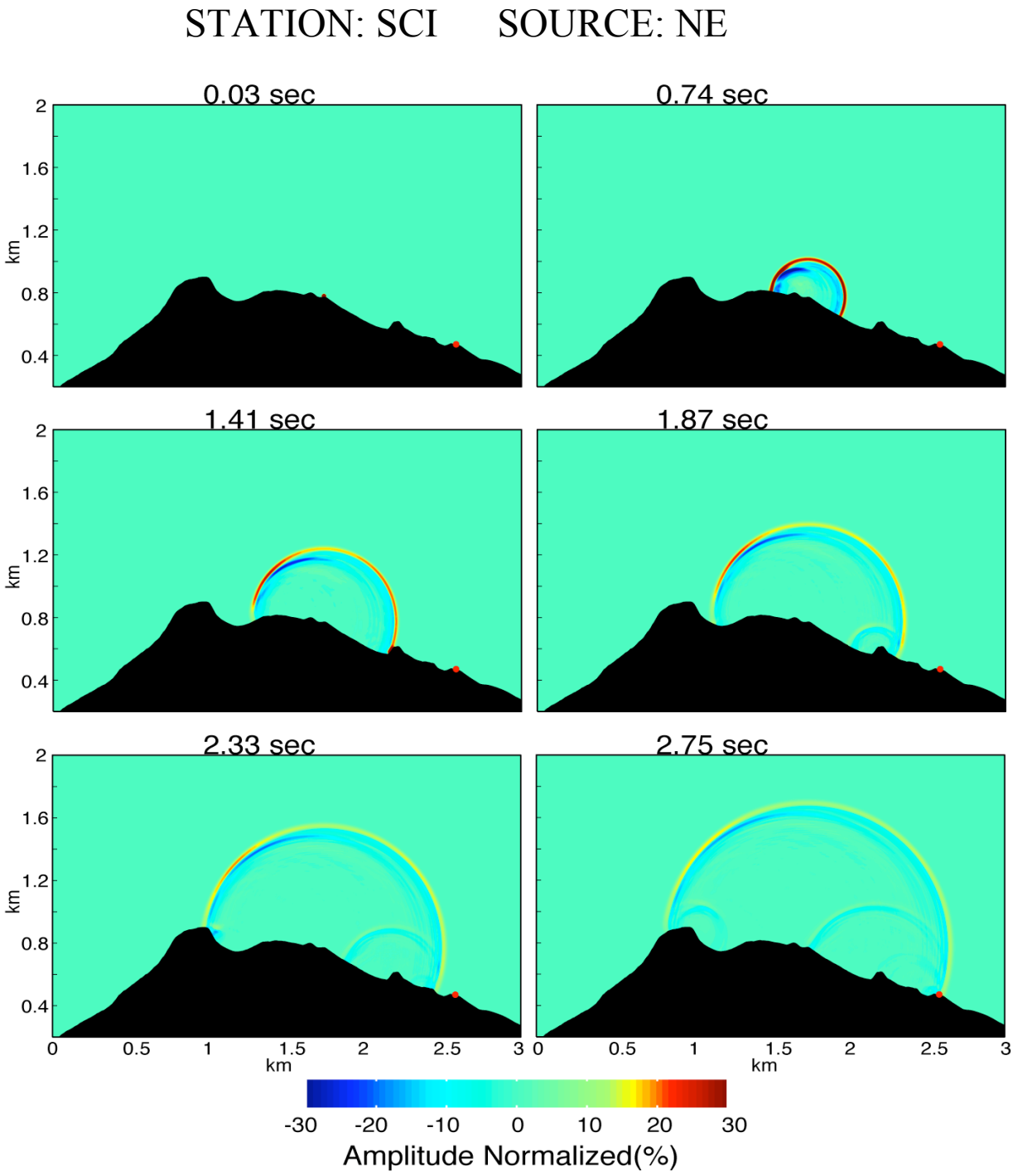

Fig B.10. Snapshots of acoustic wave produced by source located at the NE vent interacting with topographic section of the SCI station.

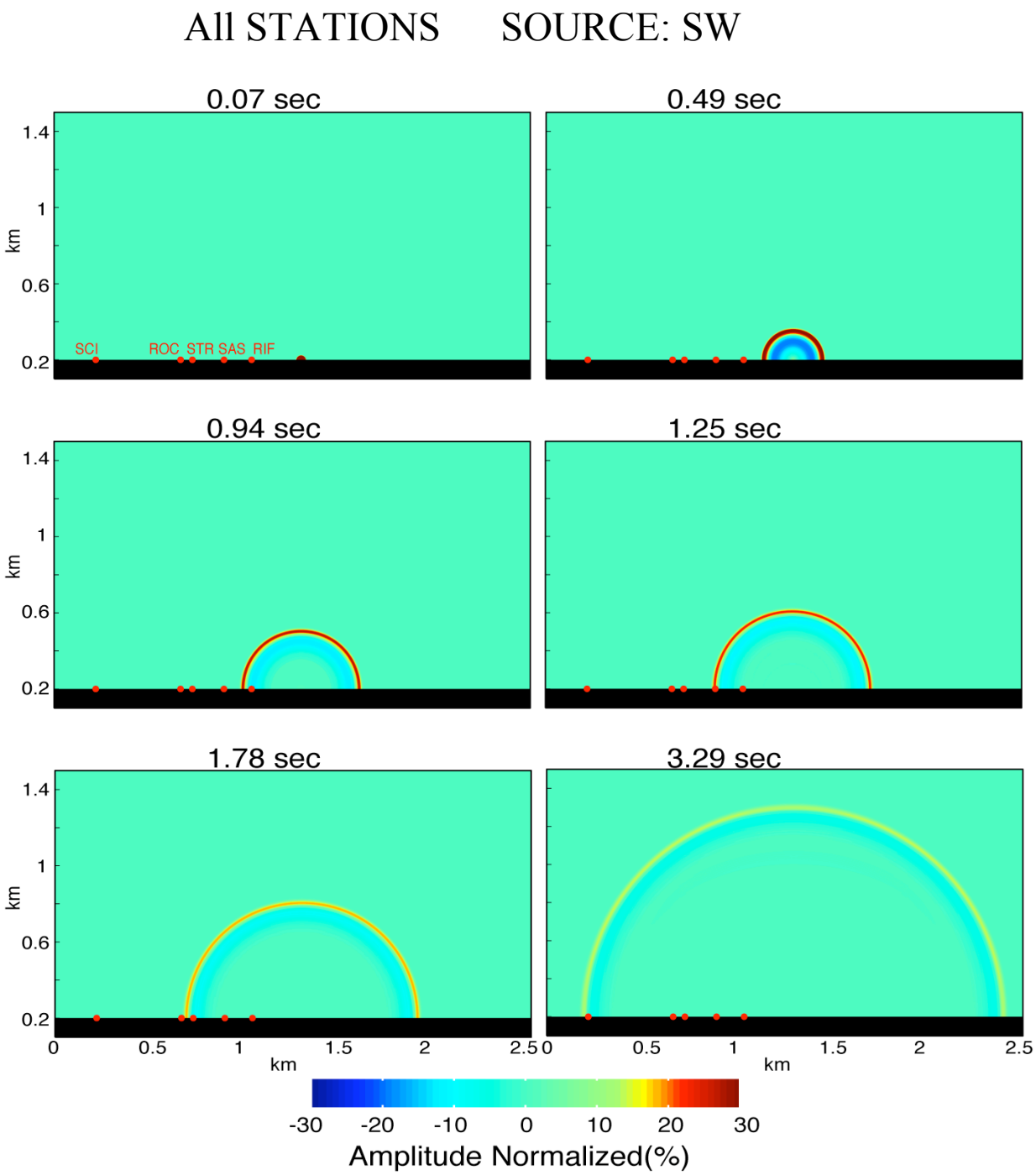

Fig B.11. Snapshots of acoustic wave without topography. The distant between stations (RIF, SAS, STR, ROC, SCI) and source are calculated assuming the source at SW vent.

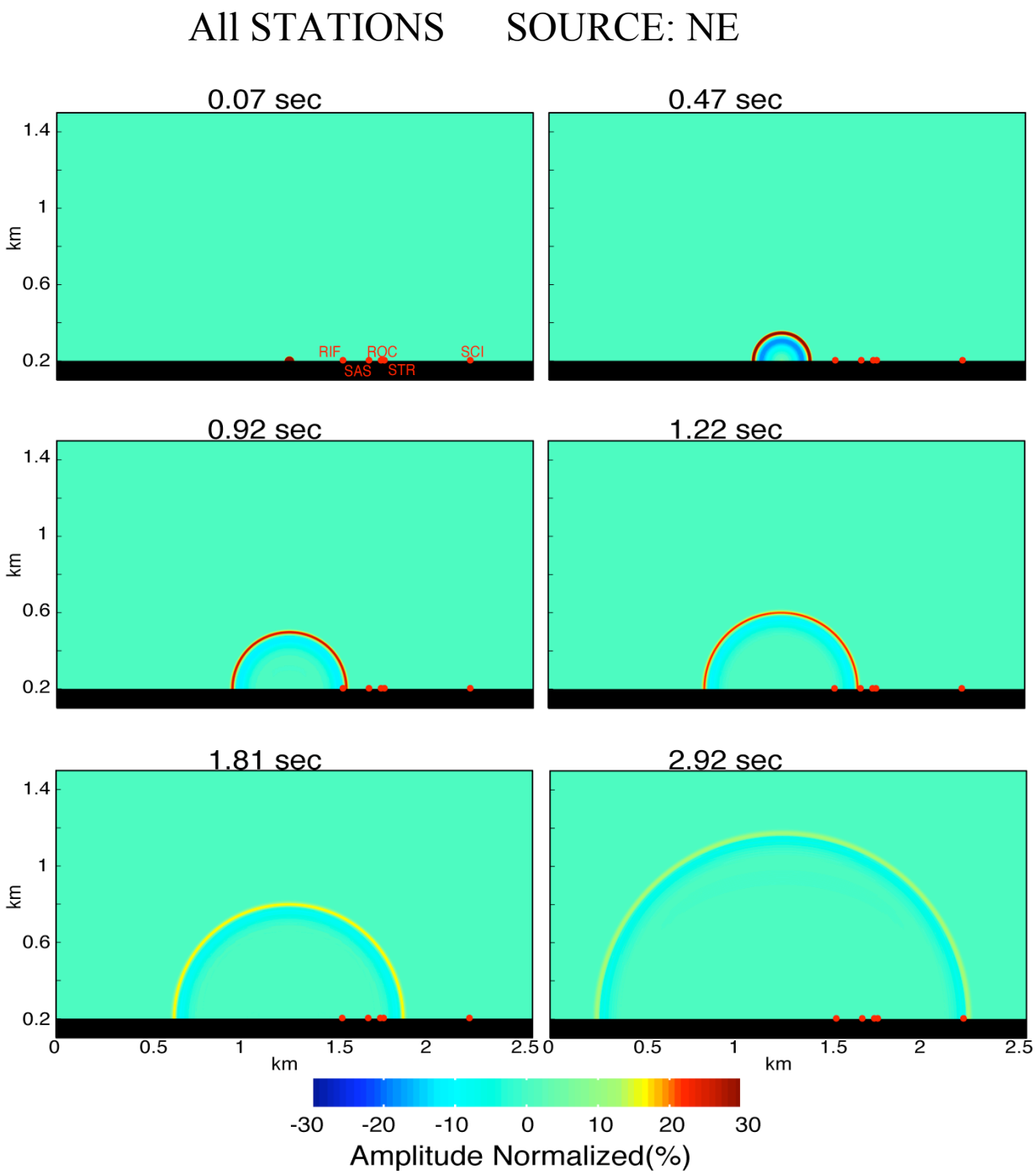

Fig B.12. Snapshots of acoustic wave without topography. The distant between stations (RIF, SAS, STR, ROC, SCI) and source are calculated assuming the source at NE vent.

References

Albert D., L. Lanbo, and M. Moran. **2005.** Time reversal processing for source location in an urban environment (L)[a)], *J. Acoust. Soc. Am., 118 (2),* 616 – 619.

Allard P., J Carbonelle, N. Metrich, H. Loyer and P. Zettwoog. **1994,** Sulfur output and magma degassing budget of Stromboli volcano, *Nature, 368*, 326-330.

Botteldooren, D**. 1994.** Acoustical finite-difference time-domain simulation in a quasi-cartesian grid, *J. Acoust. Soc. Am., 95*, 2313–2319.

Buckingham M.J. and M.A Garcés. **1996**, Canonical model of Volcano acoustics, *J. Geophys. Res., 101*, 8129 – 8151.

Caplan-Auerbach J., A. Bellesiles, J. K. Fernandes. **2010,** Estimates of eruption velocity and plume height from infrasonic recordings of the 2006 eruption of Augustine Volcano, Alaska, *J. Volcanol. Geoth. Res., 189*, 12-18.

Chouet B. **1985,** Exicitation of a buried magma pipe – A seismic source model for volcanic tremor, *J. Geophys. Res., 90,* 1881-1893.

Don C. G.. **1991.** Application of a hard truncated wedge theory of diffraction to wide barriers, *J. Acoust. Soc. Am., 90 (2),* 1005 – 1001.

Dubosclard G., R. Cordesses, P. Allard, C. Hervier, M. Coltelli, Kornprobst. **1999.** First testing of a volcano Dopler radar (Voldorad) Mat Mount Etna, Italy. *Geophys. Res. Lett., 26*, 3389 – 3392.

Garcés M.A and S.R. McNutt. **1997,** Theory of the airborne sound field generated in a resonant magma conduit, *J. Volcanol. Geoth. Res., 78*, 155-178.

Garcés M.A, A. Harris, C. Hetzer, J. Johnson, S. Rowland, E. Marchetti and P. Okubo. **2003a,** Infrasonic tremor observed at Kilauea Volcano, Hawai'i, *Geophys. Res. Lett., 30(20)*, 2023, doi:10.1029/2003GL018038.

Garcés M.A, C. Hetzer, M. Merrifield, M. Willis and J. Aucan. **2003b,** Observation of surf infrasound in Hawai'I, *Geophys. Res. Lett., 30(24)*, 2264, doi:10.1029/2003GL018614.

Garcés M.A, R.A. Hansen and K.G. Lindquist, **1998**, Traveltimes for infrasonic wave propagating in a stratified atmosphere, *Geophys. J. Int., 135*, 255–263.

Garcés M.A, S.R. McNutt, R.A. Hansen and J. Eichelberger. **2000,** Application of the wave – theoretical seismoacoustic models to the interpretation of explosion and eruption tremor signals radiated by Pavlof Volcan, Alaska, *J. Geophys. Res., 105*, 3039-3058.

Garcés M.A. **1997**, On the volcanic waveguide, *J. Geophys. Res., 102*, 22547–22564.

Hadden W. J. and A. D. Pierce. **1981.** Sound diffraction around screens and wedge for arbitrary point source locations, *J. Acoust. Soc. Am., 69,* 1266 –1276.

Hagerty M.T., S.Y. Schawartz, M.A. Garcés and M. Protti. **2000,** Analysis of seismic and acoustic observations at Arenal Volcano, Costa Rica, 1995-1997, *J. Volcanol. Geoth. Res., 101*, 27-65.

Hedlin. **2008.** Finite – difference time domain synthesis of infrasound propagation through an absorbing atmosphere, *J. Acoust. Soc. Am.*, *124 (3)***,** 1430–1441.

Hort M., R. Seyfried, Voge M. **2003.** Radar Doppler velocimetry of vol

Iu K. K. and K. M. Li. **2002.** The propagation of sound in narrow street canyons, *J. Acoust. Soc. Am., 112,* 537 – 550.

Johnson J.B., A.J.L. Harris, S.T.M. Sahetaphy – Engel, R. Wolfe and W. I. Rose. **2004b,** Explosion dynamics of pyroclastic eruptions at Santiaguito volcano, *Geophys. Res. Lett., 31*, L14604, doi:10.1029/2004GL020020.

Johnson J.B., R.C. Aster and P.K. Kyle. **2004a,** Volcanic eruption observed with infrasound, *Geophys. Res. Lett., 31*, L06610, doi:10.1029/2003GL019079.

Johnson J.B., R.C. Aster, M.C. Ruiz, S.D. Malone, P.J. McChesney, J.M. Lees and P.R. Kyle. **2003,** Interpretation and utility of infrasonic records from erupting volcanoes, *J. Volcanol. Geoth. Res., 121*, 15-63.

Johnson J.B.. **2003,** Generation and propagation of infrasonic airwaves from volcanic explotions, *J. Volcanol. Geoth. Res., 121*, 1-14.

Lanbo L. and D. G. Albert. **2006.** Acoustic propagation near a right – angle wall, *J. Acoust. Soc. Am., 119 (4),* 2073 – 2083.

Lightill M.J. **1978,** Waves in fluid. *Cambridge University Press*, New York, 504 pp.

Liu Q. H. and J. Tao. **1997.** The perfectly matched layer for acoustic waves in absorptive media*, J. Acoust. Soc. Am., 102 (4),* 2072 – 2082.

Liu, L., and M.L. Moran. **2002.** Acoustic wave propagation in atmospheric boundary layer above rough terrain, *J. Acoust. Soc. Am.*, *111***,** 2378–2379.

Machado F., W.H. Parsons, A.F. Richards and J.W. Mulford. **1962,** Capelinhos eruption of Fayal volcano, Azores, 1957-1958.

Maekawa Z. **1968.** Noise reduction by Screens, *Appl. Acoust., 1,* 157 – 173.

Marchetti E., M. Ichihara, and M. Ripepe. **2004,** Propagation of acoustic waves in a viscoelastic two-phases system: influence of gas bubble concentration, *J. Volcanol. Geoth. Res., 137*, 93-108.

Marchetti E.. **2007.** Seismic, infrasonic and thermal studies of explosive activity at Stromboli Volcano. Ph.D. Thesis, *Open University.*

Mikumo T. and B.A. Bolt. **1985,** Excitation mechanism of atmospheric pressure waves from the 1980 Mount St. Helens eruption, *Geophys. J. R. Astron. Soc., 81,* 445 -461.

Morrisey M.M. and B.A. Chouet. **1997,** Burst conditions of explosive volcanic eruptions recorded on microbarographs, *Science, 275,* 1290-1293.

Neuberg J. and T. Pointer. **2000,** Effects of volcano – topography on seismic broandband waveforms, *Geophys. J. Int., 143,* 239-248.

Ostashev V.E., D. K. Wilson, L. Liu, D.F. Aldrige, N. P. Symons, and D. Marlin. **2005.** Equation for finte – difference, time domain simulation of sound propagation in moving inhomogeneous media and numerical implementation, *J. Acoust. Soc. Am.*, *117***,** 503–517.

Papadopoulos A. I. and C.G. Don. **1991.** A study of barrier attenuation by using acoustic impulses, *J. Acoust. Soc. Am., 72,* 1011 – 1018.

Pierce A.D. **1974.** Diffraction of sound around corners and over wide barriers, *J. Acoust. Soc. Am., 55,* 941 – 955.

Reed J.W. **1977,** Atmospheric attenuation of explosion waves. *J. Acoust. Soc. Am.*, *61*, 39-47.

Reed J.W. **1987,** Air pressure waves from Mount St. Helens eruption. *J. Geophys. Res., 92,* 11979-11982.

Ripepe M. and E. Gordeev. **1999,** Gas bubble dynamics model for shallow volcanic tremor at Stromboli, *J. Geophys. Res., 104*, 10639 – 10654.

Ripepe M. and E. Marchetti. **2002,** Array tracking of infrasonic sources at Stromboli volcano, *Geophys. Res. Lett., 29*, 2076, doi: 10.1029/2002GL015452.

Ripepe M. and T. Braun. **1994,** Air – wave phases in Strombolian explosion-quakes seismograms: a possible indicator for the magma level?, *Acta Vulcanologica, 5*, 201 – 206.

Ripepe M., A.J.L. Harris and E. Marchetti. **2005a,** Coupled thermal oscillations in explosive activity at different craters of Stromboli volcano, *Geophys. Res. Lett., 32*, L17302, doi: 10.1029/2005GL022711.

Ripepe M., A.J.L. Harris and R. Carniell. **2002,** Thermal, seismic and infrasonic evidences for variable degassing rates at Stromboli volcano, *J. Volcanol. Geoth. Res., 54*, 335 – 351.

Ripepe M., E. Marchetti and G. Ulivieri. **2007,** Infrasonic monitoring at Stromboli volcano during the 2003 effusive eruption: Insight on the explosive and degassing process of an open conduit system. *J. Geophys. Res., 112*, B09207, doi: 10.1029/2006JB004613.

Ripepe M., E. Marchetti, P. Poggi, A.J.L. Harris, A. Fiaschi and G. Ulivieri. **2004a,** Seismic acoustic and thermal network tracks in real time the 2003 eruption of Stromboli Volcano, *EOS Trans. AGU, 85,* 35, 329-332.

Ripepe M., P. Poggi and E. Marchetti. **2004b,** Small aperture infrasonic array monitors activity at Stromboli volcano, *Inframatics, 7*, 1 -1 4.

Ripepe M., P. Poggi, T. Braun and E. Gordeev. **1996,** Infrasonic waves and volcanic tremor at Stromboli, *Geophys. Res. Lett., 23*, 181 - 184.

Ripepe M., S. Ciliberto and M. Della Schiava. **2001a,** Time constrains for modelling source dynamics of volcanic explosions at Stromboli, *J. Geophys. Res., 106 (B5)*, 8713 – 8727.

Ripepe M., S. De Angelis, G. Lacanna, and B. Voight. **2010.** Observation of infrasonic and gravity waves at Soufrière Hills Volcano, Montserrat, *Geophys. Res. Lett., 37,* L00E14, doi:10.1029/2010GL042557.

Ripepe M., S. De Angelis, G. Lacanna, P. Poggi, C. Williams, E. Marchetti, D. Delle Donne, and G. Ulivieri. **2009,** Tracking Pyroclastic Flows at Soufrière Hills Volcano, *EOS Trans. AGU, 90*, 27, 229-236.

Schroder C. T. and W. R. Scott. **2002.** On the stability of the FDTD algorithm for elastic media at a material interface, *IEEE Trans. Geosci. Remote Sens., 40*, 474 – 481.

Sparks R.S.J. **1997,** Volcanic Plumes. *Wiley*, New York, 574 pp.

Sparks R.S.J. **1998,** The Physics of Explosive Volcanic Eruptions. *Geol. Soc.*, London, 186 pp.

Sutherland L. C. and H. E. Bass. **2004.** Atmospheric absorption in the atmosphere up to 160 Km, *J. Acoust. Soc. Am.*, *115***,** 1012–1032.

Tahihara M., M. Nomura, Y. Sawada and K. Kamo. **1996,** Infrasonic and acoustic – gravity waves generated by the Mount Pinatubo eruption of June 15, 1991, *Fire and Mud. University of Washington Press, Seattle,* 601-614.

Vergniolle S. and C. Jaupart. **1986,** Separated two – phase flow and basaltic eruptions. *J. Geophys. Res., 91*, 12842-12860.

Vergniolle S. and G. Brandeis. **1994,** Origin of the sound generated by Strombolian explosions, *Geophys. Res. Lett., 21*, 1959-1962.

Vergniolle S. and G. Brandeis. **1996,** Strombolian explosions 1. A large bubble breaking at the surface of a lava column as a source of sound, *J. Geophys. Res., 101*, 20433-20447.

Vergniolle S. and J. Caplan-Auerbach. **2006,** Basaltic Subplinian plumes and thermals: constrains from acoustic measurements at Shishaldin volcano, Alaska, *Bull. Volcanol., 68*, 611-630.

Vergniolle S., G. Brandeis and J.C. Marechal. **1996,** Strombolian explosions 2. Eruption dynamics determined from acoustic measurements, *J. Geophys. Res., 101*, 20433-20447.

Vergniolle S., M. Boichu and J. Caplan-Auerbach. **2004,** Acoustic measurements of the 1999 basaltic eruption of Shishaldin volcano, Alaska 1. The origin of Strombolian activity, *J. Volcanol. Geoth. Res., 137*, 109-134.

Virieux J. **1984.** SH-wave propagation in heterogeneous media: Velocity – stress finite difference method, *Geophysics, 49,* 1933 – 1942.

Wang S. **1996.** Finite – difference time – domain approach to underwater acoustic scattering problems. *J. Acoust. Soc. Am., 99,* 1924 – 1931.

Wilson L. **1980,** Relationships between, pressure, volatile content and ejecta velocity in three types of volcanic explosion, *J. Volcanol. Geoth. Res., 8*, 297-313.

Woulff G. and T.R. McGetchin. **1976,** Acoustic noise from volcanoes: theory and experiment. *Geophys. J. R. Astron. Soc., 45*, 601-616.

Yamasato H. **1997,** Quantitative analysis of pyroclastic flows using infrasonic and seismic data at Unzen Volcano, Japan, *J. Phys. Earth, 45,* 397-416.

Yee K.S. **1966.** Numerical solution of initial boundary value problems involving Maxwell's equations in isotropic media. *IEEE Trans. Antennas Propag., 14,* 302 – 307.